Title
Electric Field Control of Ferromagnetism and Magnetic Devices Using Multiferroics

Author
Heron, John Thomas

Publication Date
2013

Peer reviewed|Thesis/dissertation

Electric Field Control of Ferromagnetism and Magnetic Devices Using Multiferroics

By

John Thomas Heron

A dissertation submitted in partial satisfaction of the
requirements for the degree of
Doctor of Philosophy

in

Engineering - Materials Science and Engineering

in the

Graduate Division
of the
Universisty of California, Berkeley

Committee in charge:

Professor Ramamoorthy Ramesh, Chair
Professor Junqiao Wu
Professor Sayeef Salahuddin

Spring 2013

Electric Field Control of Ferromagnetism and Magnetic Devices Using Multiferroics

Abstract

Electric Field Control of Ferromagnetism and Magnetic Devices Using Multiferroics

by

John Thomas Heron

Doctor of Philosophy in Engineering - Materials Science and Engineering

University of California, Berkeley

Professor Ramamoorthy Ramesh, Chair

This dissertation presents a study of a heterostructure composed of room temperature magnetoelectric multiferroic $BiFeO_3$ and ferromagnetic $Co_{.90}Fe_{.10}$, with specific interest in understanding the interfacial coupling mechanisms in this system and establishing the electric field control of a magnetization and spintronic devices. The field of spintronics has been plagued with the problem of a large energy dissipation as a consequence of the resistive losses that come during the writing of the magnetic state (i.e. reversing the magnetization direction). The primary aim of the work presented here is to investigate and understand a novel heterostructure and materials interface that can be demonstrated as a pathway to low energy spintronics. In this dissertation, I will address the specific aspects of multiferroicity, magnetoelectricity, and interface coupling that must be addressed in order to reverse a magnetization with an electric field. Furthermore, I will demonstrate the reversal of a magnetization with an electric field in single and multilayer magnetic devices. The primary advances made as a result of the work described herein are the use of epitaxial constraints to control the nanoscale domain structure of a multiferroic which is then correlated to the domain structure of the exchange coupled ferromagnet. Additionally, the magnetization direction of the ferromagnetic layer is controlled with only an applied electric field at both macroscopic and microscopic scales. Lastly, using this electric field control of ferromagnetism, the first demonstration of a magnetoelectric memory bit is presented.

To my family, Mom, Dad and Daniel,

for all of your love and support.

Table of Contents

List of Figures

Acknowledgments

This thesis is dedicated to my family, who I have been so blessed to have. Mom, Pops, and Daniel. From the beginning, you guys have always put education first (from the days of homeschooling all the way through college) and have instilled in me the confidence and courage to pursue science. To all of my grandparents, aunts, uncles and cousins: you have all provided so much support. You have always reinforced my goals, shown me such a great respect and have always believed in me. You are all guiding stars in my life.

I owe a great deal to many individuals throughout my scientific career, however, Professor Ramesh has, by far, been the most impactful and to you I owe a great deal. You have provided me the opportunity to study at UC Berkeley and greatly shaped my growth as a person and scientist. You have introduced me to oxide multiferroics and allowed me to pursue my passion for spintronics research. Your passion and enthusiasm for science is second to none. As a great source of personal and professional inspiration, I hope our work together and friendship continue to grow.

To my greatest collaborator, teacher, and friend, Dr. Morgan Trassin: You have taught me so much, both in science and in every other aspect of life. Through all of our work together: the IP, OOP, and spin valve work, the SEMPA and Finland collaborations, your mentorship and friendship has been a pillar of strength. I wish you and your family all of the best in the future.

I would also like to thank those who have so greatly impacted my academic career from the early years. The research and relationships that I performed and made at UC Santa Barbara are very dear to me. I surely wouldn't be writing this this if Professor David Awschalom hadn't given me the opportunity to investigate magnetic semiconductors in his group. I had learned so much. It was here that I developed such great personal and professional relationships, developed a great deal of technical skills and discovered so much regarding the physics of semiconductors and spins in solids. Again, David, you have my deepest sense of appreciation. The strength and combination of your scientific and leadership abilities are incredible and serve as a model for me to aspire to. Additionally, my two mentors Shawn Mack and Mark Nowakowski: I am deeply grateful for the friendship and continual guidance over the years. If I can't give you anything back for what you have given me, I hope that I at least make you both proud.

I also would like to thank my closest friends, those friendships that were formed long ago and those developed in graduate school. To Kevin and Jason Lauterjung, Emily Thompson, Rohini Shankaran, Anthony Diamond, Paul Rogge, Alejandro Levander, Claire Chisholm, the MSE department at Berkeley, it has been a truly amazing four and a half years. I hope our paths through life continue to cross.

I would also like to express my deepest gratitude to Professors Sayeef Salahuddin, Junqiao Wu, Oscar Dubon and Yuri Suzuki. To Professor Salahuddin, to whom I possess a great respect and admiration for, has served on my qualifying exam and

thesis committees but has made a far more significant impact on my development through his contributions to the work and intellectual property presented in this thesis and his academic and career counseling. To Professor Wu, who has also served on my qualifying exam and thesis committees, your feedback has been critical to my graduate career. To Professor Dubon, your enthusiasm for all things academic is a quality I strive for. Thanks for the academic and career mentoring, committee member service and conversations beginning from day one of graduate school. To Professor Suzuki, for serving as my qualifying exam chair, for the many great lectures on magnetism and trusting me to represent the department during the prospective graduate student visits for a couple of years, thanks.

Working in the Ramesh lab I was able to collaborate with many talented individuals and develop friendships with many great minds. Chen Wang and Dan Ralph who I have been able to work with over the years on this spin valve project. I must also thank Dmitri Nikonov at Intel for all of the contributions to the in-plane switching paper and the OOMMF simulations, Khalid Ashraf in the electrical engineering department for all of the great discussions and simulations of the electrical switching in the in-plane work. Of course, I must thank all of the former and current Concept group members for the collaborations, friendship, and good times: Xavi Marti, Guneeta Singh-Bhalla, James, Lane, Tommy, Pu, Jinxing, QTL, Steven, Bala, Jayakanth, Jan, Jian, Jiun-Haw, Di, Dennis, Asif, Micky, Martin Gajek, Helen He, Eddie Chu, Seung-Yeul, Claudy Serrao, Ajay Yadav, Shwaran Mishra, Oleg Sapunkov, and Ryan Paull. You have all trusted me with so much and have enlightened me and shape me as a scientist.

I would like to express my appreciation for the financial support provided by NDSEG graduate fellowship over three years of my graduate tenure. The research presented here was made with Government support under and awarded by DOD, Air Force Office of Scientific Research, National Defense Science and Engineering Graduate (NDSEG) Fellowship, 32 CFR 168a.

Chapter 1

Introduction

In this chapter I will provide a brief background to the key definitions and concepts that are referred to frequently in this thesis. The central theme of the work presented in this dissertation is to establish the electric field control of ferromagnetism (and magnetic devices) at room temperature. The theme of this work extends to address the questions of whether the ferromagnetism be reversed with an electric field and if such a system can be integrated into a device for spintronics applications. To begin, the work presented in this dissertation is motivated by a discussion of the idea of establishing the electric field control of ferromagnetism in light of fundamental scientific inquiry and technological demand. What follows is the introduction to multiferroics, magnetoelectrics and exchange coupling in antiferromagnet-ferromagnet heterostructures. Finally, this chapter ends with an outline that will organize the remainder of this thesis and summarize the contents of each section.

1.1 Importance of the electric field control of ferromagnetism

1.1.1 Motivation: a physical perspective

Before the early 1800's, electricity and magnetism were believed to be derived from distinct forces. Due to the works from the likes of Oersted, Faraday, Henry and Maxwell, the deep connections between electricity and magnetism were revealed and we now understand that both electricity and magnetism result from a single electromagnetic force. The impact of this connection has broadened with time, moving from a physics discovery to technological applications. The classical relations of Ampere's law and Faraday's law of induction are heavily integrated into modern electromagnetic devices. In devices such as antennas, magnetometers, motors, magnetic memories and electromagnets, electromagnetic fields are created or detected through the flow of a current. Issues with the use of electrical currents create technological issues result-

ing from resistive heating. With the use of classical electromagnetism, the complex interactions between fields, charge carriers, and spins in solids as a means towards establishing new connections between electricity and magnetism, have largely been neglected. A desirable effect would establish the link between a voltage and magnetic field without the flow of current.

Furthermore, in the classical laws of electromagnetism, there is a clear connection between the symmetry broken by the applied field or current and the field that manifests (see Figure 1.1). From Ampere's law

$$\oint \vec{B} \cdot \vec{dl} = I_{enc} = \frac{dq}{dt} \tag{1.1}$$

it is seen that the motion of electrons breaks time reversal symmetry and results in the manifestation of a magnetic field, which also breaks time reversal symmetry. Similar to a current, the spin angular momentum of the atoms in a ferromagnet or antiferromagnetic crystal break time reversal symmetry. An electric dipole is classically expressed as

$$\vec{p} = q\vec{d} \tag{1.2}$$

where $\vec{d}$ is the spatial separation between charges. An electric dipole breaks spatial inversion symmetry (since the direction of $\vec{d}$ changes the direction of $\vec{p}$). Since the electric dipole is linearly proportional to the elelctric field, an electric field also breaks spatial inversion symmetry. Since the classical laws require a current to couple charge to magnetism, it becomes a question of physics whether an electric field can be used to control magnetism. An exploration of this question in solid state systems is necessary.

1.1.2 Motivation: a technological perspective

The importance of the connection between electricity and magnetism in this information age can be seen by the abundance of electromagnetic devices. This relationship, however, requires the flow of an electrical current. This fact accounts for several technological issues. To date the most relevant issue arises from the energy loss due to Joule heating (resistive losses = I^2R). Joule heating presents two problems. The thermal energy that is created is lost to the environment and is irrecoverable. The resistive losses will heat other components in the device making thermal management a critical component to device functionality and lifetime. Lastly, because the thermal energy cannot be recovered, the thermal dissipation of the electrical energy is essentially wasted energy, energy that is not used by the system to provide functionality.

Historically, magnetic bits have been used to store information via the ability to retain two remnant magnetization directions. The first magnetic memory (magnetic core memory) was made in the 1950's to improve the speed and reliability of earlier computer memory. [1] In this memory, tori of magnetic materials (cores) were used

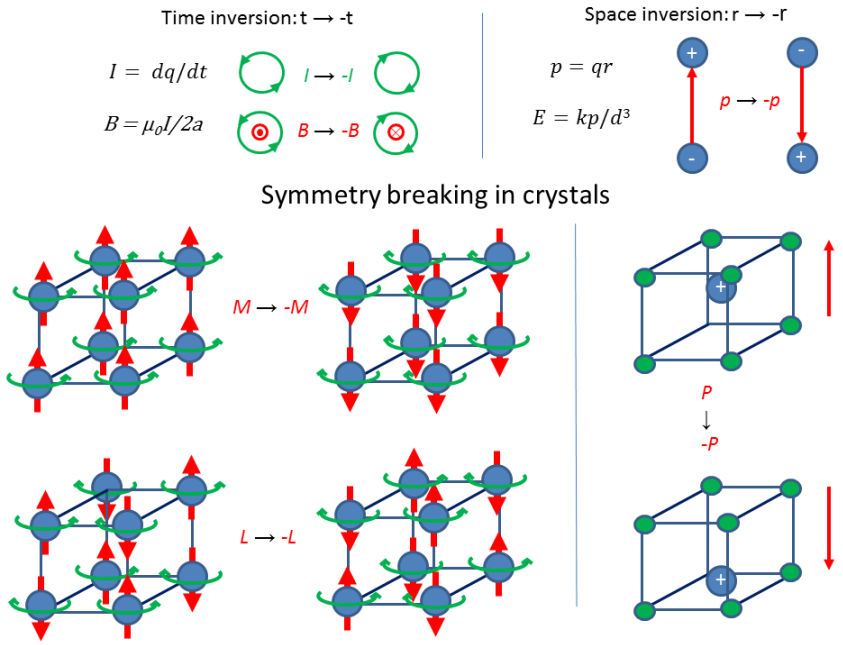

Figure 1.1: Time (or time reversal) and spatial inversion symmetries in electromagnetic equations and ferroic crystals. A current breaks time reversal symmetry while preserving spatial inversion symmetry. An electric dipole breaks spatial inversion symmetry while preserving time reversal. As a consequence, magnetic fields and magnetic moments break time inversion symmetry. Similarly, the electric field can be expressed in terms of an electric dipole and hence the electric field also breaks space inversion symmetry. Taking this understanding to the macroscopic orders in magnetic and ferroelectric crystals, ferromagnetic and antiferromagnetic crystals break time inversion symmetry and ferroelectric crystals break space inversion.

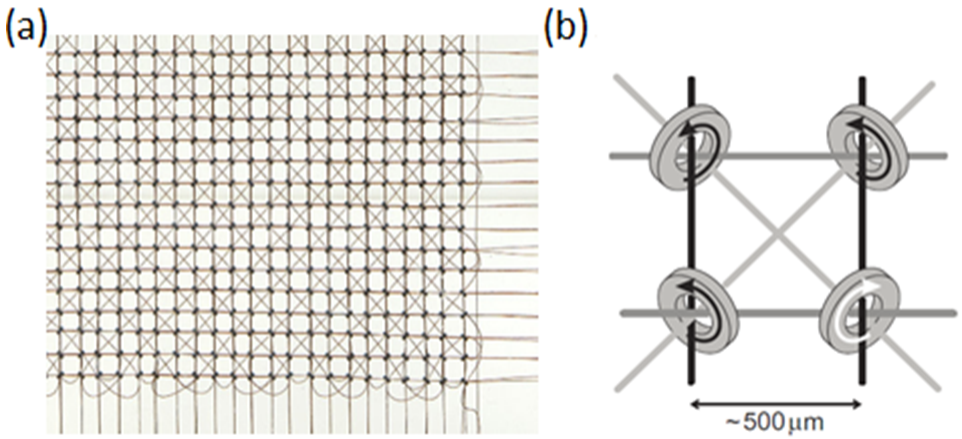

Figure 1.2: (a) Image of early magnetic core memory. World lines and read lines are strung through the cores to read and write the magnetic information. (b) Close up of the magnetic core memory architecture. Figure from [2].

to store binary information using the remnant magnetization. Currents were run through wires that were strung through the holes of the core to write and access the data stored in the cores (see Figure 1.2). Two lines were used to generate magnetic fields that would toggle the magnetization between remnant states. A third wire was used to read out the information via inductance. [2]

While the magnetic core memory has forever changed computer memory, it has since been long abandoned due to its inefficient use of energy and space. The constant demand for faster and higher memory density has made this architecture a display for a museum in just about 20 years (1950 - 1970). [2] As the bits were packed closer and closer together, the magnetic fields generated to switch an individual bit began to fringe into other neighboring bits, creating an issue with the ability to store the information without an error and preventing further scaling of the bit density.

This issue has been circumvented with a memory based on spin transfer torque (STT) [3, 4], where a spin-polarized current is injected into the magnetic layer to write the magnetic state. The remnant magnetic state of the bit is determined through the device resistance since it is dependent on the orientation of the magnetization (magnetoresistance). The limiting factor in the further miniaturization of these technologies lies in the significant energy losses that occur from the increased resistive losses as the size of the technology is decreased. While STT memories provide the historical advantages of magnetic based memories such as high speed, high density and high endurance in a non-volatile technology, it does not sufficiently address the major concern of substantially lowering energy dissipation and write energies to levels required to revolutionize memory. Furthermore, the large current is damaging to the memory device and ultimately reduces the lifetime of the memory bit significantly. [5] Prob-

lems of reliability are still hindering serious commercialization of STT based memory [5], and by the time of its commercialization, other memory technologies will likely be competitive on the basis of energy per bit.

Looking beyond magnetic memory, electromagnetic devices such as antennas and electromagnetic motors are some of examples of where a current is supplied to create or control a magnetic field or magnetic device. Similar to magnetic memories, as the dimensions of these devices are scaled down further, the implications of the resistive losses becomes impractical and represents a scientific barrier that inhibits the advancement of commercial electromagnetic devices. This has led to the pursuit of discovering mechanisms by which magnetic anisotropy and the magnetization direction in magnetic materials can be tailored without the flow of electrical current. The appeal of this new idea lies in the significant ramifications that a direct electric field control of magnetism has on the further miniaturization of electromagnetic devices.

From the previous discussions, it is clear that the pursuit of the electric field control of magnetism is an important question both fundamentally and technologically. The question is, how do we now go about approaching the electric field control of magnetism in the solid state?

1.1.3 Pathways to the electric field control of ferromagnetism

In the solid state there can be electron correlations that lead to the coupling of spin, orbital, lattice and charge degrees of freedom. Such correlations have opened up exciting fields of research in the areas of high temperature superconductivity [6], metal-inslator transitions [7], and colossal magnetoresistance [8, 9]. This concept has been pursued beyond correlations of bulk systems to the correlations at interfaces as well. [10, 11] Figure 1.3 shows an example of such a concept.

For the work presented herein, we are concerned with the coupling between spin, lattice and charge. Figure 1.4 shows a map that illustrates the routes that can be taken to establish the electrical control of magnetism in the solid state using the coupling between each of these degrees of freedom. Of primary interest is the piezoelectricity or ferroelectricity (the coupling of charge to lattice/strain), magnetostriction (coupling of spin and lattice), magnetoelectricity (coupling of charge and spin) and the inverse of these properties. It is important to note the possible paths that can be taken on this map as well as the map's handedness. With the electric field as the input, a clockwise or counterclockwise path towards the control of magnetism can be chosen. A counter clockwise path connects an electrical input to magnetism through the lattice/strain, while a clockwise path is more direct, connecting charge and spin orders directly through magnetoelectricity. While each path has its advantages and disadvantages, the handedness of the map is determined by the symmetry that is broken by the mechanism by which the coupling is driven. A counter clockwise rotation utilizes piezoelectricity to create a distortion of the lattice which then changes the magnetic anisotropy through inverse magnetostriction. Magnetostriction is phe-

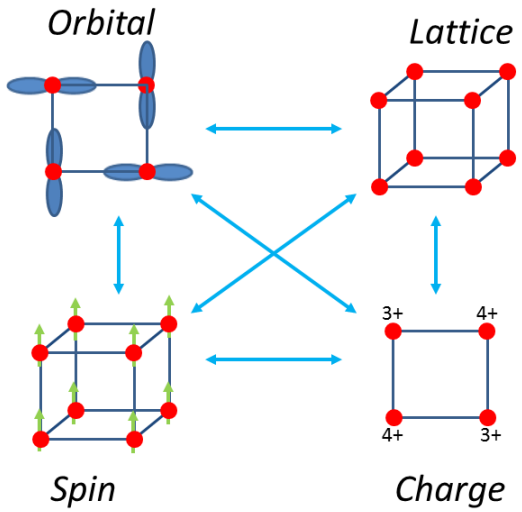

Figure 1.3: Example of the interplay that can exist in materials that show strong correlations.

nomenon due to the spin-orbit interaction and hence does not break time reversal symmetry. Additionally, neither the applied electric field nor the piezoelectric effect breaks time reversal symmetry. It is for this reason that devices based on clockwise handedness are not able to reverse a magnetization but are limited to rotating the anisotropy by 90 degrees or less. If the clockwise path is chosen, it is then possible for the coupling mechanism to break time reversal symmetry, depending on the order of the magnetoelectric coupling, which could allow for the electric field induced reversal of a magnetization.

While the map can be used to establish connections between charge and spin orders for a great deal of material configurations, however for the applications that are considered here, a non-volatile technology is desired. The idea of data storage has resulted in the integration of single phase and composite systems that have more than one ferroic order parameter (multiferroics). In this chapter I will discuss only single phase multiferroics, which are magnetoelectric (coupled magnetic and electrical order parameters - counterclockwise path). Composite multiferroics, where no individual component is magnetoelectric or multiferroic (clockwise pathway on map) are discussed, along with other other pathways to the electrical control of magnetism, in Appendix A.

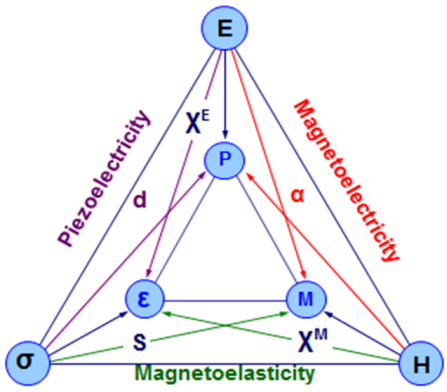

Figure 1.4: Roadmap of the routes to electrical control of magnetism.

1.2 Magnetoelectrics and multiferroics

Over the past 10 years there has been a revival of interest in materials or heterostructures that possess more than one ferroic parameter, largely due to the interest in studying the correlations between two or more ferroic orders [12] as well as the possibility to demonstrate next generation devices using these correlations. Materials of this class are deemed multiferroic. [13, 14] Originally the definition of multiferroics was limited to single phase materials which simultaneously display one of the four ferroic orders: ferroelectricity, ferromagnetism, ferroelasticity, and ferrotoroidicity. [15] This definition has been broadened to include materials that possess antiferroic order, such as antiferromagnetism rather than ferromagnetism, as well. In this dissertation, the focus is on multiferroics that possess ferroic or antiferroic electrical and magnetic orders. Furthermore, the coupling between these two ferroic orders (magnetoelectricity/magnetoelectric multiferroics) is also of primary interest. In this section, magnetoelectric multiferroics are briefly introduced with an emphasis on how they can be used to establish the electric field control of magnetism at room temperature.

1.2.1 Magnetoelectrics

From a scientific perspective the excitement behind magnetoelectrics or the magnetoelectric effect in materials is the possiblity to magnetically control a polarization [16] and the inverse (electrical control of ferromagnetism). Most of the research focus has been driven by the prospect of the electric field control of magnetism for low-power applications. While the magnetoelectric effect has recently become the focus of much theoretical and experimental investigation, the magnetoelectric effect was proposed long ago by P. Curie in 1894 [17] but was not experimentally verified for nearly 70 years later in Cr_2O_3. [18, 19, 20, 21, 22]

A clear understanding of the magnetoelectric effect can be obtained from the

expansion of the free energy, expanded in E and H (the electric and magnetic fields), as shown in [23].

$$F(\vec{E},\vec{H}) = F_0 - P_i^s E_i - M_i^s H_i - \frac{1}{2}\epsilon_0\epsilon_{ij}E_iE_j - \frac{1}{2}\mu_0\mu_{ij}H_iH_j$$

$$-\alpha_{ij}E_iH_j - \frac{1}{2}\beta_{ijk}E_iH_jH_k - \frac{1}{2}\gamma_{ijk}H_iE_jE_k - .... \tag{1.3}$$

To obtain the expression for the thermodynamic order parameter (i.e. P(E, H) and M(E, H)), the free energy expansion is differentiated by the thermodynamic driving parameter (i.e. E or H).

$$P(\vec{E},\vec{H}) = -\frac{\partial F}{\partial E_i} = P_i^s + \epsilon_0\epsilon_{ij}E_j + \alpha_{ij}H_j + \frac{1}{2}\beta_{ijk}H_jH_k + \gamma_{ijk}H_jE_k + ... \tag{1.4}$$

$$M(\vec{E},\vec{H}) = -\frac{\partial F}{\partial H_i} = M_i^s + \mu_0\mu_{ij}H_j + \alpha_{ij}E_j + \beta_{ijk}E_jH_k + \frac{1}{2}\gamma_{ijk}E_jE_k + ... \tag{1.5}$$

The terms with the α_{ij} coefficients describe the linear magnetoelectric effect and the higher order magnetoelectric terms are given byβ_{ijk} and γ_{ijk} are typically smaller than the linear term, and thus not refered to when the magnetoelectric effect is discussed.

As alluded to already, for applications, the interest in multiferroics is largely due to the potential to utilize a large magnetoelectric effect. Limitations of the magnetoelectric response were determined early on, in an attempt to maximize the effect. This limiting relationship is easily be determined from the definitions of the electric and magnetic susceptibilities.

$$P_i = \chi_{e,ij}E_j \tag{1.6}$$

$$M_i = \chi_{m,ij}H_j \tag{1.7}$$

since the magnetoelectric effect is dominated to first order, only the linear term is considered

$$M_i = \alpha_{ij}E_j \tag{1.8}$$

Then by substitution we have that

$$\alpha_{ii}^2 \leq \chi_{e,ii}\chi_{m,ii} \tag{1.9}$$

where χ_e and χ_m are the electric and magnetic susceptibilities. Hence, the magnetoelectric effect is expected to be large in ferroelectric and ferromagnetic materials. [24] Two classes of multiferroics that display large magnetoelectric coupling are composites, where the magnetoelectric effect is the product property of magnetostrictive

and piezoelectric materials, and single phase multiferroics, where the magnetoelectric coupling is intrinsic. Large magnetoelectric effects were observed in multiferroic bulk crystals and composites with the largest magnetoelectric response deriving from a system consisting of a ferroelectric piezoelectric and a ferromagnetic magnetostrictive metal. Since the 1970's, magnetoelectric materials and composite multiferroics have been used create a wide range of devices. Devices and applications such as: field sensing [25], current sensing [26, 27, 28], transformers [29, 30], amplifiers and gyrators [31, 32], tunable microwave devices [33, 34], spin wave signal processing [35], and antennas. [36] The demonstration of so many devices clearly exemplifies the interest and the importance of the magnetoelectric effect.

1.2.2 Multiferroics

The use of the magnetoelectric effect, discussed previously, has led to the demonstration of a wide variety of next-generation devices. These devices, however, have been demonstrated using bulk systems. With the need to provide solutions for micro- and nanoelectronics, multiferroics need to be in thin film form. Due to this reasoning, one of the big accomplishments of multiferroics research was the ability to produce thin films of single phase [37] and nanostructured composite [38] multiferroics. For instance, the discovery that single phase multiferroic $BiFeO_3$ could be grown in thin film form demonstrated that thin film, non-equilibrium phases of materials could be deposited and their properties could be tailored with epitaxial strain. [37] These latter facts have led to a renaissance of multiferroics research that was done in the 60's and 70's. Since the revival, researchers have proposed sensors [39], transducers, spintronics [40, 41] and heterogeneous read/write memory devices as the suggested technical implementations of thin film magnetoelectric multiferroics and some researchers have demonstrated that these applications are viable. Note that thin films lag behind the bulk studies as far as demonstrations of functional applications; however it is believed that thin films can be used for the same applications as bulk systems with the additional benefit of microelectronics integration.

The limited availability of single phase multiferroic materials originates from symmetry conflicts. In these compounds both time reversal and space inversion symmetries are broken to allow the establishment of magnetic and ferroelectric orders. The first discoveries of single phase magnetoelectric materials Cr_2O_3 (magnetoelectric) [18, 19, 20, 21, 22] and $Ni_3B_7O_{13}I$ (magnetoelectric multiferroic) [42], created the interest to pursue other multiferroic magnetoelectric materials with the hopes of understanding the unique coupling in these systems in addition to pursuing other materials with larger critical temperatures.

There are two classes of single phase magnetoelectric multiferroics: proper and improper. [43] Proper multiferroics are characterized with generally higher transition temperatures of the magnetic and electrical orders and the ordering of one parameter does not induce the ordering of the other parameter as with improper multiferroics.

$BiFeO_3$ is a proper magnetoelectric multiferroic and is the only well-established magnetoelectric multiferroic at room temperature. $BiFeO_3$ is a model multiferroic and because of it, has received much attention in both bulk crystal and thin film forms. [44, 45] The bulk phase is ferroelectric with a canted G-type antiferromagnetic structure in which a canted ferromagnetic moment forms a spin cycloid magnetic structure that propagates along one of the {110} directions. In the thin films, the spin cycloid is broken by the epitaxial strain, while preserving the G-type antiferromagnetism, and weak magnetic moment is stabilized. Like most single phase magnetoelectric multiferroics (due to the conflicting mechanisms that drive ferroelectricity and ferromagnetism) [46], $BiFeO_3$ is both ferroelectric and antiferromagnetic. Single phase multiferroics are typically criticized for the antiferromagnetic ordering is not ideal for spintronics applications. Furthermore, the coupling of the electrical and magnetic orders in proper multiferroics is typically mediated by the spin-orbit based Dzyaloshinskii-Moriya (DM) interaction. [47, 48, 49, 43] The DM interaction is an asymmetric, anisotropic exchange between two spins or magnetic moments (S_i) which are bonded neighbors in a lattice without an inversion center. The DM interaction is expressed as:

$$E = \vec{D_{ij}} \cdot (\vec{S_i} \times \vec{S_j}) \tag{1.10}$$

The direction of the DM vector ($\vec{D_{ij}}$) is governed by the symmetry of the lattice and is thus subjected to the following symmetry constraints [49]:

1. When there is an inversion center at the midway point of the line that connects $\vec{S_i}$ and $\vec{S_i}$,
$$\vec{D_{ij}} = 0 \tag{1.11}$$

2. When a mirror plane passes through the midway point of the line that connects $\vec{S_i}$ and $\vec{S_i}$ perpendicularly,
$$\vec{D_{ij}} \text{ lies in the mirror plane} \tag{1.12}$$

3. When there is a mirror plane that includes $\vec{S_i}$ and $\vec{S_i}$,
$$\vec{D_{ij}} \perp \text{ to the mirror plane} \tag{1.13}$$

4. When there is a two-fold rotation axis that passes through the midway point of the line that connects $\vec{S_i}$ and $\vec{S_i}$,
$$\vec{D_{ij}} \perp \text{ to the two-fold axis} \tag{1.14}$$

5. When there is a n-fold rotation axis ($n \geq 2$) along the line that connects $\vec{S_i}$ and $\vec{S_i}$,
$$\vec{D_{ij}} \text{ is parallel to the n-fold rotation axis} \tag{1.15}$$

In the case of $BiFeO_3$, the polar distortion is along the [111] direction and is responsible an axis of 3-fold rotational symmetry. The DM vector then points along this symmetry axis and the magnetic structure of $BiFeO_3$ is orthogonally coupled to this DM vector. [50, 51, 52] Thus by reorienting the polarization, it is possible to reorient the magnetic plane, either reorienting the antiferromagnetic structure or the canted moment. [53, 54]

While the magnetoelectric coupling of improper multiferroics is much larger than that of proper multiferroics, improper multiferroics are confined to low temperatures and are not considered a solution to the low magnetoelectric coupling of its single phase counterparts. Single phase multiferroics have unique advantages over improper and composite multiferroics in that they can exist at room temperature and intrinsically break time reversal symmetry, necessary ingredients to electrically driven magnetization reversal at room temperature.

1.3 Exchange coupling in ferromagnet - antiferromagnet heterostructures

Of additional importance to the understanding of this dissertation is a background in the manifestations and mechanisms of interface exchange coupling in ferromagnet-antiferromagnet heterostructures. Exchange coupling is an integral part of this thesis largely due to the fact that $BiFeO_3$ is the only well established room temperature multiferroic and has antiferromagnetic order. The push is for a room temperature demonstration of the electrical control of magnetism; however, since $BiFeO_3$ is antiferromagnetic, it is not easy to measure the magnetic properties. Furthermore, the active layers in magnetic devices are typically conducting and ferromagnetic. [55, 56, 57] This is to exploit the ease of resistance based measurements for applications and to use the significant spin polarization (spin dependent conduction channels) found in ferromagnets as the mechanism of electron scattering in these devices. [58, 59, 60] For these reasons, magnetoelectric mulitferroics have been proposed in structures where the antiferromagnetic multiferroic is in contact with an active ferromagnetic layer. [40, 41, 61] The primary visions of multiferroics in spintronic devices has been either to function as an electrically controllable tunnel barrier or an electrically controllable pinning layer. While there has been much recent success integrating multiferroics (and ferroelectrics) as electrically active tunnel barriers [62, 63, 64, 65, 66], the objective of the work presented in this dissertation has been to establish the electrical control of magnetism using the multiferroic as an electrically controllable pinning layer. Aside from device applications, the magnetization of the exchange coupled ferromagnet can be used to investigate the magnetic order of the antiferromagnet by essentially serving as a spin amplifier by tracking the direction of a weak moment or mapping the antiferromagnetic domain structure. Thus, a ferromagnet-antiferromagnet heterostructure can aslo be used as a scientific tool. In this dissertation, the ferromagnet-multiferroic

heterostructure is used for both the demonstration of a potential application and the investigation of the multiferroics magnetic structure.

Throughout this dissertation, the relevant magnetic anisotropies will be discussed. How these different magnetic anisotropies alter the magnetic properties and the energy landscape of the magnetization is important for the understanding the quasi-statics of magnetic materials and heterostructures. For this reason, the model for determining the orientation of a magnetization from energy considerations is first discussed.

1.3.1 Stoner-Wohlfarth model

The Stoner-Wohlfarth model is developed by the name sakes to model quasi-static magnetic processes. [67, 68] The model considers energy terms from the applied magnetic field (Zeeman energy) and any revelent magnetic anisotropy energies (i.e. those resulting from strain, magnetic field annealing, crystallinity, etc). The energy is expressed as if the magnet were a single magnetic moment (or monodomain) and thus the Stoner-Wohlfarth model does not account for domain formation and domain wall motion. As a consequence, it will over predict coercive field values of multidomain films.

As an example, lets consider a single domain magnet with uniaxial anisotropy.

$$E_V = -\mu_0 H_a M_f cos(\theta_a - \theta) + K_u sin^2(\theta_u - \theta) \tag{1.16}$$

The first term is the Zeeman energy and the second is the uniaxial anisotropy term. μ_0 is the permeability of free space, H_a is the applied magnetic field, M_f is the magnetization of the magnetic film and K_u is the uniaxial anisotropy strength. The angles θ, θ_a, and θ_u are the angle of the mangetization, angle of the applied field, and the angle of the uniaxial anisotropy all with respect to the same reference direction.

To determine where the magnetization will point (i.e. θ), the stability condition must be applied to the equation of state (E_V). This requires:

$$\frac{\partial E_V}{\partial \theta} = 0 \tag{1.17}$$

$$\frac{\partial^2 E_V}{\partial \theta}^2 > 0 \tag{1.18}$$

This leads to the following relations:

$$-\mu_0 H_a M_f sin(\theta_a - \theta) + 2K_u sin(\theta_u - \theta) cos(\theta_u - \theta) = 0 \tag{1.19}$$

$$\mu_0 H_a M_f cos(\theta_a - \theta) - 2K_u cos^2(\theta_u - \theta) + 2K_u sin^2(\theta_u - \theta) > 0 \tag{1.20}$$

Solving these relations yeilds the angle θ. From here magnetic hysteresis loops can be modeled with the knowledge that the measured moment in magnetometry is the

longitudinal component of the magnetization ($M_{long} = M_f \cos(\theta_a - \theta)$). The coercive field can also be calculated from the first of the stability criteria.

Additionally, magnetization dependent conductivity measurements can aslo be modeled using this model. For instance, the anisotropic magnetoresistance observed in ferromagnetic materials is expressed as

$$R(\theta) = R_0 + \delta R cos^2(\theta - \theta_I) \tag{1.21}$$

Using the Stoner-Wohlfarth model to obtain θ, the anisotropic magnetoresistance of a magnetic sample can be modeled.

Other systems that possess anisotropies other than a simple uniaxial anisotropy can also be considered. While the model may become a more complicated, the competition between anisotropies can be understood.

1.3.2 Meiklejohn-Bean Model

The interest in ferromagnetic-antiferromagnetic heterostructures occurs from the initial discovery of exchange bias by Meiklejohn-Bean in 1956 [69] and its pervasive use in the magnetic read heads found in computer hard drives. [70, 71] Exchange bias manifests as a shift (either positive or negative) in the ferromagnetic hysteresis loop of the ferromagnetic-antiferromagnetic heterostructure, breaking the symmetry about zero magnetic field. [72] The phenomenological description of exchange bias is illustrated in Figure 1.5. Figure 1.5(1) shows the magnetic hysteresis and spin configuration of a ferromagnet-antiferromagnetic heterostructure at a temperature above the ordering temperature of the antiferromagnet but below the ordering temperature of the ferromagnetic layer. The antiferromagnetic layer is in a paramagnetic state at this temperature and thus the magnetic hysteresis is dominated by the ferromagnet, yeilding the typical feromagnetic hysteresis.

As the sample is cooled below the antiferromagnetic critical temperature (T_N) while under a magnetic field (H_{FC}), the antiferromagnetic spins order along the axis of the applied magnetic field. Figure 1.5(2-5) show the magnetic hysteresis and spin configuration of the heterostructure below the ordering temperature of the antiferromagnet. Illustration 2 shows the spin configuration at the cooling field. The field orders the antiferromagnetic spins along this axis, with all of the spins at the antiferromagnetic surface pointing along the field direction and direction of the ferromagnetic moments. It is assumed that the exchange bias interaction occurs at the interface of the ferromagnetic and antiferromangetic layers. As the field is applied in the negative direction, at a value significant enough to cause switching (illustration 3), the ferromagnetic spins begin to collectively rotate while the spins in the antiferromagnet remain fixed. This continues out to larger negative field to the point where the ferromagnetic spins point along the field direction and antiparallel to the antiferromagnetic spins at the interface. One the reversed field sweep, the ferromagnetic spins

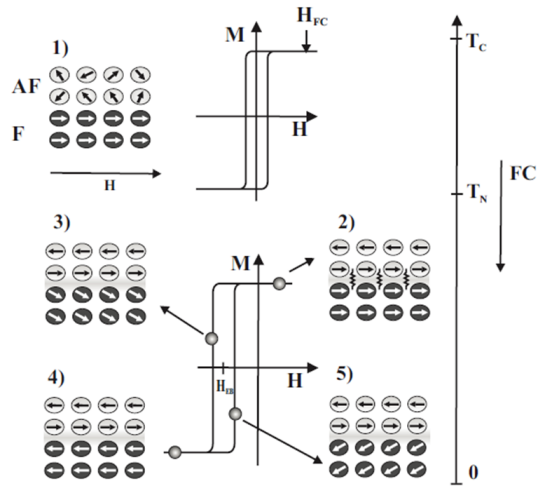

Figure 1.5: Phenomenological model of exchange bias. Figure 1 shows the high temperature spin configuration and magnetic response. Figures 2-5 show the magnetic response and the spin configurations at several points as in the magnetic hysteresis, taken after cooling below the Néel temperature in a magnetic field. Taken from [79].

begin to switch and even return to a parallel configuration with the antiferromagnetic spins at the interface before a positve field value is reached as if an internal magnetic field were present. This early switching is driven by the interaction between the ferromagnetic and antiferromagnetic spins at the interface which prefer a parallel configuration to minimize the interface exchange energy.

This phenomenological model was proposed by Meiklejohn-Bean in 1956 [69]. They were able to correctly assess that the exchange bias effect was a new source of magnetic anisotropy and then used a Stoner-Wohlfarth model with an additional anisotropy term to predict exchange bias fields. The additional anisotropy term they added was of the form of a magnetic field ($\cos\theta$ dependence) since it manifests in the loop as a magnetic field. Since the interaction was assumed to be from the interface, the mathematical expression to determine the state of the system is given by the energy per unit area:

$$E_A = -\mu_0 H_a M_f t_f cos(\theta_a - \theta) + K_u t_f sin^2(\theta_u - \theta) - J_{ex} cos(\theta_{ex} - \theta) \tag{1.22}$$

where t_f is the thickness of the ferromagnetic layer, J_{ex} and θ_{ex} are the strength and direction of the effective exchange field. The stability conditions require:

$$-\mu_0 H_a M_f sin(\theta_a - \theta) + 2K_u sin(\theta_u - \theta) cos(\theta_u - \theta) - J_{ex} sin(\theta_{ex} - \theta) = 0 \tag{1.23}$$

$$\mu_0 H_a M_f cos(\theta_a - \theta) - 2K_u cos^2(\theta_u - \theta) + 2K_u sin^2(\theta_u - \theta) + J_{ex} cos(\theta_{ex} - \theta) > 0 \tag{1.24}$$

Solving these equations for the coercive and exchange fields leads to the useful relationships:

$$H_c = \frac{2K_u}{\mu_0 M_f} \tag{1.25}$$

$$H_{ex} = -\frac{J_{ex}}{\mu_0 M_f t_f} \tag{1.26}$$

There are a few interesting points to note from these equations. The first is that both the coercive and exchange bias fields are inversely proportional to the saturation magnetization of the ferromagnet. Secondly, the coercive field is directly proportional to the anisotropy of the ferromagnetic layer. Note that the strength of the antiferromagnetic anisotropy is not considered directly in this model and thus does not have an influence on the coercive field. Thirdly, the sign of the exchange bias is determined by the sign of J_{ex}. In the case of Co/CoO and Co/CuMn, the exchange bias is positive [73, 74], however, in FeF_2 the sign of the exchange bias can be both positive and negative, depending on the cooling field. [75, 76] Lastly, the exchange bias field scales inversely with the thickness of the ferromagnetic layer. This is considered to be one of the tradtional signs of exchange coupling in these bilayer systems and has been extensively invesigated in the Co/CoO systems [77, 78, 72].

While this model was able to qualitatively explain the observed anisotropy, it was immediately known to make bias field predictions 1-2 orders of magnititude larger than observed values. [69] The Meiklejohn-Bean model makes several assumptions about the system which may be the cause of the large over predictions of the model.

1. The ferromagnetic layer rotates as a whole, no formation of a domain wall or partial domain wall.

2. Both magnetic layers are monodomain.

3. The interface is atomically flat.

4. The interface of the antiferromagnet is fully uncompensated, and thus has a surface magnetic moment.

5. The antiferromagnetic spins are rigid and do not rotate during the process or cant.

6. A higher order magnetic anisotropy of the antiferromagnet is not considered.

7. The effect is strictly an interface effect, no consideration of the bulk order.

Additional anisotropies and magnetic moments can be added to address some of these issues. In the next section, the antiferromagnetic anisotropy and moment will be considered in this Stoner-Wolfarth type model. This addition can not only predict

exchange bias, but also predicts another manifestation of exchange coupling known as exchange enhancement. This advanced Stoner-Wolfarth model and other proposed mechanisms of exchange bias are considered in the next two subsections.

1.3.3 Exchange bias and exchange enhancement

The prediction of the two macroscopic manifestations of exchange coupling can be predicted using a Stoner-Wohlfarth model that includes an anisotropy term for the antiferromagnet. [79, 72, 80] The equation used in [79] is given as:

$$E_A = -\mu_0 H_a M_f t_f cos(\theta_a - \theta) + K_{u,f} t_f sin^2(\theta_{u,f} - \theta)$$
$$+K_{u,af} t_{af} sin^2(\theta_{u,af} - \beta) - J_{ex} cos(\theta - \beta) \quad (1.27)$$

Here the antiferromagnetic spins are characterized by the angle β and are assumed to have a uniaxial anisotropy. In this case, the stability condition must be met for both the ferromagnet and the antiferromagnet, leading to the system of equations [79]:

$$\frac{H}{H_{ex}^{MB}} sin(\theta_a - \theta) + sin(\theta - \beta) = 0 \quad (1.28)$$

$$Rsin(2\beta) - sin(\theta - \beta) = 0 \quad (1.29)$$

where

$$H_{ex}^{MB} = -\frac{J_{ex}}{\mu_0 M_f t_f} \quad (1.30)$$

$$R = \frac{K_{u,af} t_{af}}{J_{ex}} \quad (1.31)$$

The distinguishing physical parameter in this model is the R parameter, which is the ratio of the antiferromagnetic anisotropy energy to the interface exchange energy. In fact, three distinct regions of magnetic response can be found based on this parameter. [79, 81, 80, 82]

1. When R $\geq$ 1. In this region the antiferromagnetic anisotropy is much stronger than the interface exchange energy. In this situation the exchange bias follows the prediction made by the Meiklejohn-Bean model when R = ∞ (no rotation of β). In this region, the antiferromagnetic spins rotate reversibly and the rotation angle is set by the size of R. The exchange bias is smallest when R = 1. See Figure 1.6.

2. When 1/2 $\leq$ R < 1. The coercive field is non-zero and has a strong R dependence while the exchange bias is zero. Furthermore, the antiferromagnetic spins rotate hysteretically (irreversibly) with the coupled ferromagnetic magnetization. The discontinous jumps in β are seen in the modeled magnetic hysteresis loops.

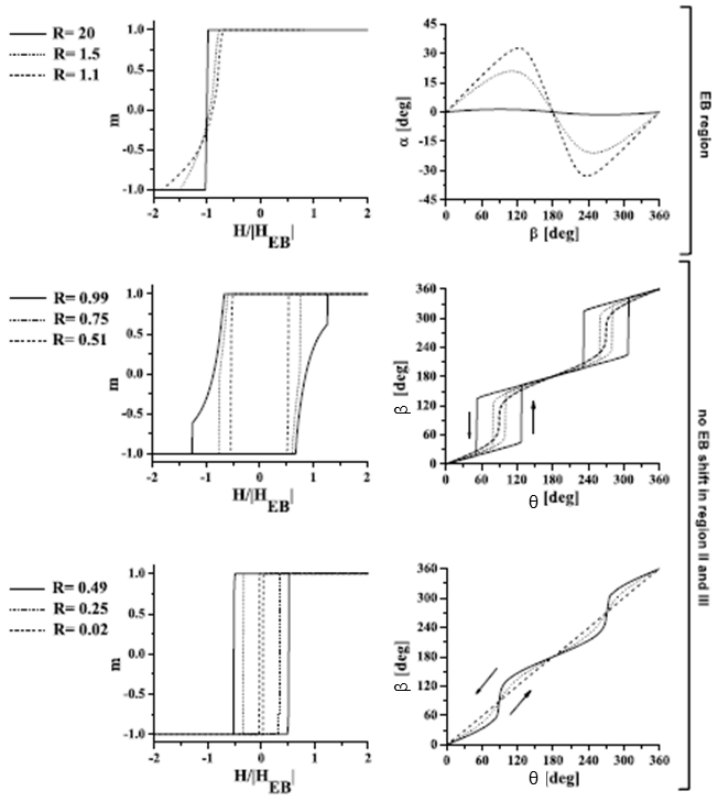

Figure 1.6: (Left) Simulations of the magnetic hysteresis loops for the 3 different regions of R. (Right) The corresponding rotation of β as the magnetization (θ) is rotated. Taken from [79].

3. When R $< 1/2$. In this region there is no irreversible switching of the antiferromagnetic spins, rather they rotate smoothly with the ferromagnet magnetization. Again, there is no exchange bias but a coercive field is present. In this region the coercive field varies as, $H_c \propto \frac{2K_{u,af}t_{af}}{\mu_0 M_f t_f}$ and thus the width of the ferromagnetic hysteresis is no longer dependent on the anisotropy of the ferromagnetic layer but rather the antiferromagnetic layer. This is an important realization largely due to the fact that the anisotropy energy of antiferromagnets are typically larger than that of ferromagnets. Thus we should expect that the coercive field of a ferromagnet should be enhanced or broadened when it is in contact with an antiferromagnet. Aside from exchange bias, this is the other manifestation of exchange coupling in an ferromagnetic-antiferromagnetic heterostructure and is an important realization when considering the $Co_{.90}Fe_{.10}$ / $BiFeO_3$ heterostruture.

Model Name	Direct coupling (uncompensated)	Spin-Flop coupling (fully compensated)	Properties
Meiklejohn and Bean (Direct exchange).	X		Orders of magnitude off. If # pinned moments small, then ok.
Mauri (AFM spring).	X		Realistic values, relies on thick AFM layer, longitudinal AFM DW walls.
Malozemoff (random field).		X	Realistic values, relies on surface roughness, laterial AFM DW walls.
Koon (spin flop).		X	Relies on easy plane AFM (bad assumption).
Seuss (Interacting Grain Model).		X	Complicated, relies on interaction between grains with random anisotropy and lateral AFM DW formation.

Figure 1.7: Different mechanisms of exchange bias. The mechanisms are distinguished by whether the mechanism describes the coupling at an uncompensated (Meiklejohn-Bean and Mauri) or compensated (Malozemoff, Koon-Butler, and Suess) surface.

1.3.4 Other models of interface exchange

The Meiklejohn-Bean model has been criticized for over predicting the value of exchange bias. Furthermore, it bases its prediction on coupling to a fully uncompenstated surface of the antiferromagnetic layer and further predicts that the exchange bias with a fully compensated surface should be zero. As a result, other models of exchange bias were developed to understand the mechanism of reduced exchange bias and exchange bias observed with fully compensated surfaces. The other models of exchange bias are listed in Figure 1.7. In addition to the Meiklejohn-Bean model, the Mauri model was developed using uncompensated surfaces while making more realistic predictions of exchange bias fields. The other three models of exchange bias were developed to understand the mechanism behind the observed exchange bias found in heterostructures with a fully compensated antiferromagnetic surface. Figure 1.7 also highlights each model. The Suess model will not be reviewed here since we are concerned with single crystal antiferromagnetic specimens.

Mauri model

The Mauri model, proposed in 1987, is a model of exhange bias that considers a flat, fully uncompenstated, antiferromagnetic surface. [83] The Mauri model is an attempt to gain a better quantitative understanding of exchange bias. The Mauri model proposes that the antiferromagnetic structure is rigid and will rotate to form a domain wall in the antiferromagnet as the ferromagnetic spins are rotated. An illustration of the process is given in Figure 1.8. The spins in the antiferromagnet, at the ferromagnet-antiferromagnet interface, follow the spins in the antiferromagnet while the spins at the other end of the antiferromagnet remain fixed. This forms a domain wall parallel to the ferromagnet-antiferromangetic interface. Using a Stoner-Wohlfarth model, however, this time adding an energy term for the formation of a domain wall in the antiferromagnet leads to an energy per unit area of the form [79]:

$$E_A = -\mu_0 H_a M_f t_f cos(\theta_a - \theta) + K_{u,f} t_f sin^2(\theta_{u,f} - \theta) - J_{ex} cos(\theta_- \beta) \\ +2\sqrt{A_{af} K_{af}}(1 - cos(\beta)) \tag{1.32}$$

where the last term is the energy required to form the domain wall or partial domain wall and A_{af} is the exchange stiffness in the antiferromagnetic layer. Thus the exchange bias field will be expressed as

$$H_{ex} = \frac{\delta E_{DW}}{2\mu_0 M_f t_f} = \frac{\sqrt{A_{af} K_{af}}(1 - cos(\beta))}{\mu_0 M_f t_f} \tag{1.33}$$

Malozemoff model

The Malozemoff model was proposed in 1987. Here, the exchange anisotropy was postulated to be due from a randomization of the local exchange interactions. [84, 85, 86] More importantly, it highlights the influence of defects. An illustration of the Malozemoff random field model (roughness model) is shown in Figure 1.9. Figures 1.9(a-c) show the number of frustrated local exchange interactions at the ferromagnet-antiferromagnet interface (marked by the x) due to an imperfect surface. Figure 1.9(a) shows the number of frustrations due to a surface imperfection at a site that preserves the antiferromagnetic order. 5 frustrated interactions are created in such an arrangement. In Figure 1.9(b), the antiferromagnetic state is broken creating a frustrated magnetic interaction in the antiferromagnet, however, the number of frustrated interactions at the interface is reduced to 2. Clearly, the lowest energy case is that which is shown in Figure 1.9(c). In the case where the antiferromagnetic exchange in the antiferromagnet is preserved and frustrated interactions due to surface imperfections are 0. In this case, the surface imperfection actually reduces the overall energy (compared to a perfect surface) by reducing the number of frustrated interface interactions that would be found at a perfect interface. This means that there is a

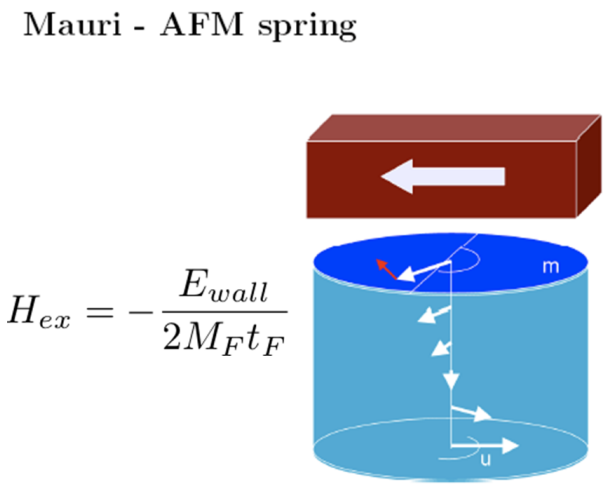

Figure 1.8: Illustration of the Mauri model mechanisms of exchange bias. The model describes the formaton of a domain wall in the antiferromagnet as the cause for the preferential direction of the magnetization. The exchange bias field can be estimated by the cost in energy to form the domain wall.

preferred order to the antiferromagnet and the ferromagnet which is the ultimate driver of the exchange bias. Figure 1.9(d) illustrates the global effect of a random surface roughness. In this case it is preferential for the antiferromagnet to break up into domains, if necessary, to promote the condition observed in (c) since this configuration is significantly lower in energy than the other two alternatives.

Koon-Butler model (spin-flop coupling)

Koon reported a microscopic explanation of exchange bias at fully compensated antiferromagnetic interfaces. His calculations showed that it was energetically preferred for the antiferromagnet to cant, creating a small ferromagnetic moment that the coupled ferromagnetic magnetization would couple to. This is schematically illustrated in Figure 1.10. The effect creates a perpendicular orientation between the ferromagnetic and antiferromagnetic axes.[87]

This canted moment will couple to the ferromagnet and leads to spin-flop like interaction. Using this energy, the Stoner-Wohlfarth energy becomes:

$$E_A = -\mu_0 H_a M_f t_f cos(\theta_a - \theta) + K_{u,f} t_f sin^2(\theta_{u,f} - \theta) - J_{ex} cos(\theta - \beta)$$
$$+2\sqrt{A_{af} K_{af}}(1 - cos(\beta)) + J_{sf}(M_f M_c)^2 cos^2(\theta - \beta) \quad (1.34)$$

where the last term is the spin-flop coupling term.

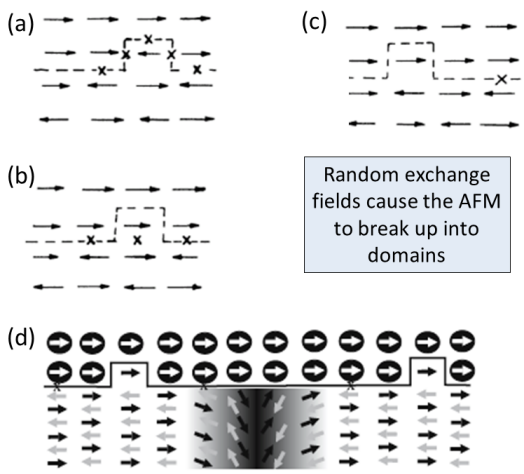

Figure 1.9: Illustration of the Malozemoff model of exchange bias. The model describes exchange bias through the formation of vertical domain walls in the antiferromagnet to reduce a possible high energy coupling state at the interface due to surface roughness. Taken from [84].

Koon proposed that this mechanism would result in an exchange bias anisotropy, largely due to the mechanism being Mauri-like, in that it requires the partial longitudinal domain wall formation in the antiferromagnet. [87] In 1998 Butler and Schulthess [88] performed microscopic exchange calculations that included magnetostatic interactions. When perfectly flat interfaces were considered, the spin-flop coupling did not show exchange bias. They determined that the canted ferromagnet moment would switch between its degenerate states before a domain wall in the antiferromagnet is formed. Butler's calculation did however show that this induced a large uniaxial anisotropy in the ferromagnet which gives rise to the large coercive fields (exchange enhancement). [88] To predict an exchange bias, a Malozemoff (surface roughness) component was required in the model.

1.3.5 Additional mechanisms of induced anisotropy

There are several other ways to induce a magnetic anisotropy into a ferromagnetic layer. The magnetic anisotropy is largely dominated by the spin-orbit interaction in the ferromagnetic material. Thus, a magnetic anisotropy can be induced into the ferromagnetic system with any external parameter which can influence the spin-orbit interaction. This could be a magnetic field, electric field, and stress amoungst other possibilities. In most cases a magnetic field is applied during the growth of ferromagnetic layers to induce a uniaxial magnetic anisotropy. The magnetic field induced anisotropy (or magnetic annealing) will be discussed due to its use in this

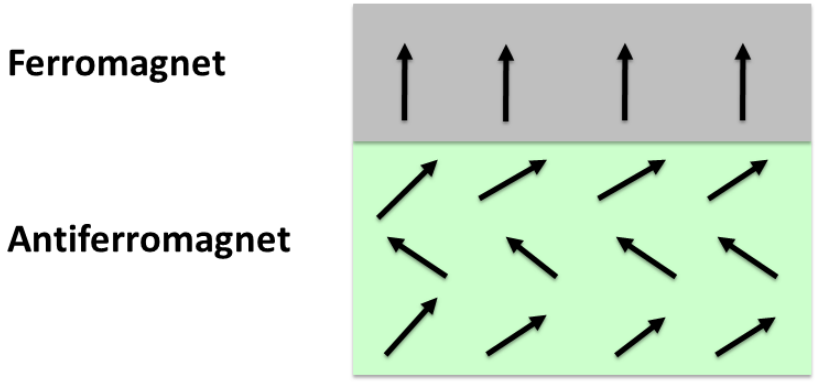

Figure 1.10: Illustration of the Koon-Butler model of exchange bias, which is more commonly known as spin-flop coupling. The model describes exchange bias through the formation of a canted magnetic moment in the antiferromagnet to reduce the overall energy.

dissertation. Additionally, it is important to consider other mechanisms by which an magnetic anisotropy can be induced into a ferromagnetic layer. $BiFeO_3$ is also ferroelectric and ferroelastic, meaning that there is a stress along the axis of the ferroelectric polarization. This stress could induce be a source of magnetic anisotropy in a feromagnetic-multiferroic heterostructure. Stress induced magnetic anisotropy will briefly be discussed here as well.

Magnetic annealing

When a magnetic field is applied to a magnetic material at high temperature or during a growth process like sputtering, where the atoms have large effective temperatures, and short range diffusion is possible, the magnetic field can induce several microscopic effects. The effects are as follows [89]:

1. The directions of bonds between similar and dissimilar species make take on aysmmetric ordering (also known as directional pair ordering). This is the most dominant effect of magnetic annealing. Typically this mechanism is found in the annealing of polycrystalline and amorphous alloys.

2. If the interation between one species is much larger than its interaction with another, atoms of the minority species may coalesce into fault planes.

3. An applied magnetic field can have the strenth to physically reorient structural features of magnetic materials and thus can have a significant influence over the microstructure of the material. This could influence the macroscopic magnetic anisotropy if the magnetic field can create a texturing.

4. In two phase alloys, a textured or anisotropic structure may evolve.

Since the mechanism of directional pair ordering is the most dominant and likely to be cause of anisotropy in amorphous films, only this mechanism will be discussed in further detail.

The bonding of atoms in an alloy can be preferential if the interaction energies between species are different and if the atomic radii are significantly different. The ordering of the species will be such to reduce the bonding energy and the local magnetostriction will determine the direction of the magnetization. An applied magnetic field forces the magnetization of the sample along this direction. The local magnetostrictive energy will be minimize if the boding stress is either along or orthognonal to the magnetization direction depending on the sign of the magnetostriction coefficient (λ_s). The minimization of the local magnetostriction energy will preferentially order the bonding. Once the sample is cooled and the bonds are set, the macroscopic effect is a induced uniaxial anisotropy.

The strength of this effect can be estimated by calculating the magnetocrystalline, strain, and magnetostrictive energies at the local scale. Considering an binary alloy of $A_{1-x}B_x$ and the above energies, the strength of the field induced anisotropy varies as:

$$K_u \propto \frac{1}{k_B T_a}\left[\frac{M_s(T_a)}{M_s(0)}^2\right]\left[\frac{M_s(T)}{M_s(0)}^2\right] x^2(1-x)^2 \tag{1.35}$$

where T_a is the annealing temperature, M_s(T) is the saturation magnetization at the given temperature and x is the fraction of the B constituent in atomic percent [89]. In the dilute limit, x is much less than 1, the anisotropy strength varies as x^2. The angular dependence of the varies as a uniaxial anisotropy with the preferential axis being set by the direction of the anealing or growth field. Mathematically, this anisotropy is expressed as:

$$E_V = K_u sin^2(\theta - \theta_{anneal}) \tag{1.36}$$

where θ and θ_{anneal} are the angles of the magnetization and the annealing field with respect to a common reference. Thus the magnetization favors a collinear alignment with the axis set by the annealing field.

Since the work presented in this dissertation heavily relies on thin sputtered films of $Co_{.90}Fe_{.10}$ that are grown in a 200 Oe magnetic field, the induced anisotropy was measured by taking magnetic hysteresis loops along and orthogonal to the magnetic field applied during the growth of the film (see Figure 1.11). The loop along the growth field direction shows a clear hysteretic opening and sharp switching between M_s and -M_s states, confirming that the axis of the growth field is the magnetic easy axis. Orthogonal to the growth field direction, the magnetic hysteresis shows no opening and no sharp switch, rather a smooth transition between M_s and -M_s

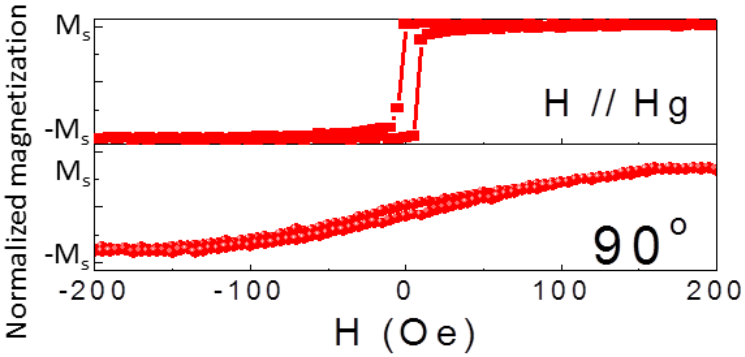

Figure 1.11: Magnetic hysteresis loops of a 2.5nm $Co_{.90}Fe_{.10}$ film that was grown on an non-magnetic substrate ($SrTiO_3$) under a 200 Oe magnetic field. Loops taken along the growth field direction show the easy axis behavior (sharp switching and clear opening). Orthogonal to the growth field direction displays hard axis behavior (no sharp switching and no opening).

states, and confirming the hard axis behavior. The anisotropy of the loops confirms the induced uniaxial magnetic anisotropy is induced in our $Co_{.90}Fe_{.10}$ films by the magnetic growth field. I will use this fact in chapter 3 to test the interface coupling between $Co_{.90}Fe_{.10}$ and $BiFeO_3$.

Stress annealing

When a stress is applied to a material, an anisotropic ordering in the material can occur when the atoms have enough energy to quickly diffuse. This can be during a growth process like sputtering, where the atoms have large effective temperatures. The exact nature of the anisotrpoy will be alloy dependent, but regardless, an anisotropy will develop from a preferential ordering either along or perpendicular to the stress axis. In the case of a magnetic material, the anisotropic ordering or bonding will change the local spin orbit interaction and ultimately creates a macroscopic magnetic easy axis for the magnetization. Stress annealing can also be viewed as an inverse magnetostriction effect (Villari effect). The energy relationship of the Villari effect can be expressed as $E = \frac{3}{2}\lambda_s \sigma \sin^2\theta$. An elongation of the magnetic material will cause the magnetization to orient along the stress axis if λ_s is positive and orthogonal to the stress axis if λ_s is negative and in both cases the induced anisotropy is uniaxial.

The stressed induced magnetic anisotropy can be significantly larger than the anisotropy induced by magnetic annealing. In the case of a solid solution of $Fe_{.22}Al_{.78}$, it was foung that a stress of 140MPa produces an easy axis along the stress; having a anisotropy constant of 170x10^3 J/m^3 (twice as large as the anisotropy constant obtained from field annealing. [90] Likewise, a stress induced anisotropy can influence

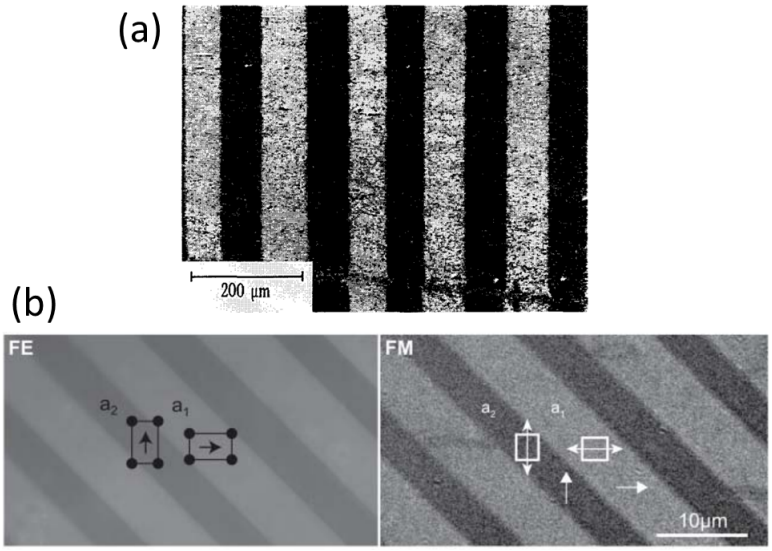

Figure 1.12: Laminar stripe domain structure induced by stress (a) in a nanocrystalline FeCuNbSiB alloy the where the induced magnetic anisotropy is arranged transverse to the stress direction, that is, parallel to the easy magnetic direction. Taken from [91] (b) Ferroelectric (FE) domain pattern of $BaTiO_3$, showing the two ferroelectric domain variants. The ferrmagnetic domain structure of the $Co_{.60}Fe_{.40}$ layer closely follows the domain structure of the $BaTiO_3$ due to the large magnetostriction coefficient of this particular composition of CoFe. Taken from [94].

the magnetic domain structure of the material. In the cases of the nanocrystalline FeCuNbSiB alloy and a 15nm $Co_{.60}Fe_{.40}$ layer on ferroelectric $BaTiO_3$, laminar striped domain structures were observed (see Figure 1.12). In the case of the FeCuNbSiB alloy, the stress determined the easy axis, which is along the length of the striped domains, however, the stripes form due to the minimization of the magnetostatic energy. [91]

In the case of the $Co_{.60}Fe_{.40}$ layer on ferroelectric $BaTiO_3$, the large magnetostriction and small magnetocrystalline anisotropy of the $Co_{.60}Fe_{.40}$ layer [92, 93] causes it to couple to the stress in each ferroelectric domain. [94] Since the ferroelectric domains have a laminar striped structure, the $Co_{.60}Fe_{.40}$ layer adapts the same magnetic domain structure. Note here that the laminar structure formed in this structure is not created by magnetostatics but rather by the laminar domain structure of the ferroelectric.

1.4 Organization of the dissertation

The remainder of this dissertation is organized as follows:

Chapter 2 is a compilation of the previous work towards the electric field control magnetism using the room temperature multiferroic $BiFeO_3$. The focus of this chapter not only be to summarize the knowledge gained by past experiements but to also highlight the difficulties and challanges faced in these experiments. Highlighted will be the dependence of manifestation of the interface exchange coupling on the $BiFeO_3$ domain structure and interface quality. Lastly, the electric field control of antiferromagnetic domains, the electric field control of ferromagnetism using nanopillars and a thin metallic layer will highlight the importance of symmetry.

Chapter 3 will begin with the investigation of the exchange coupling between a ferromagnetic metal and $BiFeO_3$. I present the evidence for the one-to-one domain coupling between ferromagnetic $Co_{.90}Fe_{.10}$ and a (001) oriented 2-variant $BiFeO_3$ film that is composed of long 71^o striped domains. The discussion and the results in this chapter will emphasize the importance of domain coupling rather than domain wall coupling for the electric field control of ferromagnetism.

Chapter 4 will discuss the electric field control of ferromagnetism using an in-plane electric field. Presented in the chapter is the use of the one-to-one domain coupling between ferromagnetic $Co_{.90}Fe_{.10}$ and a (001) oriented, 2-variant $BiFeO_3$ film, discussed in chapter 3, to enable the magnetization reversal of the net $Co_{.90}Fe_{.10}$ magnetization in a device architecture. The local ferroelectric and magnetoelectric switching are determined through magnetotransport and piezoresponse force microscopy measurments. The chapter ends with a discussion that motivates the pursuit of the electric field control of magnetism using an out-of-plane electric field.

In chapter 5 I will show that the net magnetization of the $Co_{.90}Fe_{.10}$ can be reversed in this heterostructure with an out-of-plane voltage. This reversal only

requires the application of a single digit voltage. The anisotropic magnetoresistance is used to reveal this reversal and its reversibility. Domain imaging after the electrically induced reversal shows that the striped 2-variant domain structure is preserved after the switch. At the end of the chapter I will motivate the electric field control of a traditional spintronic device (spin valve), which is the topic of the proceeding chapter.

Chapter 6 presents the evidence for the electric field control of a spintronic device. Using magnetotransport measurements to correlate the orientation of the magnetic layers with respect to one another, the orientation of the magnetization as a function of the applied voltage to the $BiFeO_3$ film is determined. The resistance state of the spin valve device is shown to switch from low to high resistance states (magnetizations parallel to antiparallel) with a single digit voltage. Furthermore, it will be noted that no where in the writing or readout of the device is an external magnetic field required.

Chapter 7 briefly summarizes this entire dissertation and leaves the reader with suggeted directions for future investigations in this area of research.

Chapter 2

Previous work

This chapter summarizes the relevant work performed on $BiFeO_3$ and $BiFeO_3$ heterostructures with a ferromagnetic metal. It was found that the ferroelectric domain structure of the $BiFeO_3$ film could easily be controlled with epitaxial growth conditions. Films with different fractions of the three possible domain walls could all be achieved by tuning the growth conditions. In addtion to $BiFeO_3$ having 3 macroscopic order parameters, these studies highlighted the heavy correlations in $BiFeO_3$ with the observations that the three possible domain walls in $BiFeO_3$ are all varying degrees of magnetic and conductive. Early work on the magnetic exchange coupling with a ferromagnetic metal primarily focused on using a single epitaxial condition imposed on the $BiFeO_3$ which displayed 4 or 8 different domain variants with each variant having 3 macroscopic order parameters. Additionally, the 4 and 8 variant films have different mixtures of all 3 possible domain walls. This convolutes the interpretation of the mechanism of the magnetic exchange coupling. Despite this heavy convolution, it was still determined that $BiFeO_3$ films with a high degree of 109^o domain walls showed both an enhanced coercivity of the ferromagnetic layer and also an asymmetry of the magnetic hystersis. If was also found that the size of the asymmetry scaled with the length of the 109^o domain walls. However the mechanism for the coercivity enhancement was unknown. The electric field control of magnetism was shown using a $Co_{.90}Fe_{.10}$ / $BiFeO_3$ heterostructure as well as a $CoFe_2O_4$ / $BiFeO_3$ nanopillar structure. The former exploited the magnetic interface exchange coupling, which can break time reversal symmetry, while the latter was a strain/lattice-distortion mediated effect. The results of which highlights the fact that to reverse a magnetization, time reversal symmetry must be broken.

2.1 Introduction to $BiFeO_3$

$BiFeO_3$ has been investigated since the late 1950's and recieved much attention for the same reason that it recieves so much today. That is, the interest is in the

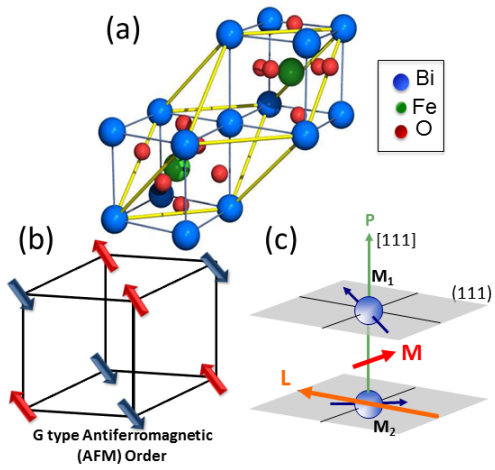

Figure 2.1: (a) Schematic of the rhombohedral $BiFeO_3$ unit cell (outlined in yellow). The unit cell can be pictured in a pseudo-cubic structure which is outlined in blue. Two pseudo-cubic structures are needed to describe the rhombohedral unit cell. (b) Schematic of the magnetic lattice of $BiFeO_3$, G-type antiferromagnetism (all nearest neighbor spins are antiparallel). The Fe spins reside in the pseudo-cubic (111) plane. (c) Schematic of the arrangement of the macroscopic order parameters (P, L, and M) of thin film $BiFeO_3$.

magnetoelectric coupling of its macroscopic order parameters. [95] These early studies investigated bulk crystals of $BiFeO_3$, in contrast to much of today's work which is dominated by $BiFeO_3$ thin film research. Early on, the crystal structure of $BiFeO_3$ was determined to be a rhomboherally distorted perovskite [96, 97] with a ferroelectric hysteresis [98] and G-type antiferromagnetic lattice with a small canted moment that forms a long range spin spiral [99, 100].

Figures 2.1(a) and (b) show the rhombohedrally distorted perovskite cystal structure and G-type antiferromagnetic order of $BiFeO_3$. Figure 2.1(a) shows the $BiFeO_3$ crystal structure in two different bases. The crystal structure outlined in yellow is the the rhombohedral unit cell, while the structure outlined in blue is a pseudo-cubic structure. In recent literature, the crystal axes and planes are typically referred to in the pseudo-cubic basis. In this thesis, all references to crystal directions and planes will be made in the pseudo-cubic basis. The ferroelectric polarization points along the direction of the rhombohedral distortion (the [111] direction) and a T_c near 1100K. [98] Figure 2.1(b) shows the antiferromagnetic structure of $BiFeO_3$. $BiFeO_3$ has been determined to have a G-type antiferromagnetic order in both thin films and in bulk crystals [101, 53], where all nearest neighbor spins point (arrows represent Fe spins) antiparallel to one another and the (111) planes are ferromagnetically aligned, and a Néel temperature of 643K. Additionally, it was found in the bulk that the antiferromagnetic order would rotate around the <110> directions with a period of 62nm.

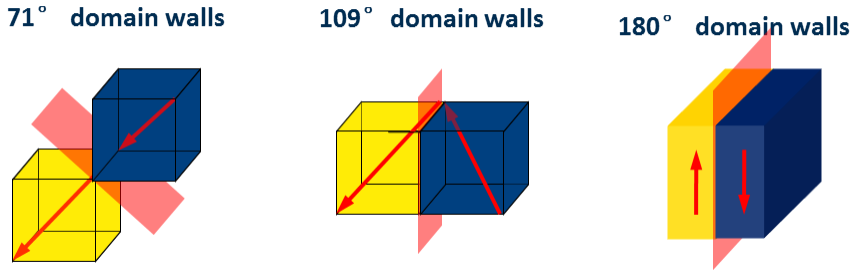

Figure 2.2: Schematics illustrating the three possible domain walls permitted in $BiFeO_3$ and other rhombohedral ferroelectrics. The domain walls are distinguish by the angle of rotation made by the polarization going from one domain to the next.

[100] Furthermore, symmetry also permits the formation of a weak magnetic moment through a canting of the antiferromagnetic lattice. The canted moment flows the rotation and period of the antiferromagnetic spin cycloid. [102, 103] In thin films, however, the spin cycloid is broken given rise to a homogenous canted moment and antiferromagnetic axis. [104] Figure 2.1(c) is a schematic that illustrates the configuration of the polarization (P), antiferromagnetic vector (L), and the canted moment (M) in the thin film limit. The polarization is oriented along the [111] direction while the magnetic vectors are confined to the (111) plane, with all three vectors being mutually orthogonal. [51] The antiferromagnetic vector, L, is defined by M_1 - M_2 and the canted moment, M, is defined by M_1 + M_2.

Since $BiFeO_3$ is a rhombohedral ferroelectric, its ferroelectric polarization can point along any one of the eight degenerate [111] directions. This degeneracy permits the posible formation of 3 types of domain walls which are classified by the angle by which the polarization rotates when traveling from one domain to the next (i.e. 71^o, 109^o and 180^o). The domain walls are illustrated in Figure 2.2.

In the $BiFeO_3$ system, the type of domain wall present can determined by mapping the directions of the polarization in all of the domains. To determine the local polarization direction, a scanning probe microscopy technique known as piezoresponse force microscopy (PFM) is employed. The PFM technique is briefly reviewed in Appendix B. The the local polarization vector and domain structure of $BiFeO_3$ films grown on $SrTiO_3$ substrates are shown in Figures 2.3 (a) and (b). The films come in two different flavors, those being 4-variant striped (Figures 2.3 (a)) and mosaic (Figures 2.3 (b)) $BiFeO_3$. The flavor of the $BiFeO_3$ film is determined by the kinetics of the growth. The mosaic samples are more chaotic than the 4-variant films and hence require higher growth rates than the 4-variant films. Figures 2.3 (c) and (d) trace out the the various domain walls present in the 4-variant striped and mosaic films. [105] It was found that the 4-variant films are primarily composed of 71^o domain walls while the domain walls in mosaic samples are largely 109^o (Figures 2.3 (c) and (d)).

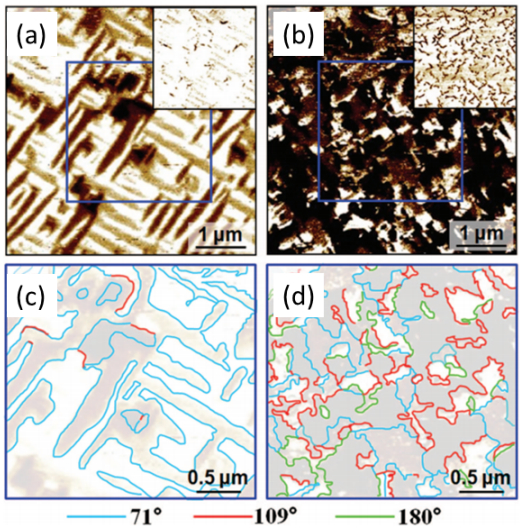

Figure 2.3: (a and b) In-plane and out-of-plane (insets) PFM images of a (a) 4-variant striped and (b) a mosaic $BiFeO_3$ film grown on (001) oriented $SrTiO_3$. (c and d) maps of the domain walls for the boxed regons in (a) and (b). Blue, red, and green lines trace the 71^o, 109^o, and 180^o domain walls. The 71^o domain walls are heavily present in the film shown in (a) while 109^o domain walls are heavily present in the film shown in (b). Taken from [105].

The question then was, how will each of these domain structures influence and exchange coupled ferromagnetic layer and what is responsible for such a coupling?

2.2 Previous exchange coupling studies

2.2.1 Effect of domain walls

Heterostructures of $Co_{.90}Fe_{.10}$ and $BiFeO_3$ where made with both the 4-variant and mosaic films. Figure 2.4 shows the magnetic hysteresis loops for $Co_{.90}Fe_{.10}$ / $BiFeO_3$ heterostructures with (a) 4-variant and (b) mosaic films plotted with the magnetic hysteresis of $Co_{.90}Fe_{.10}$ deposited on a $SrTiO_3$ substrate as a control. In both cases, the coercive field of the $Co_{.90}Fe_{.10}$ is enhanced when exchange coupled to either $BiFeO_3$ film. The striking difference, however, is the large exchange bias present in the hysteresis loops in the heterostructures with mosaic $BiFeO_3$. In fact, those early researchers even found that the magnititude of the exchange bias is determined by the overall length of the 109^o domain walls present in the mosaic films. [105]

The exchange bias observed with the mosaic films is desired for the electric field control of an exchange coupled magnetization, unfortunately the 109^o domain walls are metastable and are erased when an electric field is applied. While the highly

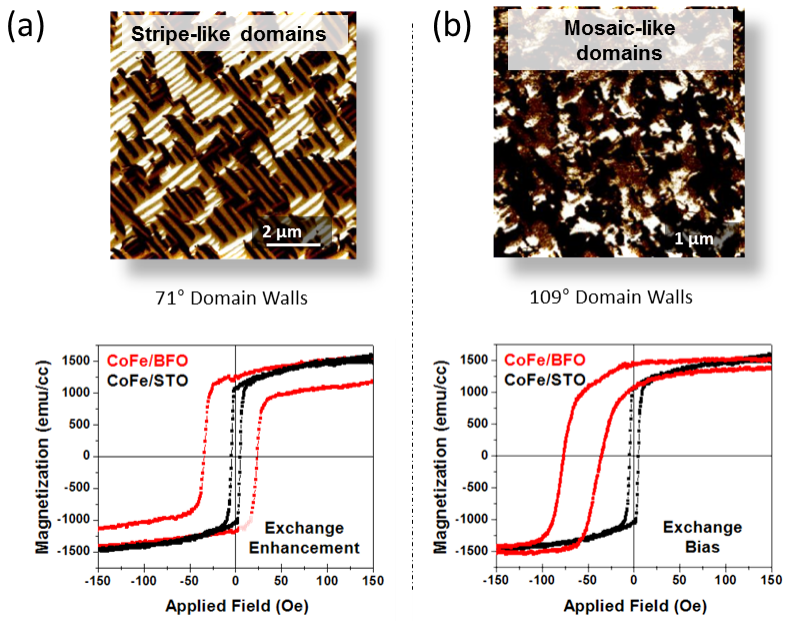

Figure 2.4: (a) In-plane PFM image of a 4-variant $BiFeO_3$ (BFO) film grown on $SrTiO_3$ (STO). 4-variant $BiFeO_3$ (BFO) films grown on $SrTiO_3$ contain primarily 71^o domain walls. The magnetic hysteresis loops from $Co_{.90}Fe_{.10}$ (CoFe) / 4-variant BFO / STO and CoFe / STO heterostructures. (b) In-plane PFM image of a mosaic $BiFeO_3$ (BFO) film grown on $SrTiO_3$ (STO). Mosaic $BiFeO_3$ (BFO) films grown on $SrTiO_3$ contain primarily 109^o domain walls. The magnetic hysteresis loops from $Co_{.90}Fe_{.10}$ (CoFe) / mosaic BFO / STO and CoFe / STO heterostructures.

desirable exchange bias is absent in the 4-variant films, there is still a significant effect from the exchange coupling. The corecive field of the $Co_{.90}Fe_{.10}$ has increased by several times. More importantly, the 71^o domain walls are stable and will not be erased with an applied voltage. This makes the striped 4-variant film the film of choice for the early electric field control of ferromagnetism experiments.

2.3 Towards the electrical control of magnetism

Now that clear evidence for the coupling between $BiFeO_3$ and $Co_{.90}Fe_{.10}$ has been presented, it is a question if whether the magnetic moment of the $Co_{.90}Fe_{.10}$ can be controlled with a voltage applied to the $BiFeO_3$ layer. Before this, the electric field control of $BiFeO_3$'s magnetic order must be demonstrated. This section begins with the investigation of the evolution of $BiFeO_3$'s antiferromagnetic order due to an applied electric field. This section ends with the demonstration of the electrically assisted magnetization reversal and the electric field control of magnetism using two fundamentally different ferromagnet-$BiFeO_3$ heterostructures. The fundamentals are discussed in terms of the symmetries broken by the mechanism that couples the ferromagnets magnetic order to $BiFeO_3$.

2.3.1 Electrical control of antiferromagnetism

The first experimental evidence of the electrical field induced evolution of the antiferromagnetic ordering in the $BiFeO_3$ thin films employed a combination of PFM and photoemission electron microscopy techniques (PEEM). [53] Figure 2.5 shows the primary discoveries of the work. The correlation between the ferroelectric domain structure and the antiferromagnetic domain structure is evident by the the X-ray magnetic linear dichroism (XMLD) PEEM (Figure 2.5(a)) and in-plane PFM (Figure 2.5(c)) images. The two images are taken a the same location on the sample. A close look at the images shows that the domain structure is the same for the two orders.

The region of the sample enclosed by the yellow boxes is where the voltage was applied. Figures 2.5(b) and (d) show modified domain orders in both the PEEM and PFM images. By looking at very specific regions (labeled 1-4) in the figure, the type of ferroelectric switch undergone at that location can be determined. Locations 1 and 2 underwent a 109^o ferroelectric switch while regions 3 and 4 underwent 71^o and 180^o ferroelectric switching events. A clear change in the antiferromagnetic axis direction is presented in the regions that underwent a 109^o ferroelectric switch, while no change was observed for the regions of 71^o and 180^o switching. Illustrations of the polarization and magnetic plane are shown for the 71^o and 109^o rotations of the polarization in $BiFeO_3$ unit cells are shown in Figure 2.5. A 180^o rotation does not change the magnetic plane, and hence does not change the antiferromagnetism. The 109^o switch rotates the (001) projection of the magnetic plane while the 71^o switch

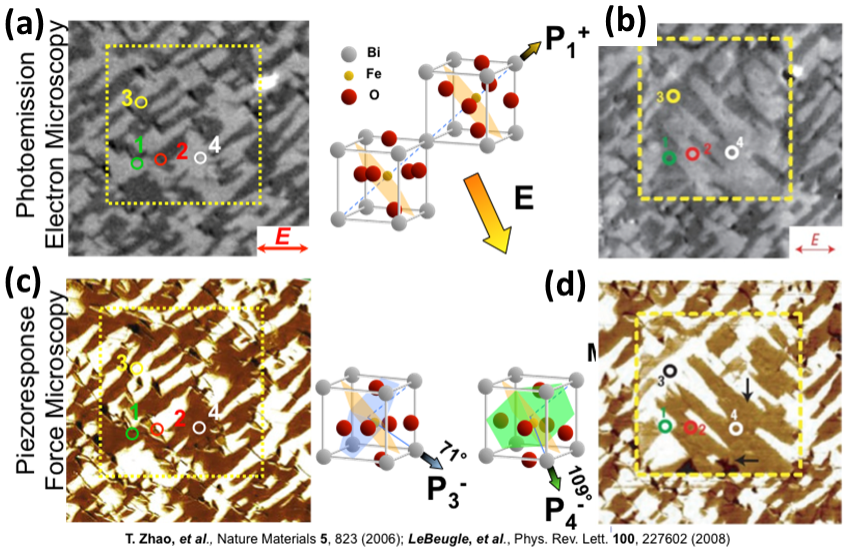

Figure 2.5: (a and b) XMLD PEEM images before (a) and after (b) poling of the same region. The red arrows in the white inset show the X-ray polarization direction during the measurements. (c and d) In-plane PFM images before (c) and after (d) poling of the same region. The arrows show the direction of the in-plane component of ferroelectric polarization. Regions 1 and 2 (marked with green and red circles) correspond to 109^o ferroelectric switching, whereas 3 (black and yellow circles) and 4 (white circles) correspond to 71^o and 180^o switching. In regions 1 and 2 the PEEM contrast reverses after electrical poling. Taken from [53]

leaves the projection invariant.

This demonstration of the ability to electrically control the magnetic order in $BiFeO_3$ thin films suggests that the electrical control of a coupled ferromagnet is possible. Since in a ferromagnet-$BiFeO_3$ heterostructure, where the coupling is driven by exchange between the two magnetic systems, the electrical field control of the magnetic order of $BiFeO_3$ suggests that the exchange coupling in a ferromagnet-$BiFeO_3$ heterostructure can be altered with an applied electric field. Altering the exchange coupling across the interface is expected to lead to a change in the magnetic order (magnetization rotation or change in anisotropy) of the ferromagnetic layer. The remainder of this chapter covers the early works that investigated this possibility.

2.3.2 Electrical control of local ferromagnetism

In this section two early and fundamentally different approaches to the electric field control of magnetism will be highlighted. The first mechanism employs the interface magnetic exchange coupling between $BiFeO_3$ and ferromagnetic $Co_{.90}Fe_{.10}$.

The second mechanism illustrated is mediated by strain. The fundamental difference between these two mechanisms arises from the underlying symmetry broken. The interface exchange coupling has the potential to break time reversal symmetry and it is often modeled as an ficticious magnetic field. The lattice/strain coupling preserves the time reversal symmetry and thus no deterministic reversal of a magnetization is possible.

Exchange coupling driven

The observation of the electric field control of the antiferromagnetism in $BiFeO_3$ thin films set the stage for the electric field control of a ferromagnetic layer exchange coupled to the $BiFeO_3$ film. A single-phase multiferroic composite, consisting of $Co_{.90}Fe_{.10}$ and multiferroic magnetoelectric $BiFeO_3$, was then created in order to probe the ability to electrically control the ferromagnetic state.

In order to probe the ability to electrically control the ferromagnetic state of the $Co_{.90}Fe_{.10}$ layer, simple device structures were designed to ensure the proper ferroelectric switch to enable a magnetic change (i.e. a rotation of the magnetic plane). Additionally, the structures were scaled down to illustrate local functionality and reduced switching voltages. The device shown in Figures 2.6(a-b) illustrates the device layout and how the electric field is applied in the plane of the $BiFeO_3$ film (red in the figure). [54] The lateral distance between the $SrRuO_3$ poling electrodes (blue) is 6 microns and in between the poling electrodes, but on top of the $BiFeO_3$ film, resides a small $Co_{.90}Fe_{.10}$ dot that is capped with a thin Pt layer to prevent oxidation of the $Co_{.90}Fe_{.10}$. The idea behind this device is to then apply an in-plane electric field to the $BiFeO_3$ layer which is below the $Co_{.90}Fe_{.10}$ dot (see Figure 2.6(b)) that reorients the $BiFeO_3$ domain structure.

The devices were created by first growing a thin layer ($\sim$50nm) of $SrRuO_3$ on a $SrTiO_3$ substrate by pulsed laser deposition (PLD). Following this growth, optical lithography is used to define the poling electrodes. The unwanted $SrRuO_3$ is removed using an Ar ion mill, exposing the underlying $SrRuO_3$ substrate and leaving only the $SrRuO_3$ electrodes. After this step, the sample is covered with a blanket $BiFeO_3$ layer of roughly 150nm. Following the growth the $BiFeO_3$, the films are characterized within the regions of interest (i.e. the region between poling electrodes). Figures 2.6(c-e) show in-plane PFM images of the $BiFeO_3$ domain structure in the region between the two $SrRuO_3$ poling electrodes. No $Co_{.90}Fe_{.10}$ is present in these images. The striped like ferroelectric domain structure is observed in between the poling electrodes. The polarization and orientation of the ferroelectric domain walls were intentionally oriented at a 45 degree angle with respect to the direction of the applied electric field (i.e. normal to the $SrRuO_3$ poling electrodes) to induce 71^o in-plane switching events at each domain and an overall 90^o rotation of the in-plane component of the macroscopic polarization. The regions of interest are exposed to cycling voltage pulses to cycle the $BiFeO_3$ domain structure to ensure the expected switching event. After

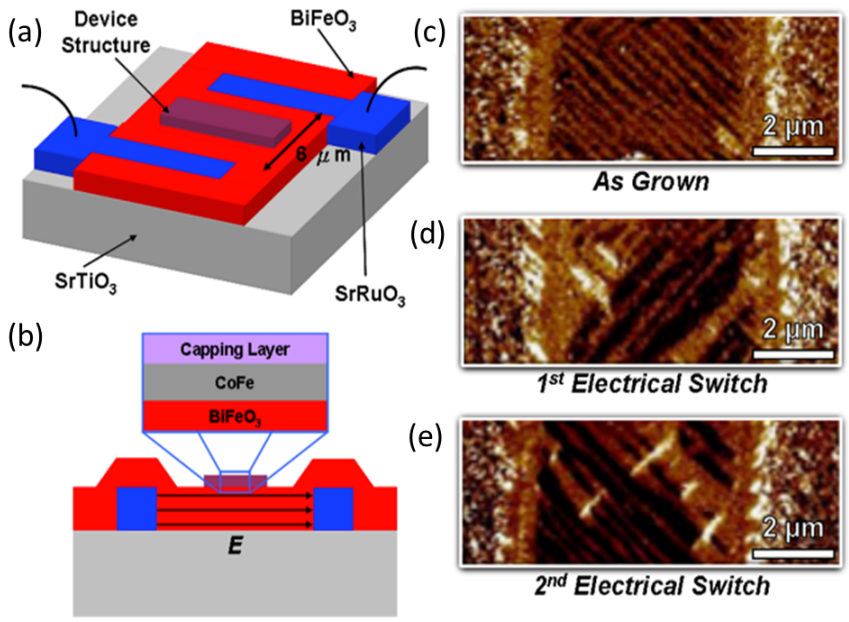

Figure 2.6: (a and b) Schematics of the device structure used in [55]. The schematic shows the $SrRuO_3$ electrodes in blue which are separated by 6 μm and buried under a $BiFeO_3$ film (Red). On top of the $BiFeO_3$ and inbetween the $SrRuO_3$ electrodes is a $Co_{.90}Fe_{.10}$ / Pt dot. The electric field is applied in the plane of the $BiFeO_3$ film and under the $Co_{.90}Fe_{.10}$ / Pt dot. (c -e) are PFM images of the $BiFeO_3$ surface at the device structure before the $Co_{.90}Fe_{.10}$ / Pt dot is deposited. The structure is imaged in the (c) as-grown state and after the (d) first and (e) second electrical switches. Taken from [54].

each voltage pulse, the remnant ferroelectric domain structure within the swicthing region is imaged with PFM. One complete switching cycle is shown in Figures 2.6(c-e). Following the characterization of the $BiFeO_3$ film, the samples have the $Co_{.90}Fe_{.10}$ / Pt dots deposited on top the $BiFeO_3$ film. [54]

Chu *et al.* first probed the magnetization and domain state of the $Co_{.90}Fe_{.10}$ / Pt dot. The magnetic state of the $Co_{.90}Fe_{.10}$ feature in the as-grown remant state is imaged using XMCD-PEEM at the Co L3 edge (Figure 2.7(a)) and a schematic of the observed magnetic domain structure is given in Figure 2.7(d). The $Co_{.90}Fe_{.10}$ has two domain variants (grey and black regions in schematic and image; the corresponding arrows give the direction of the associated magnetization) with a net magnetization (blue arrow) and a domain structure which are oriented at 45^o angles with respect to the $SrRuO_3$ electrodes. These two facts are in agreement with the $BiFeO_3$ domain structure shown in Figure 2.6(c).

To detect the electric field control of these small $Co_{.90}Fe_{.10}$ dots, XMCD PEEM

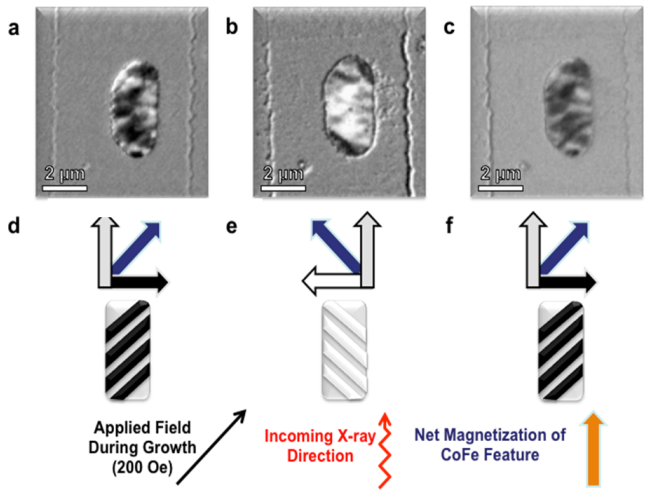

Figure 2.7: (a - c) XMCD-PEEM images of the $Co_{.90}Fe_{.10}$ / Pt dot when the device is in the (a) as-grown state, (b) after the first switch, and (c) after the second switch. (d - f) schematics illustrating the XMCD contrast, domain structure, and net magnetization direction (blue arrows) for each of the states shown in (a - c). Taken from [54].

images are taken after poling of the $BiFeO_3$ layer. The resulting magnetic domain structure and magnetization directions after one voltage pulse is imaged Figure 2.7(b) and schematically depicted in Figure 2.7(e). The color of the XMCD-PEEM contrast has changed with respect to the as-grown image (Figure 2.7(a)) and the orientation of the magnetic domain structure has rotated by 90^o. This is schematically illustrated in Figure 2.7(e). The reorientation of the mangetic domains by 90^o correlates with the observation where the $BiFeO_3$ domain structure and net in-plane polarization rotate by 90^o after the first switch (Figure 2.6(d)).

Furthermore, it was shown that this 90^o reorientation of the magnetic domain structure is reversible, just as the 90^o rotation of the $BiFeO_3$ domain structure and net in-plane polarization are reversibily switched with the voltage. Figures 2.7(c) and (f) show the XMCD PEEM image and the illustration of the XMCD PEEM data. Again the XMCD PEEM contrast has changed from the first switch. The domain structure and the net magnetization have reverted back to the direction that was observed in the as-grown state illustrating the reversible nature of the switch and the correlation to the multiferroic domain structure.

Lattice/strain driven

Another mechanism for the electric field control of magnetism is one that is driven by strain. This mechanism differs fundamentally from the exchange coupling mechanism in that strain does not break time reversal symmetry, and thus no deterministic

magnetization reversal is possible with soley an applied electric field. The pioneering work by Zavaliche *et al.* demonstrates this very clearly. [106] In this work a nanostructured system of $CoFe_2O_4$ / $BiFeO_3$ where nanosized pillars are embedded into a $BiFeO_3$ matrix. The $CoFe_2O_4$ is a magnetostrictive material with a negative magnetostriction coefficient, in that an applied tensile stress along the length of the pillar will drive the magnetization to the plane perpendicular to the length of the pillar. When such a stress is removed, the magnetization has a 50% probability of returning to the upward state along the pillar length and a 50% probability of returning to the downward state along the pillar length. A compressive stress keeps the magnetization along the pillar length. These latter points are schematically illustrated in Figures 2.8 (a - d), with the applied stress being driven by the piezoelectric distortion of the $BiFeO_3$ matrix in response to an applied electric field.

Time reversal symmetry can be broken with the application of a magnetic field (see Figure 1.1 for a discussion). To illustrate the necessity of time reversal symmetry breaking, an electric field was applied to the $CoFe_2O_4$ / $BiFeO_3$ heterostructure using a PFM tip while under (Figures 2.8(f) and (g)) H = 0 and H = 700 Oe (Figures 2.8(h) and (i)). When the voltage was applied, under zero magnetic field, to a $CoFe_2O_4$ / $BiFeO_3$ heterostructure that was magnetically saturated in the upward direction (see before and after boxed regions in Figures 2.8(f) and (g)) some of the moments reorient into a downward direction while others remain unchanged. Figure 2.8(g) shows a roughly even mix of up and down states. [106]

The switching was then performed on the heterostructure when it was initially magnetically saturated in the downward direction while under an applied field of 700 Oe, which is much smaller than the coercive field. A comparision of Figures 2.8(h) and (i) reveal that more than 80% of the switched region has reversed its magnetization direction. This clearly illustrates the need for time reversal symmetry breaking for deterministically reversing a magnetization.

2.3.3 Concluding remarks and summary of the issues

Chu *et al.* demonstrated the electrically induced magnetization rotation in rather large devices (μm scale). [54] Large voltages of 200V were applied to see this effect, and the net magnetization rotated by 90 degrees. While a 90^o rotation of the magnetization can be quite desirable for nanomagnetic logic and electrically controlled magnetic sensors. A 180^o degree rotation of the magnetization, however, is what is valued from the perspective of magnetic memories. In memory, a trilayer is used to form the bit and the resistance of the device is given by $R = R_0 - \Delta R\cos(\theta)$. Where θ is the angle between the magnetizations of two magnetic layers. Thus a 180^o separation gives the maximum change in resistance between the two states (parallel magnetizations and antiparallel magnetizations). We have discussed the need to break time reversal symmetry in order to reverse a magnetization (i.e. a 180^o rotation), now the question is: Can we electrically reverse the magnetization?. Additionally, can we

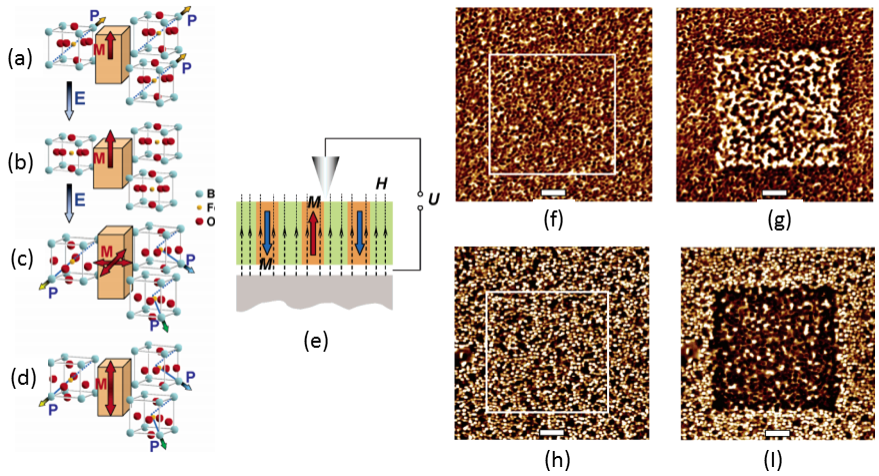

Figure 2.8: (a - d) Schematics of the electric field control of magnetism in the $CoFe_2O_4$ / $BiFeO_3$ heterostructure. (a) The initial state of the system. The polarization of $BiFeO_3$ and the magnetization of the $CoFe_2O_4$ are indicated. (b) increased perpendicular magnetic anisotropy due to the compressive stress following the spontaneous distortion in the $BiFeO_3$ matrix when the polarization is switching due to an electric field, (c) fourfold in-plane magnetic anisotropy induced by the tensile piezoelectric deformation in the matrix when the polarization and the applied electric field are parallel, and (d) final configuration with perpendicular magnetic anisotropy. The magnetization of the $CoFe_2O_4$ can choose either the up or down state because time reversal symmetry is not broken. (e) Experimental configuration for the data presented in (f-i). A magnetic field is applied to break time reversal symmetry as an electric field is applied. MFM images of upward oriented magnetization before (f) and after (g) the application of a voltage under zero magnetic field. MFM images taken of downward oriented magnetization before (h) and after (i) the application of a voltage and an upward oriented magnetic field. Taken from [106].

then integrate this reversal into a prototype magnetoelectric device?

To begin such an endeavor, we should first highlight some of the issues faced in the previous work.

- Mosaic domain structure: very complex domain structure, exchange coupling mechanism unclear
- 4-variant $BiFeO_3$ domain structure: complex domain structure, exchange coupling mechanism unclear
- Magnetization only rotated by 90^o and determined by non-quantitative technique
- High voltages required ($\sim$200V) for switching
- In-plane switching: non-ideal geometry of memories

The multiferroic domain structures (mosaic and 4-variant) are complex and the domains are not well ordered. The high degree of correlations found in the $BiFeO_3$ system make the domains and domain walls possible sources of exchange coupling. This makes an interpretation exchange coupling studies difficult.

Chapter 3

Exchange coupling with ordered $BiFeO_3$ domains

The previous chapter summarized the work and understanding that derived from the early experiments of exchange coupling in $Co_{.90}Fe_{.10}$ / $BiFeO_3$ heterostuctures with 4-variant and mosaic $BiFeO_3$ films. Additionally, the early demonstrations of the electric field control of antiferromagnetism and local ferromagnetism were shown using the 4-variant $BiFeO_3$ films. The work presented in this chapter was intended to build upon and use the information from the previous work to uncover the difference between exchange coupling with a $BiFeO_3$ domain and a $BiFeO_3$ domain wall through the use of a more simplified/ordered $BiFeO_3$ system. As part of the understanding of the exchange coupling with a $BiFeO_3$ domain, the objective is to uncover the directionality of the relevant order parameters (P,L,M) of $BiFeO_3$. Lastly, the work in this chapter was searching for an eligible pathway to an electric field induced magnetization reversal. Indeed, a possible pathway emerged.

3.0.4 $BiFeO_3$ domains, domain walls and domain wall ordering

In order to study the properties of domain walls, it is imperative that their formation be controlled. Furthermore, the effect of the multiferoic domains and domain walls can be determined if the domain walls can be ordered. Controlled arrays of 71^o domain walls in $BiFeO_3$ thin films can created. This is achieved through the control over the growth and elastic boundary conditions in $BiFeO_3$ / $SrRuO_3$ / $DyScO_3$ (110) heterostructures. [107] The $DyScO_3$ (110) provides a small anisotropic strain to the $BiFeO_3$. To minimize the in-plane strain, the $BiFeO_3$ orders into a quasi-periodic, striped array of domains/domain walls.

A $BiFeO_3$ film predominantly comprised of 71^o domain walls is described in Figures 3.1(a-d). Figure 3.1(b) is a detailed representation of the polarization directions in each domain in this structure while Figure 3.1(a) illustrates a homogeneity of the

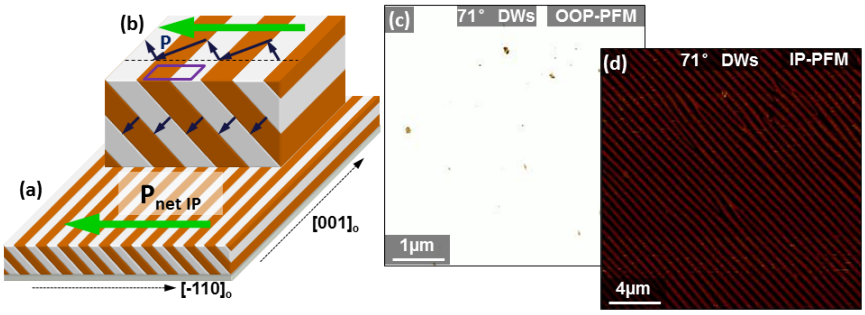

Figure 3.1: (a) Schematic of 71^o domain pattern. Domain colors are following from IP-PFM image as shown in (b). Green arrow shows the net IP ferroelectric polarization. (b) Schematic of detailed 71^o domain structure with blue arrows showing the ferroelectric polarization components in [001]pc and [010]pc planes. (c and d) OP and IP-PFM images of 71^o domain pattern.

macroscopic, net in-plane polarization. The out-of-plane PFM image (Figure 3.1(c)) of such a 71^o domain wall sample shows a uniform contrast, indicating a single out-of-plane polarization component which is directed downward, into the substrate. The in-plane PFM image (Figure 3.1(d)) shows a stripe pattern that is composed of two contrasts, dark (black) and neutral (brown) contrast. The black contrast corresponds to domains with the in-plane component of the polarization directed to the right while the direction for the brown contrast is oriented upwards. The net in-plane polarization, P_{netIP}, points orthogonal to the length of the domain wall and along a [100] direction.

Ferromagnet - antiferromagnet heterostructure with ordered striped 71^o domain walls

Here I will discuss the magnetic properties of a $Co_{.90}Fe_{.10}/BiFeO_3$ heterostructure with the $BiFeO_3$ layer having a simple, quasi-periodic, ferroelectric domain architecture with only two 71^o ferroelectric polarization variants, as in Figure 3.2(a). The sum of these two polarization variants leads to a well-defined in-plane projection of the net polarization (P_{netIP}) which points along [1-10] direction of the $DyScO_3$ substrate (Fig. 3.2(a)).

The striped 71^o $BiFeO_3$ films were immediately inserted into a vacuum sputtering chamber with a base pressure of $\sim$3x10^{-8} Torr. Here, $Co_{.90}Fe_{.10}$ (2-3 nm) layers were grown by DC magnetron sputtering under a 200 Oe magnetic field and capped with Pt (3 nm) to prevent oxidation. To probe the interfacial coupling of the ferromagnet-

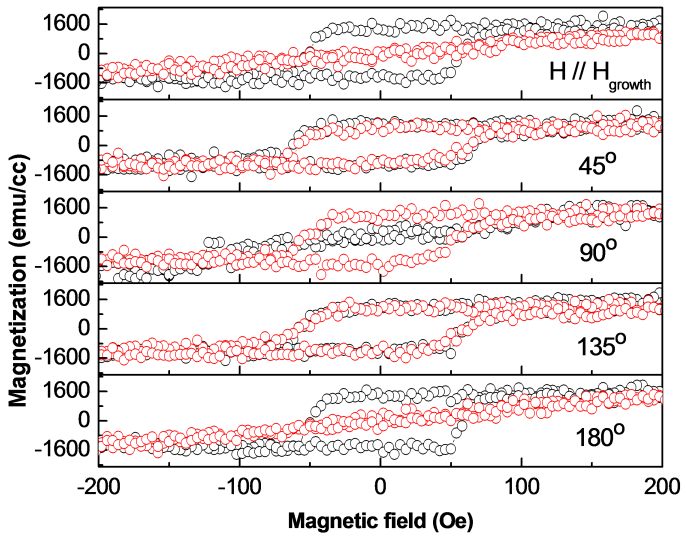

Figure 3.2: M(H) curves measured at room temperature from $Co_{.90}Fe_{.10}/BiFeO_3$ heterostructures where the $Co_{.90}Fe_{.10}$ growth field was applied along (black open circles) or perpendicular (red open circles) to the net in-plane polarization direction (P_{netIP}). The samples were rotated every 45^o in-plane from the growth direction.

multiferroic heterostructure, a 200 Oe magnetic field was applied parallel and perpendicular to (P_{netIP}). Figure 3.2(b) presents the in-plane hysteresis loops, obtained by vibrating sample magnetometry (VSM), taken from samples where the growth field was applied perpendicular (red circles) and parallel (black circles) to (P_{netIP}). The data in Figure 3.2(b) clearly illustrate that irrespective of the orientation of the growth field, the anisotropy is always uniaxial and along the axis corresponding to the direction of (P_{netIP}). This trend is observed regardless of the orientation of the $BiFeO_3$ growth terraces with respect to the ferroelectric domain walls. These heterostructures show an enhancement of the coercive field, when compared to $Co_{.90}Fe_{.10}$ grown on the $DyScO_3$ substrate, and negligible exchange bias anisotropy (See Figure 1.11).

3.1 Determination of coupling mechanism: microscopic origins of coupling with striped 71^o films

The (110) $DyScO_3$ substrate was used to reduce the complexity of the resulting $BiFeO_3$ so that the interface coupling mechanism with an exchange coupled $Co_{.90}Fe_{.10}$ layer could be determined. While the $DyScO_3$ substrate has reduced the number of possible coupling mechanisms, there still remains possible pathways for exchange cou-

pling in this simplified system. Those being: (1) stress induced by the ferrodistortion of the $BiFeO_3$ due to the ferroelectricity, (2) the easy axis of the antiferromagnetic spins (L) in the $BiFeO_3$ domains, (3) the canted moment (M) in each of the $BiFeO_3$ domains, (4) the 71^o domain walls and (5) an oxidized or rough interface. In each of the following subsections, a possible coupling mechanism will be eliminated to reveal the microscopic origin of the exchange coupling in this heterostructure. Additionally, the magnetic order of $BiFeO_3$ will be determined beyond the argument of a (111) easy magnetic plane to the point were the direction of the antiferromagnetic easy axis and the canted moment is determined.

3.1.1 Elimination of stress induced anisotropy by polarization

To test the the possibility of a stress induced anisotropy as a result of the ferroelastic distortion, the insertion of a fully strained, epitaxial $SrTiO_3$ (2 nm) or $SrRuO_3$ (2 nm) spacer between $BiFeO_3$ and $Co_{.90}Fe_{.10}$ was used to break the magnetic interface coupling while preserving the stress from the $BiFeO_3$ film. The insertion of a non-magnetic spacer layer resets the easy axis of the $Co_{.90}Fe_{.10}$ films to the direction of the applied growth field, ruling out magnetostriction and stress induced magnetic annealing as the causes of this preferential anisotropy axis. Figures 3.3(a) and 3.3(b) show data taken from two $Co_{.90}Fe_{.10}$ (2.5 nm)/ $SrTiO_3$ (2 nm)/ $BiFeO_3$ heterostuctures and are plotted with the data presented in Figure 3.2(b) for comparison. The magnetic field applied during the growth was fixed at 200 Oe for all of the curves. For the curves in Figure 3.3(a), the growth field was applied parallel to the net in-plane polarization (P_{netIP}) direction. The growth field was applied perpendicular to the P_{netIP} direction for the curves in Figure 3.3(b). A comparison of the two curves in Figure 3.3(a) reveals that the $Co_{.90}Fe_{.10}$ coercivity is reduced, compared to Figure 3.2(b), with the insertion of a fully strained $SrTiO_3$ layer in between $Co_{.90}Fe_{.10}$ and $BiFeO_3$. Furthermore, a comparison of the curves with the $SrTiO_3$ interlayers in Figures 3.3(a) and 3.3(b) show the easy axis becomes insensitive to the P_{netIP} direction. The observed uniaxial anisotropy imposed by the underlying multiferroic $BiFeO_3$ film indicates a strong interfacial magnetic coupling in this system.

3.1.2 Determination of antiferromagnetic easy axis (L) and canted moment (M) directions

The magnetic order of the $BiFeO_3$ must be determined in order to decouple the magnetic nature of the exchange coupling with a $Co_{.90}Fe_{.10}$ layer. Since canted moments are very difficult to detect with a direct means due to the small size of the moment, typically the antiferromagnetic easy axis is first determined using X-ray magnetic linear dichroism (XMLD)-photoemission electron microscopy (PEEM). Be-

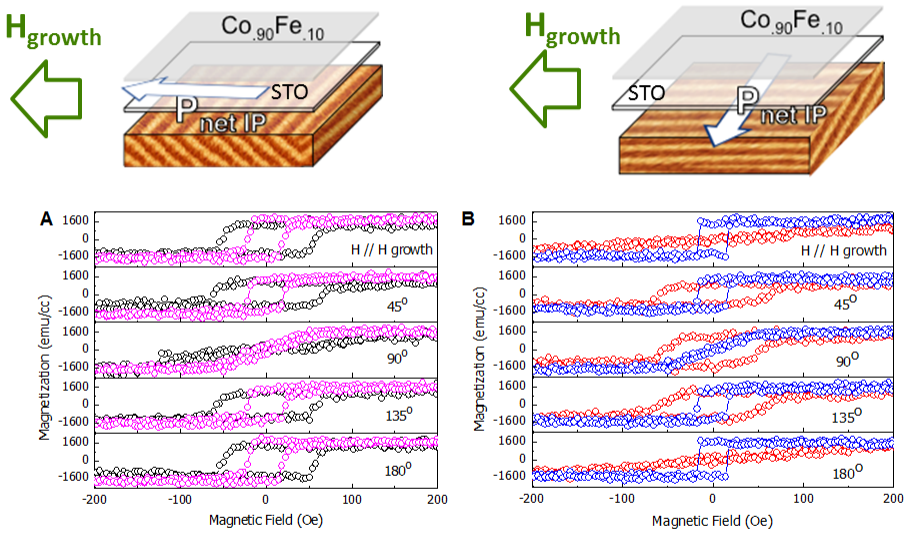

Figure 3.3: (a) (a-b) Magnetic hysteresis curves from the $Co_{.90}Fe_{.10}$ (2.5 nm)/ $BiFeO_3$ heterostuctures from Figure 3.2b (open black and red circles) and a $Co_{.90}Fe_{.10}$ (2.5 nm)/ $SrTiO_3$ (2 nm)/ $BiFeO_3$ heterostuctures (open magenta and blue circles). The 200 Oe growth field was applied parallel to the direction of P_{netIP} for both heterostructures in (a) and perpendicular to P_{netIP} in (b).

ginning with this approach, the XMLD-PEEM of a $BiFeO_3$ film was imaged at the Fe L_2-edge (See Figure 3.4). Figure 3.4(a) shows the XMLD-PEEM image when the X-ray polarization (double-headed green arrow) is oriented along one of the $BiFeO_3$ {110} directions. In the image, the black domains show the contrast, revealing that in the black domains the antiferromagnetic easy axis (L) has a component which is parallel to the X-ray linear polarization. To determine if L has a out-of-plane component the X-ray beam polarization was oriented along the [001] direction. The out-of-plane XMLD-PEEM image is shown in Figure 3.4(b). There is little contrast in this direction revealing that the antiferromagnetic easy axis lies completely in the $BiFeO_3$ (001) plane. Since the $BiFeO_3$ polarization is known to be along the <111> direction and the magnetic order parameters of $BiFeO_3$ are required to lie in the {111} plane in a configuration where the polarization, antiferromagnetic easy axis and the canted moment are mutually orthogonal [51], the precise direction of the antiferromagnetic axis is then determined to be along the [110] type directions. Figure 3.4(c) shows orientation of the antiferromagnetic easy axis in each of the two $BiFeO_3$ domain variants. The polarization points along a <111>, L points along a <110> and thus, the canted moment must point along a $<11\bar{2}>$. This means the (001) projection of these vectors will lead to a configuration where the canted moment and the polarization, in each of the $BiFeO_3$ domain variants, project parallel to each other while the antiferromagnetic easy axis is orthogonal to both. To confirm such a picture, PFM was performed at the same location of the XMLD-PEEM image shown in Figure 3.4(c) to confirm that the in-plane polarization component will be orthogonal to the antiferromagnetic easy axis in each associated domain. Using lithographically defined Pt electrodes to align the images of Figures 3.4(c) (XMLD) and 3.4(d) (PFM), the domain structures in both images can be aligned. Then comparing the direction of the in-plane component of the polarization with the antiferromagnetic easy axis in each domain, it is clearly seen that the two order paramemters are orthogonal on the (001) surface (Compare Figures 3.4(c) and 3.4(d)). The 3-D construction of the order parameters in $BiFeO_3$ and the projections onto the (001)surface are illustrated later in Figure 3.9.

3.1.3 Examination of the $Co_{.90}Fe_{.10}$ / $BiFeO_3$ interface

To probe the sharpness of the $Co_{.90}Fe_{.10}$ / $BiFeO_3$ interface as well as the oxidation state of the $Co_{.90}Fe_{.10}$ at the interface, a combination of transmission electron microscopy (TEM) and electron energy loss spectroscopy (EELS) were employed. Figure 3.5 shows the TEM image of the full Pt/ $Co_{.90}Fe_{.10}$ / $BiFeO_3$ / $DyScO_3$ stack. A high-resolution image of the $Co_{.90}Fe_{.10}$ / $BiFeO_3$ interface is shown in the inset on the left. It is seen in this high resolution image that the $Co_{.90}Fe_{.10}$ is amorphous and the Pt capping layer is nanocrystalline. The $BiFeO_3$ surface is smooth having only a single unit cell step. To more accurately illustrate the sharpness of the interface as well as to probe the oxidation state of the $Co_{.90}Fe_{.10}$ so as to verify CoO was not being

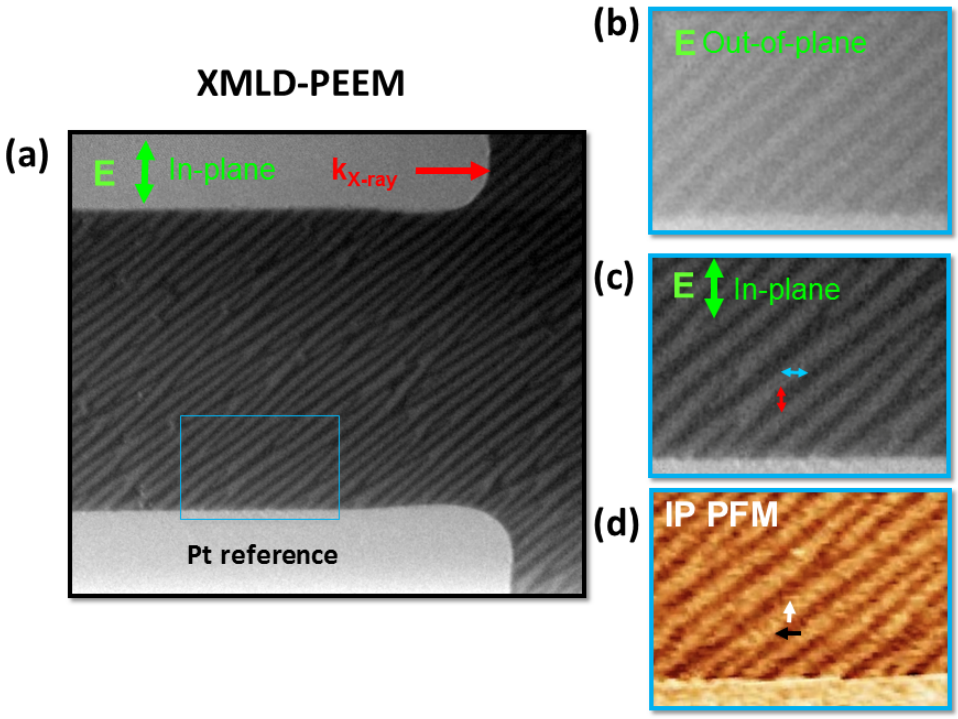

Figure 3.4: (a) XMLD-PEEM image of the $BiFeO_3$ film when the X-ray polarization is oriented along one of the $BiFeO_3$ {110} directions. The direction of the linear polarization of the X-rays are indicated by the double-headed green arrow. The direction of the beam is indicated by the red arrow labeled k. (b) XMLD-PEEM image of the $BiFeO_3$ film when the X-ray polarization is oriented along the $BiFeO_3$ [001] direction. (c) A zoomed in image of (a) near the Pt electrode for later comparision with a in-plane PFM image (d) to correlate order parameter directions in each $BiFeO_3$ domain.

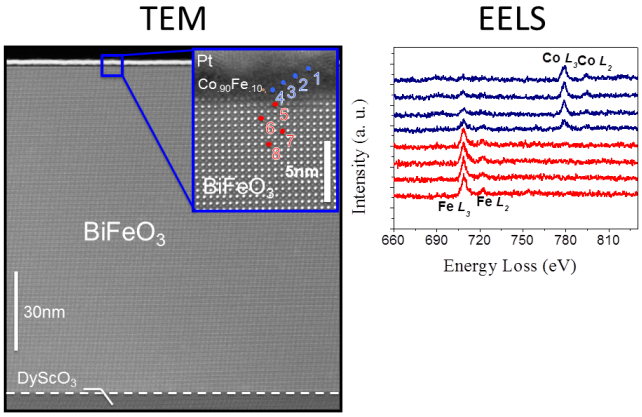

Figure 3.5: Transmission electron microscope (TEM) image of the heterostructure. Inset: High resolution image of the $Co_{.90}Fe_{.10}$ / $BiFeO_3$ interface. Electron energy loss spectroscopy (EELS) curves taken accross the $Co_{.90}Fe_{.10}$ / $BiFeO_3$ interface. EELS curves correspond to the regions labeled 1-8 in the high resolution TEM image.

formed, EELS was performed accross the $Co_{.90}Fe_{.10}$ / $BiFeO_3$ interface and is shown on the left of Figure 3.5. The EELS curves correspond to the regions labeled 1-8 in the high resolution TEM image. Two things become clear in this data set. One is that the inteface is sharp as can be seen by the abrupt enhancement of the Fe L3 peak when going from 4 to 5. Addtionally, the EELS spectra at the Co L3 edge reveal the peak shape for metallic Co rather than insulating CoO, revealing that the Co has not been oxidized in this heterstructure. The combination of TEM and EELS across the $Co_{.90}Fe_{.10}$ / $BiFeO_3$ interface has illustrated that the interesting magnetic exchange interactions in this materials system is not attributable to a extreme roughness or oxidation of Co into the strong antiferromagnet CoO. [81]

3.1.4 Determination of $Co_{.90}Fe_{.10}$ moment direction

The magnetic state of the $Co_{.90}Fe_{.10}$ layer was imaged using X-ray magnetic circular dichroism (XMCD)-photoemission electron microscopy (PEEM) at the Co L3 -edge. The $BiFeO_3$ ferroelectric domain structure was imaged by PFM following the removal of the $Co_{.90}Fe_{.10}$ by ion milling. As shown by the correspondence of the PFM and PEEM images in Figures 3.6(a) and 3.6(b), a clear matching of the magnetic and ferroelectric domain architectures is observed. The growth field for the $Co_{.90}Fe_{.10}$ layer shown in Figure 3.6(b) was oriented along the direction of P_{netIP}. The XMCD Co images were obtained from the ratio between PEEM images taken with right and left polarized X-rays, which results in a 2-D map of projected magnetization of the

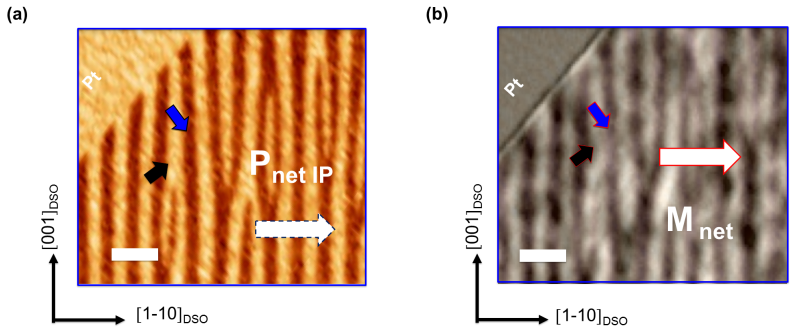

Figure 3.6: (a) In-plane PFM image of $BiFeO_3$. (b) XMCD-PEEM image of the $Co_{.90}Fe_{.10}/BiFeO_3$ heterostructure. The blue and black arrows in (a) correspond to the in-plane projections of the polarizations in each of the ferroelectric domains of $BiFeO_3$. The blue and black arrows in (b) correspond to the directions of the magnetic moments in the white and black domains in the $Co_{.90}Fe_{.10}$ layer, respectively. There is a clear mapping of the domain structures in the images. Scale bars are 500 nm.

ferromagnetic Co domains along the direction of incident X-rays.

Furthermore, XMCD-PEEM images were taken at different orientations of the sample relative to the incoming X-rays to distinguish the orientation of magnetization within each domain. Figure 3.7 shows the in-plane PFM image of a $BiFeO_3$ film and the corresponding XMCD-PEEM images of Co after $Co_{.90}Fe_{.10}$ was deposited on the film. The electrodes were used to create a shared reference frame between the PFM and PEEM images. A comparison of Figures 3.7(a) and 3.7(c) reveals a one-to-one mapping of the magnetic and ferroelectric contrasts. The ferromagnetic Co images in Figures 3.7(b-d) were taken with the incident beam at 45^o (b), 90^o (c) and parallel (d) to P_{netIP}. Figures 3.7(e-h) correspond to the black boxes in Figures 3.7(a-d). The images in Figures 3.7(b) and 3.7(f) exhibit two contrasts corresponding to ferromagnetic domains aligned along the direction of the k vector (white) of the X-ray and at 90^o from the k vector direction (grey). To distinguish the direction of the magnetic domain (labeled 1) in Figures 3.7(b) and 3.7(f), the angle of the X-ray beam with respect to the P_{netIP} direction was increased to 90^o (Figures 3.7(c) and 3.7(g)). The contrast changes to a darker grey indicating the upward-right orientation of the ferromagnetic domains labeled 1 in Figure 3.7(f). The X-ray beam was then oriented parallel to the P_{netIP} direction (Figures 3.7(d) and 3.7(h)). The absence of contrast indicates that both ferromagnetic domains have a component that points to the right in the Figures 3.7(d) and (h).

This rotational dependence reveals that there is a one-to-one domain correlation between the ferroelectric domain structure of $BiFeO_3$ and the magnetic domain structure of the coupled $Co_{.90}Fe_{.10}$ layer. Additionally, a collinear arrangement is observed between the in-plane projection of each polarization variant and the moment from the corresponding $Co_{.90}Fe_{.10}$ domain. The directions of the underlying ferroelectric do-

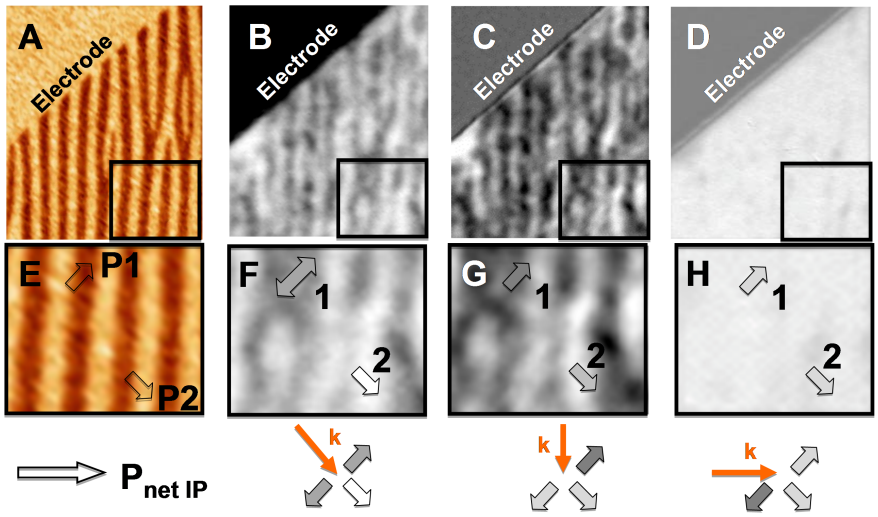

Figure 3.7: (a) In-plane PFM image of the $BiFeO_3$ ferroelectric domain structure. (b-d) XMCD-PEEM images of the $Co_{.90}Fe_{.10}$ domain structure from the same area that is shown in (a). The X-ray is directed at 45^o (b), 90^o (c) and parallel (d) to P_{netIP}. (e-h) A zoom-in of the areas encompassed by the black squares in (a-d). The arrows labeled P1 and P2 in (e) show the in-plane projection of the polarization within each of the domain variants. The arrows labeled 1 and 2 in (f-h) are the directions of the moment at the location of P1 and P2 in (e). The contrast observed in each image is described below each image with the colored arrows and the orange arrow that shows the direction of the incident X-ray.

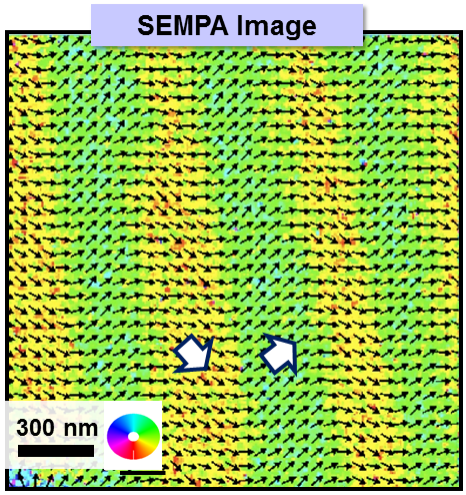

Figure 3.8: SEMPA image of the domain structure of $Co_{.90}Fe_{.10}$ in a $Co_{.90}Fe_{.10}$ / striped 71^o $BiFeO_3$ heterostructure. The color wheel gives the direction of the local moment. Large white arrows show the direction of the macroscopic magnetization in eac of the domain variants. The local moment rotates by 90^o across each domain.

main polarizations and $Co_{.90}Fe_{.10}$ domain magnetizations are given in Figures 3.6(c) and (d) respectively.

To verify the direction of the local moment, a technique with a higher resolution was employed to image the local moment direction. A scanning electron microscope with polarization analysis (SEMPA) can image the local magnetic moment with a resolution of ∼20nm. For an excellent review of the SEMPA technique see references [108, 109]. Figure 3.8 is an image of the magnetic domain structure of the $Co_{.90}Fe_{.10}$ film in a $Co_{.90}Fe_{.10}$ / striped 71^o $BiFeO_3$ heterostructure. The striped domain structure induced by the $BiFeO_3$ is clearly seen. Looking at the moment rotation when moving from one domain to the neighboring domain, the moments rotate such that the macroscopic moment at each domain is paralell to the in-plane component of the polarization in the associated $BiFeO_3$ domain. The large white arrows in Figure 3.8 represent the macroscopic moment in its representative domain.

Lastly I end with end argument that the magnetic interface exchange coupling cannot be due to the 71^o domain walls since the clear one-to-one domain correlation and the collinear arrangement of the $Co_{.90}Fe_{.10}$ moments to the in-plane polarization in each domain implies that the coupling is due to a order parameter in each of the $BiFeO_3$ domains. Since the $Co_{.90}Fe_{.10}$ moments were found to couple collinearly with the in-plane polarization and we have eliminated the polarization, the antiferromagnetic easy axis, the 71^o domain walls and the possibility of roughness or metal oxidation at the interface between $BiFeO_3$ and $Co_{.90}Fe_{.10}$, it is concluded that the $Co_{.90}Fe_{.10}$ moments couple to the canted moment (M_c) in each domain. This agrees

with the observation of the collinear alignement of the in-plane polarization and the $Co_{.90}Fe_{.10}$ moments in each domain and the determination of the direction of the canted moment direction to be along the $<11\overline{2}>$ directions that projects parallel to the polarization onto the (001) plane.

3.1.5 Coupling mechanism and pathway to the electric field control of magnetism

In $BiFeO_3$ bulk, the antiferromagnetic structure is described as a cycloidal G-type. [100, 103, 45] In thin films, a weak canted ferromagnetism emerges from the breaking of this cycloid and is perpendicular to both the ferroelectric polarization and the antiferromagnetic axis. [51] Considering a single unit cell within a single $BiFeO_3$ ferroelectric domain variant with a polarization (P) pointing along a <111> direction, the canted moment (M_c) and the antiferromagnetic axis (L) lie perpendicular to each other in the (111) plane. This is schematically illustrated in Figure 3.9(a). The one-to-one correlation between the direction of the magnetic moments within each ferromagnetic domain and the ferroelectric polarization within each ferroelectric domain observed in Figures 3.6(c) and Figure 3.6(d) leads us to infer that a $BiFeO_3$ canted moment is pointing along the $<11\overline{2}>$ which projects parallel to the polarization on the (001) $BiFeO_3$ surface (Figure 3.9(a)). The collinear correlation of the $Co_{.90}Fe_{.10}$ moments with the projected direction of the canted moment and the orientation of the ferromagnetic domains results in a parallel in-plane arrangement of both P_{netIP} and the net $Co_{.90}Fe_{.10}$ magnetization as shown in Figures 3.6(a) and 3.6(b).

This interfacial coupling between the ferromagnet and $BiFeO_3$, described in Figure 3.9(a), combined with the intrinsic correlation between the ferroelectricity and the antiferromagnetism in the multiferroic film [53], imply that the magnetization of the ferromagnet can be controlled within the realms of ferroelectric switching allowed in $BiFeO_3$. Since the polarization of a single ferroelectric domain in the $BiFeO_3$ system must be along one of the eight possible <111> directions, the polarization can only be switched by 71^o, 109^o or 180^o. [110]

Figure 3.10 represents the ferroelectric switching events possible within a single polarization variant in the $BiFeO_3$ system when an electric field is applied in-plane (along the $BiFeO_3$ [110] and $[\overline{1}10]$ directions) or out-of-plane (along the [001] direction). White arrows give the direction of the polarization pointing along the <111> $BiFeO_3$ directions. The orthogonal (111) magnetic plane, in which the mutually orthogonal antiferromagnetic axis and the weak canted moment lie, is given in yellow. An in-plane 71^o ferroelectric switching event is accompanied with the corresponding rotation of the magnetic (111) plane. Both the ferroelectric polarization and the magnetic plane projections on the (001) plane rotate by 90^o (from the [110] to $[\overline{1}10]$ in the case of the magnetic plane). This rotates the antiferromagnetic axis (which was initially along the [110]). A reorientation of the canted moment (initially along

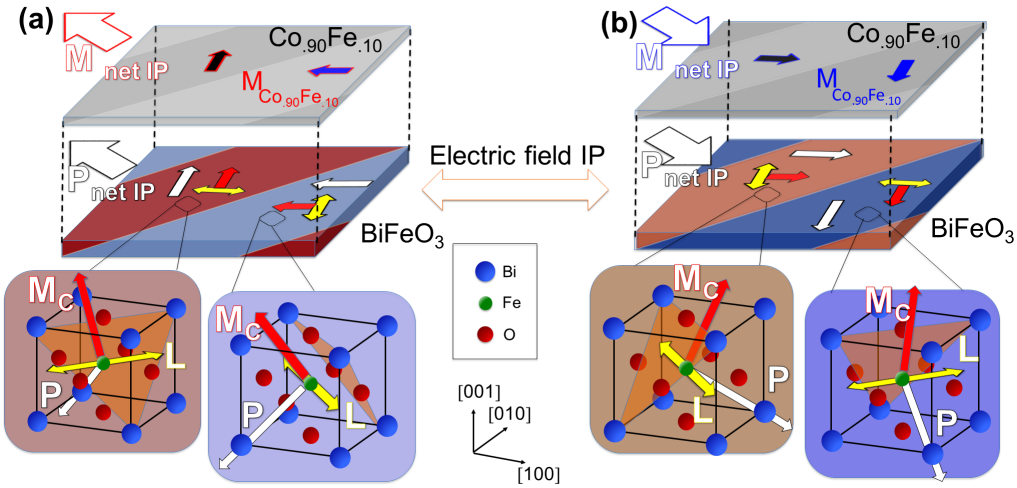

Figure 3.9: (a) Schematic illustrating the magnetic interface coupling and (b) possible configuration after an in-plane electric field is applied. The crystal structures show the orientations of the polarization (white arrows, P), the antiferromagnetic axis (yellow double arrows, L), the canted moment (red arrows, M_c), and the (111) plane (orange) within each of the domain variants in the $BiFeO_3$ system. The $Co_{.90}Fe_{.10}$ moments couple with the in-plane projection of the canted moment within each of the $BiFeO_3$ domains. If the $BiFeO_3$ domain variants individually undergo a 71^o switching event such that P_{netIP} reverses direction, the net magnetization of the $Co_{.90}Fe_{.10}$ layer can be reversed due to the coupling with the canted moment in $BiFeO_3$.

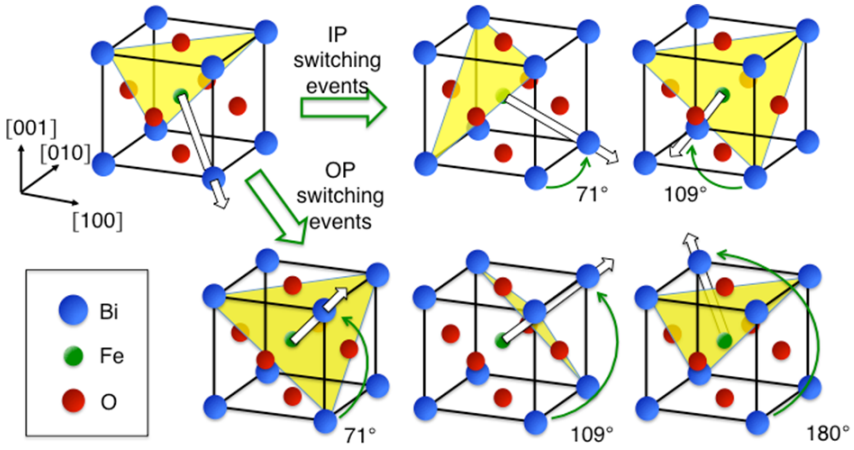

Figure 3.10: Illustrations of the magnetoelectric switching events possible in the $BiFeO_3$ system. The white arrows give the direction of the <111> oriented polarization. The (111) oriented magnetic plane is orthogonal to the polarization and is shown in yellow. An externally applied electric field directed in-plane (along the [110] or the $[\bar{1}10]$) will lead to either a 71^o or 109^o in-plane (IP) switching event. A [001] oriented electric field can permit 71^o, 109^o or a 180^o out-of-plane (OP) switching events. The 180^o switching event leaves the (111) magnetic plane invariant.

the $[1\bar{1}2]$, reorients to the [112]) in $BiFeO_3$ is expected as a consequence of the change in the antiferromagnetic axis orientation. This corresponds to a 90^o change in the projection of the canted moment on the (001) plane. The projected directions of the polarization and the canted moment are collinear in this case. On the other hand, the 109^o in-plane switching event does not change the projection of the antiferromagnetic axis on the (001) plane.

Considering an electric field applied out-of-plane, a reorientation of the (001) projected antiferromagnetic axis only occurs after a 109^o switching event. This projected reorientation is a 90^o rotation that will also affect the direction of the weak ferromagnetic moment. The two other attainable ferroelectric out-of-plane switching events (71^o and 180^o change) do not change the projected direction of the antiferromagnetic order. A 180^o rotation of the polarization leaves the magnetic plane invariant. A summary of the magnetoelectric switching is given in Figure 3.11.

Thus, a in-plane 71^o switch should induce an associated rotation of the in-plane projection of the canted moment. Furthermore, the rotation of the canted moment produces an effective torque on the coupled $Co_{.90}Fe_{.10}$ moments that causes these ferromagnetic moments to rotate with the same sense as the canted moment and P_{netIP} in $BiFeO_3$. Using a striped two-variant $BiFeO_3$ film the combination of each of the polarization variants rotating by 71^o (i.e. 90^o in-plane - one rotates clockwise

Switching event	In-plane rotation of the polarization (P)	In-plane rotation of the antiferromagnetism (L)	In-plane component of canted moment (M_c) expected to rotate?
71° In-plane	90°	90°	Yes
109° In-plane	180°	0°	Unknown
71° Out-of-plane	0°	0°	Unknown
109° Out-of-plane	90°	90°	Yes
180°	180°	0°	No

Figure 3.11: Multiferroic switching events for the in-plane and out-of-plane switching events. The 71^o in-plane and the 109^o out-of-plane switching events are the only switching events that rotate the in-plane components of the polarization (P) and the antiferromagnetism (L). Since the canted moment (M_c) is orthogonal to L, the 90^o in-plane rotation of L imposes the condition such that the canted moment also is expected to rotate in-plane.

while the other rotates counter clockwise), can lead to a unique path of a reversal of P_{netIP} (compare Figures 3.9(a) and 3.9(b)). That is, 90^o rotations of the in-plane projection of the polarization within each domain and summed over adjacent domains leads to a reversal of P_{netIP}. Due to the one-to-one magnetic interface coupling in this heterostructure, a reversal of P_{netIP} in this way implies that a reversal of the in-plane projection of $BiFeO_3$'s magnetic order and the magnetization of the exchange coupled $Co_{.90}Fe_{.10}$ layer is also possible (Figure 3.9(b)). If one can deterministically and reliably switch $BiFeO_3$ in such a way that these two 71^o rotations are preferred, a roadmap to the robust electrical control of magnetism can be created.

3.2 Concluding remarks

In this chapter I have shown that $BiFeO_3$ thin films with well-ordered striped domains with 71^o domain walls can be grown through the control of epitaxial conditions. 71^o domain walls are stable after the application of an electric field. This is the primary reason for the use of the 4-variant films in the previous demonstrations of the electric field control of antiferromagnetism and local ferromagnetism. [53, 54] Heterostructures of $Co_{.90}Fe_{.10}$ and 71^o striped domain $BiFeO_3$ show no exchange bias, but rather an exchange enhancement and uniaxial anisotropy. Even despite the perturbation of the applied magnetic field during the growth of the $Co_{.90}Fe_{.10}$ in these heterostructures, the uniaxial anisotropy follows the axis determined by the direction of $BiFeO_3$'s macroscopic order parameter P_{netIP}. An investigation of the coupling at the microscopic scale reveals a clear one-to-one correlation of striped domains in both subsystems. The moments in the $Co_{.90}Fe_{.10}$ domains were found to follow the in-plane

projection of the polarization in the $BiFeO_3$. Experiments to test the mechanism of the coupling, which required inserting thin layers to break magnetic coupling and imaging the antiferromagnetic axis of $BiFeO_3$ at each $BiFeO_3$ domain, revealed that the local $Co_{.90}Fe_{.10}$ moments couple to the in-plane projection of the $BiFeO_3$ canted moment. Since such a clear coupling exists with the 71^o domain structure, which is stable after the application of an electric field, implies that the electric field control of ferromagnetism is possible in this system. Such a clear coupling also suggests that this system can be used to investigate the magnetoelectric switching characteristics of $BiFeO_3$ and the reorientation of the ferromagnetic moments is governed by the reorientation of the in-plane polarization.

Chapter 4

Electric field control of ferromagnetism: In-plane switching

Current spintronics applications utilize either an externally applied magnetic field or a large current density to achieve a magnetization reversal, which are accompanied by significant energy dissipation. This energy cost could be reduced if the reversal of a magnetization only required the application electric field. In this chapter I will demonstrate a new means of non-volatile, room temperature magnetization reversal using purely electric fields in a ferromagnet-multiferroic system. Using a combination of ferromagnetic and ferroelectric domain imaging techniques, a strong interfacial magnetic coupling, that mediates the reversal, is revealed. Anisotropic magnetoresistance measurements show that this electrically-driven 180^o reorientation of the net magnetization is reversible. This materials configuration opens exciting, new avenues towards next-generation, low-energy consumption spintronics.

4.1 Introduction

In the push for low-energy consumption memory and logic applications, the field of spintronics has focused on establishing control of a magnetization without the need of a magnetic field. [111, 112, 113, 114, 115] Of these, a magnetization reversal requires the injection or the accumulation of spin-polarized carriers to create an effective spin-orbit field, transfer of angular momentum to the macroscopic spin state [3, 116, 4] or to establish a large chemical potential gradient through non-local diffusion. [117] While these methods are effective, large current densities are required and a significant energy loss results from Joule heating. Promising alternatives and a rich field of physics now reside in the use of correlated systems such as multiferroic magnetoelectrics. [118, 119] In these materials an electric field can be applied to the multiferroic to alter its magnetic order. [120, 121, 122] To support both ferroelectric and magnetic orders, multiferroics are typically insulators with an antiferromagnetic

spin arrangement. [43, 46] Hence, multiferroics are used in ferromagnet-multiferroic heterostructures to establish the conductivity and spin polarization necessary for spintronics applications.

Most of the existing work has focused on modulating the exchange bias that is often observed in these heterostructures. For example, electrical reversal of exchange bias and magnetization has been reported in multiferroic magnetoelectric $LuMnO_3$ and $YMnO_3$-based structures at low temperatures where the pinning moments in clamped antiferromagnetic domain walls are unclamped by the electric field and later re-clamped under a magnetic field near the coercive field of the ferromagnet. [123, 124] At room temperature, a magnetoelectric switching of exchange bias was observed in $Pt(Pd)/Co/Cr_2O_3$ heterostructures. [125, 126] However the use of such a non-multiferroic magnetoelectric requires a combination of electric and magnetic fields for the isothermal change in the sign of the exchange bias field. Magnetoelectric multiferroic $BiFeO_3$-based heterostructures have been utilized to demonstrate a strong correlation between its antiferromagnetic-ferroelectric orders and the magnetization (in addition to the exchange bias field) of a coupled ferromagnetic layer that can be modified electrically. [127, 54, 102]

Despite these advances, a 180^o reversal of a magnetization state by applying solely an electric field is yet to be achieved in any material system. Such a reversal is, of course, the underpinning physics behind a broad range of magnetic devices. In the following, I will show the anisotropic magnetoresistance (AMR) of a $Co_{.90}Fe_{.10}$ layer in intimate contact with the room temperature magnetoelectric multiferroic $BiFeO_3$. The reversible and deterministic reversal of the ferromagnet's magnetization through the application of an electric field to the $Co_{.90}Fe_{.10}$ / $BiFeO_3$ heterostructure, under zero magnetic field, is demonstrated at room temperature and is quantitatively determined by AMR measurements.

4.2 Experimental Methods

The $BiFeO_3$ (001) thin films (70-120 nm thick) used for this study were fabricated by pulsed laser deposition (PLD) using a KrF laser on single-crystalline (110) $DyScO_3$ substrates. [107] For PLD, a substrate temperature of 700 ^{o}C was used in an oxygen pressure of 100 mTorr, at a repetition rate of 8 Hz with a laser fluence of 1.1 J/cm^2. After growth, the samples were cooled to room temperature in an O^2 pressure of 750 Torr. The topography and ferroelectric domain architecture of the $BiFeO_3$ films were probed using a combination of atomic force microscopy (AFM) and piezoresponse force microscopy (PFM). The anisotropic strain from $DyScO_3$ substrates results in the formation of a simple, quasi-periodic, ferroelectric domain architecture with only two 71^o ferroelectric polarization variants. The sum of these two polarization variants leads to a well-defined in-plane projection of the net polarization (P_{netIP}) which points along the $[1\bar{1}0]$ direction of the $DyScO_3$ substrate (Figure 3.2(a)). The magnetic

coupling is then confirmed by VSM magnetometry. To probe the evolution of the magnetization after the application of an electric field, a device was designed to enable such a measurement.

4.3 Device design and characterization

4.3.1 Design considerations

The device architecture shown in Figure 4.1 was designed for angle-dependent anisotropic magnetoresistance (AMR) measurements, used to probe the magnetic state of the $Co_{.90}Fe_{.10}$ dots as a function of applied electric field to the $BiFeO_3$ layer. Two outer electrodes on the surface of $BiFeO_3$ are dedicated to the in-plane ferroelectric switching of $BiFeO_3$. Two leads make contact to a 2x4 μm^2 $Co_{.90}Fe_{.10}$ dot positioned at the center of the gap, in-between the poling electrodes. The direction of the applied current was oriented at a 45^o angle to the P_{netIP} which coincides with the macroscopic easy axis of the $Co_{.90}Fe_{.10}$. A 45^o angle was specifically chosen for two reasons. The first is that the sensitivity of the AMR measurement is maximized in this geometry. The second reason stems from simulations of the AMR as a function of the reorientation of the magnetization. Since the reorientation of the magnetization after an applied electric field to the $BiFeO_3$ must be quantified, the AMR measurement must be sensitive to any such reorientation. A quick look at the AMR equation suggests that an arbitrary reorientation of the magnetization with respect to the current (i.e. a arbitrary change in θ) should not be quantifiable due to the 180^o periodicity of the $\cos^2\theta$. To determine if any reorientation of the magnetization can be detected, simulations of the AMR resistance were performed using a Stoner-Wolfarth model under the condition that the applied magnetic field was well below the magnetic switching field as to prevent magnetization switching from the applied field.

Figure 4.2 shows simulations of AMR curves for different orientations (90^o and 180^o) of the magnetic easy axis with respect to a reference orientation which is oriented at a 45^o from the applied current. An applied magnetic field (H_a)that is much smaller than the magnetic anisotropy field (H_u) was used to generate a torque on the magnetization. This ensures that the magnet cannot be switched by the applied magnetic field during the AMR measurement, rather the magnetization wiggles about its magnetic easy axis. The energy landscape is given by the Stoner-Wolfarth model which consists of two terms since no exchange bias anisotropy has been observed in this system (see Figure 4.2). [105, 128] The first term is the Zeeman energy which causes the preferential alignement of the applied magnetic field (H_a) and the magnetization (M). The second term is a uniaxial magnetic anisotropy term whos strength is governed by the uniaxial anisotropy field (H_u). The energy is minimized with respect to the angle of the magnetization to determine θ. Beginning with the

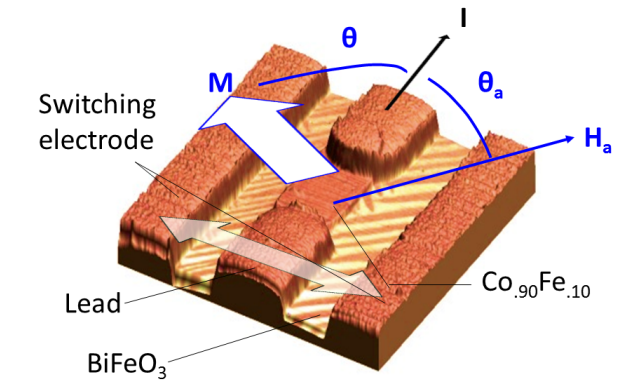

AMR $\rho = \rho_\perp + (\rho_\parallel - \rho_\perp)cos^2\theta$

Figure 4.1: Image of the device to probe the magnetization of $Co_{.90}Fe_{.10}$ dot using AMR after in-plane electrical poling of the $BiFeO_3$. The definition of AMR is given in the equation and the definition of the angles of the magnetization and applied magnetic field during the AMR measurement are defined in the device image.

uniaxial anisotropy at a 45^o from the applied current, that is $\theta_u = 45^o$, as our reference state, we see that the low field AMR is not 180^o periodic but more akin to a 360^o periodic curve (see black curve in Figure 4.2). Now if we rotate the anisotropy axis by 90^o from the reference direction (blue curve) the curve is nearly 90^o out of phase with the reference AMR curve and maintains the 360^o periodic nature. Finally, as the magnetization starts 180^o from the reference direction the simulation predicts a AMR curve (red curve) that is 180^o out of phase with the reference AMR curve and, again, preserves the 360^o periodic nature. In fact, the angle of rotation of the magnetization reflects as a phase shift of the low field AMR curve with respect to the reference direction. Thus in this device configuration, any angle of magnetization rotation after the applied electric field can be detected as long as the direction of the magnetization of the reference state is known. In the case of the $Co_{.90}Fe_{.10}$ / $BiFeO_3$ system, the reference direction can be determined by knowing the direction of P_{netIP} and applying a growth field, during the $Co_{.90}Fe_{.10}$ deposition, along this axis to set the direction.

4.3.2 Device characterization

Device characterization was performed to verify the proper functionality of the device as well as to verify the predictions of the Stoner-Wolfarth simulations of the AMR. Figure 4.3 shows the device characterization verifying the AMR response and the response to a reorientation of the $Co_{.90}Fe_{.10}$ magnetization by 180^o. In Figure

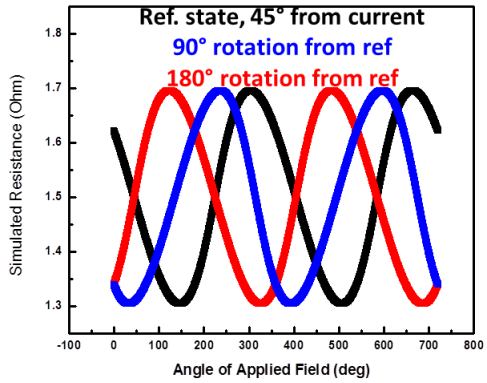

AMR $\rho = \rho_{\perp} + (\rho_{\parallel} - \rho_{\perp})cos^2\theta$

Stoner-Wolfarth

$$E = -MH_a \cos(\theta_a - \theta) + (MH_u / 2)\sin^2(\theta_u - \theta)$$

Figure 4.2: Simulations of AMR curves for different orientations (0^o, 90^o, and 180^o) of the magnetic easy axis with respect to a reference orientation which is oriented at a 45^o from the applied current using an applied magnetic field (H_a)that is much smaller than the magnetic anisotropy field (H_u). This ensures that the magnet cannot be switched by the applied magnetic field during the AMR measurement, rather the magnetization wiggles about its magnetic easy axis. Also shown is the equation of the AMR behavior and the energy landscape which is given by the Stoner-Wolfarth model.

4.3(a) high field (500 Oe, black open triangles) and low field (20 Oe, blue open squares) AMR curves of the device are shown. At 500 Oe the Zeeman energy dominates the energy landscape and thus $\theta = \theta_a$ (angle of the applied field w.r.t. the applied current direction). Thus if $\theta = \theta_a$ then the high field AMR curve should follow a $\cos^2\theta_a$ dependence, which is observed by the 180^o periodicity and the large amplitude of the resistance oscillations. At low field the Zeeman energy is significantly smaller than the anisotropy energy and the result is that the magnetization simply wiggles about its anisotropy axis without switching. At small applied magnetic field the approximation can be made that θ_u - θ is small and therefore the uniaxial anisotropy term can be rewritten in the form of a unidirectional anisotropy (See Appendix B). This can easily be rationalized with the following argument. At low magnetic field, where the magnetization cannot be reversed by the small field due to the larger uniaxial barrier, the magnetization is essentially pinned to one direction, emulating an exchange bias anisotropy. This fact is what causes the change in the AMR phase at low field (refer to appendix B for illustrative derivations and schematics) and has been measured in other metal-oxide exchange bias systems. [129, 123]

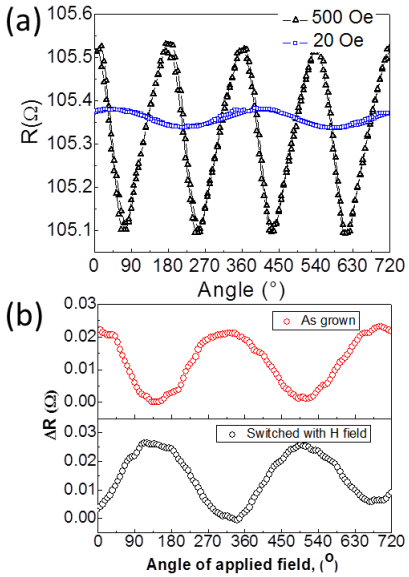

Figure 4.3: (a) Experimental high field (500 Oe, black open triangles) and low field (20 Oe, blue open squares) AMR curves of the device.(b) Low field (20 Oe) AMR curves in the as-grown state (red open circles) and after switching the $Co_{.90}Fe_{.10}$ magnetization state by 180^o using an applied magnetic field (black open circles).

To verify the validity of the predictions made by the Stoner-Wolfarth simulations of the device resistance after the magnetization has been reoriented, the AMR was measured at 20 Oe in the as-grown state, which serves as the reference state (red open circles in Figure 4.3(b)). After the as-grown measurement, the magnetic field was set to -3000 Oe to reverse the magnetization direction, and then reset to 20 Oe to perform the AMR measurement. The resulting AMR curve is plotted in the open black circles in Figure 4.3(b). Comparing the as-grown and magnetically switched AMR curves shown in Figure 4.3(b), it is clearly seen that there is a 180^o phase difference between the two curves. Since the magnetization was reversed (180^o rotation) from the as-grown state, the 180^o phase difference in the AMR curves confirms the predictions made by the Stoner-wolfarth model of the resistance. Thus we conclude that this device is capable of measuring any reorientation of the net magnetization of the $Co_{.90}Fe_{.10}$ after an electric field has been applied to the multiferroic $BiFeO_3$ layer.

4.3.3 Electrical switching of $BiFeO_3$ under the $Co_{.90}Fe_{.10}$ dot

In this AMR structure, after each electric field pulse applied to the $BiFeO_3$, the $Co_{.90}Fe_{.10}$ dot was removed by Ar ion milling to reveal the ferroelectric state of the multiferroic film underneath the $Co_{.90}Fe_{.10}$. Figures 4.4(a) and 4.4(b) show the in-plane PFM images of an as-grown AMR structure before and after the etching of

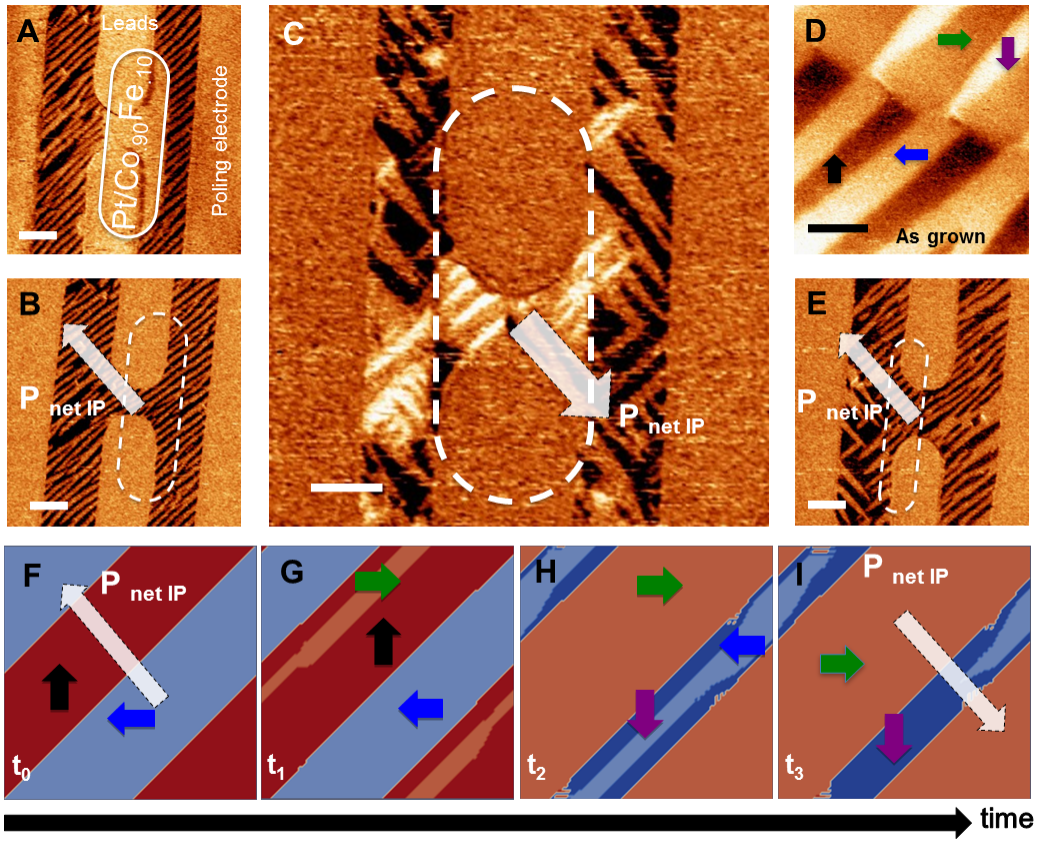

Figure 4.4: (a-b) In-plane PFM images before (a) and after (b) removal of the $Co_{.90}Fe_{.10}$ dot from an as-grown AMR structure. The white arrow gives the direction of P_{netIP} underneath the $Co_{.90}Fe_{.10}$ dot. (c) After the application of a 130 kV/cm pulse (oriented from left to right) and subsequent etching of the magnet, the ferroelectric architecture underneath the $Co_{.90}Fe_{.10}$ dot corresponds to a reversal of P_{netIP}. (d) IP-PFM image where both as-grown and reversed states of P_{netIP} coexist. The 90^o in-plane rotation of each single ferroelectric domain is represented by the colored arrows (black and blue to green and purple, respectively) and correspond to in-plane 71^o 3-D vector rotations. (e) Another structure which has been switched first by a 130 kV/cm pulse and followed by a -130 kV/cm pulse. The ferroelectric configuration reverts back to the as-grown state. (f-i) Phase field simulation of the ferroelectric switching of a multidomain $BiFeO_3$ film under an in-plane electric field (420 kV/cm) applied to the right. (f) is the as-grown state and (g-i) show the switching as a function of increasing time and under constant electric field, leading to the 180^o switch of P_{netIP}. The author aknowledges K. Ashraf and S. Salahuddin for the phase field simulations; similar work is given in reference [130].

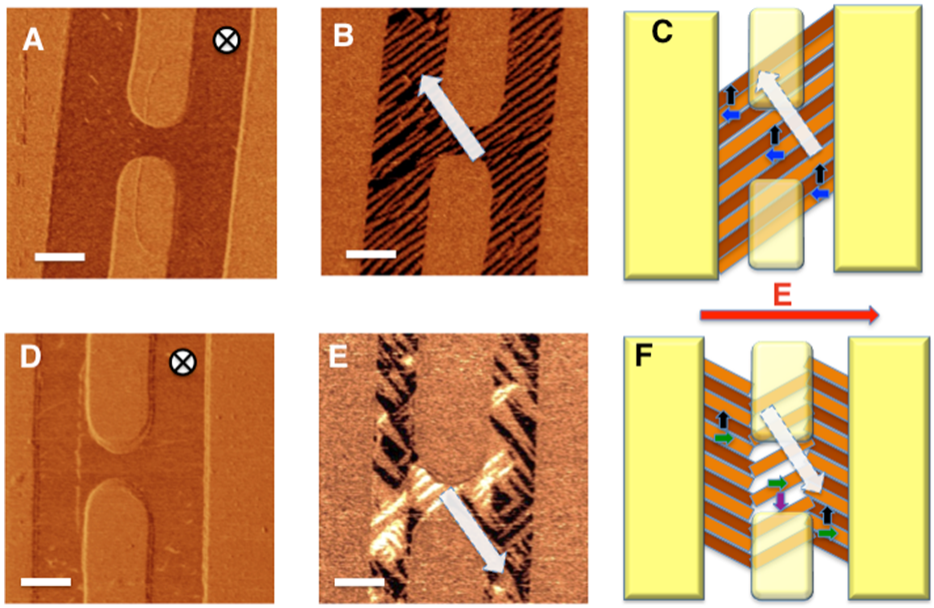

Figure 4.5: (a-b) Out-of-plane (a) and in-plane (b) PFM response of the AMR structure after etching the $Co_{.90}Fe_{.10}$ dot. (c) Schematic of the ferroelectric architecture corresponding to the in-plane PFM caption in (b). (d-e) Out-of-plane (d) and in-plane (e) PFM response of the AMR structure after the application of a 130 kV/cm pulse and the removal of the $Co_{.90}Fe_{.10}$ dot. Two different ferroelectric switching events are observed. Under the dot, the domain walls do not change direction from the as-grown state, however, the direction of P_{netIP} changes by 180^o. On both sides of the transport leads, where there was no $Co_{.90}Fe_{.10}$ during the application of the electric field, the domain walls reorient by 90^o in-plane which results in a 90^o switch of P_{netIP}. This configuration is illustrated in (f). The direction of P_{netIP} at the location where the $Co_{.90}Fe_{.10}$ dot once was, is given by the white arrows. The colored arrows in (c) and (f) give the directions of the in-plane polarization in each of the single ferroelectric domains. The scale bars are 1 μm.

the ferromagnetic dot. The dashed open white arrows give the directions of P_{netIP} under the $Co_{.90}Fe_{.10}$ dot. The continuity of the 71^o ferroelectric domain stripes after removing the $Co_{.90}Fe_{.10}$ proves that this controlled etching allows us to clearly visualize the domain configuration underneath the ferromagnet without altering the ferroelectric domain state. After a 130 kV/cm pulse, no domain wall reorientation occurred underneath the dot but the in-plane contrast change in Figure 4.4(c) reveals that P_{netIP} has rotated by 180^o with respect to the as-grown state. Importantly, no change in the out-of-plane polarization direction was observed (Figure 4.5). Figure 4.4(d) presents the ferroelectric architecture of the $BiFeO_3$ film where both as-grown and 180^o switched states coexist. The continuity of the ferroelectric domain walls across the boundary between as-grown and switched regions reveals that the 180^o switch of P_{netIP} consists of two 71^o (i.e. 90^o in-plane; one clockwise and the other counterclockwise) rotations of the single ferroelectric domains and confirms the 180^o switching event of P_{netIP} illustrated in Figure 3.9. The reversibility of the switching event is illustrated in Figure 4.4(e) which presents the observed domain configuration from a third structure after two successive switching pulses (130 kV/cm followed by -130kV/cm) were applied. The orientation of the 71^o stripes revert homogeneously back into a direction parallel to the as-grown state.

The overall reversal of P_{netIP} under the magnetic dot results as a consequence of two successive 71^o in-plane switching events. Figures 4.5(a) and 4.5(b) show the out-of-plane and in-plane PFM captures from an AMR structure in the as-grown state after the $Co_{.90}Fe_{.10}$ dot has been removed. The out-of-plane contrast is uniform and indicates that the out-of-plane component of the net polarization is pointing down into the film. The schematic in Figure 4.5(c) indicates the direction of the polarization in each single ferroelectric single domain (colored arrows) corresponding to the PFM capture in Figure 4.5(b). These lead to the defined net in-plane polarization (white arrow).

When a 130 kV/cm pulse is applied to the $BiFeO_3$ and again the $Co_{.90}Fe_{.10}$ dot is removed, no out-of-plane change of contrast is observed (Figure 4.5(a) and (d)). The ferroelectric switching event is purely in-plane. The contrast change observed in Figure 4.5(e) is represented in Figure 4.5(f). The net in-plane polarization switches by 180^o with respect to its direction in the as-grown state. However, outside of the area formerly covered by the magnet, the domain walls reorient by 90^o, leading to a 90^o in-plane rotation of the net polarization. This different ferroelectric behavior observed on both sides of the leads between the poling electrodes is attributed to the absence of screening that favors the reorientation of the domain walls. This fact is discussed later in this chapter.

4.4 Phase field simulations of the electrical switch

Electric-field driven phase field simulations reveal the origin of the observed P_{netIP} reversal underneath the $Co_{.90}Fe_{.10}$ dot. [130] Prior studies have shown that the 71^o and 109^o switching event in $BiFeO_3$ are characterized by two different coercive fields with $E_{c,71^o} < E_{c,109^o}$. [131] Considering the as-grown 71^o striped $BiFeO_3$ configuration represented in Figures 3.9(a) and 4.4(f), the high saturation polarization of $BiFeO_3$ causes all of the domains to arrange in-plane in a head-to-tail configuration so that the dipole-dipole energy is minimized. For an applied electric field of strength $E_{c,109^o} > E_{applied} > E_{c,71^o}$, the time evolution of the system demonstrates that the ferroelectric domains with an in-plane polarization oriented perpendicular to the applied electric field align first towards the direction of this external field (Figure 4.4(g)). This corresponds to a 71^o switching event due to the applied field (90^o in-plane). This switching, which had originally nucleated at the domain wall, generates an energetically unfavorable head-to-head configuration. Adjacent domains originally oriented antiparallel to the electric field then switch in-plane by 90^o (corresponding to a second 71^o switching event) under this dipole-dipole field to recover the preferred head-to-tail configuration of the polarizations (Figure 4.4(h)). P_{netIP} changes by 180^o, permitting the in-plane projection of the antiferromagnetic order to reverse without domain wall reorientation (Figures 3.9(b) and Figure 4.4(i)).

4.4.1 Phase field simulations: switching thresholds

Ferroelectric switching thresholds are determined by the coercive fields of individual domains, the domain wall energy and the duration of the applied electric field pulse. As described earlier, the $BiFeO_3$ polarization within a single ferroelectric domain variant must point along one of the <111> directions of the crystal. There are four in-plane polarization variants on the (001) plane of $BiFeO_3$. These different polarization variants are labeled P_1, P_2, P_3 and P_4 and are shown in the Figure 4.6.

When an in-plane electric field of sufficient strength is applied along the $[\overline{1}\overline{1}0]$ direction (along P_1), the polarizations along P_2, P_4 and P_3 will switch to P_1. In the switching process, P_2 and P_4 switch by 71^o while P_3 switches by 109^o. The projection of the 71^o and 109^o switches onto the (001) plane are 90^o and 180^o respectively. Figure 4.7 lists the calculated coercive fields and switching times for the 71^o and 109^o switching angles.

The coercive field of the 71^o switch is significantly lower compared to the 109^o switch. Consistent with previous phase-field simulations of $BiFeO_3$, the coercive field of the 71^o switch is significantly lower than the 109^o switch. [131] Thus, an in-plane 90^o (corresponding to the 71^o switch) switch occurs faster and at a lower coercive field than an in-plane 180^o switch (109^o).

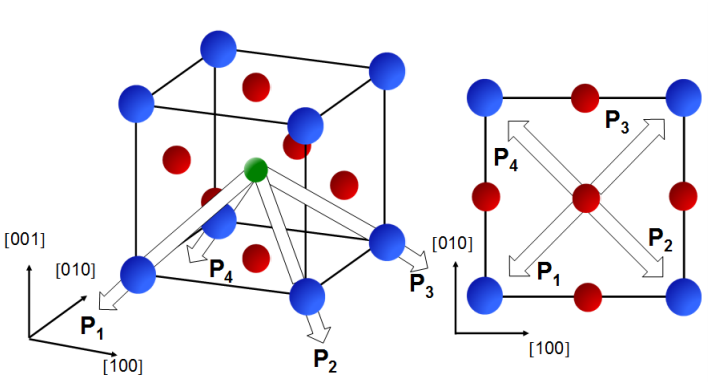

Figure 4.6: The possible in-plane polarization variants and their projection on the (001) surface of $BiFeO_3$. An in-plane electric field directed along P_1 causes all of the other polarization variants to switch by either 71^o or 109^o in 3-dimensions. These 71^o and 109^o switches project onto the (001) surface as 90^o and 180^o rotations.

Switch	Coercive field (kV/cm)	Switching time (unit)
71˚	420	63.1
109˚	490	127.2

Figure 4.7: Table listing the calculated coercive fields and switching times for the 71^o and 109^o switching events. The 109^o switch has a larger coercive field and a switching time roughly twice the 71^o switching time. The author aknowledges K. Ashraf and S. Salahuddin for the phase field simulations; similar work is given in reference [130].

4.4.2 ferroelectric switching at low electric field ($\mathbf{E}_{c,109^o} > \mathbf{E}_{applied} > \mathbf{E}_{c,71^o}$)

Simulation of the $BiFeO_3$ (001) surface in the as-grown state is shown in Figure 4.8(a). Two domain variants are present. The application of an in-plane electric field above the coercive field of the 71^o switch causes the vertically directed polarizations in the red domains to switch to the right (orange domains in Figure 4.8(c)), a 71^o switch. [130] Since the 109^o switch is significantly slower compared to the 71^o switch, the left oriented domains (light blue) do not switch within the time that the red domains switch. Note that the domain wall direction has not changed due to the first switch. The theoretical maximum limit of the dipole-dipole fields at these domain walls can reach up to ∼104 kV/cm due to the induced charge. To recover a head-to-tail configuration and minimize dipole-dipole field, the left oriented polarizations (light blue domains) switch downward (dark blue domains) by another 71^o switch (Figures 4.8(d) and 4.8(e)). [130] If the applied field is kept on, then downward oriented polarizations (dark blue domains) will switch to the right oriented orange domains within 63.1 [time units] at the coercive field. The lifetime of the dark blue domains decreases with increasing applied electric field. Note that the dark blue domains will be stabilized if the applied field is turned off before its lifetime. In that case, the net in-plane polarization performs a 180^o in-plane switch.

4.4.3 Switching at high electric field ($\mathbf{E}_{applied} > \mathbf{E}_{c,109^o} > \mathbf{E}_{c,71^o}$) in two variant films

In this regime, both 109^o and 71^o switching will occur. The configuration shown in Figure 4.8(a) will evolve to a monodomain state as in Figure 4.8(f). Once the system has reach a monodomain state, the ferroelectric architecture will break into domains as the field is turned off. The domain walls and hence the net in-plane polarization will rotate by 90^o in-plane. [130] This is illustrated in Figure 4.9.

4.5 Electric field induced magnetization reversal

The combination of phase field modeling and direct imaging of the ferroelectric domain structure of the same location before and after the application of the electric field establishes the notion that P_{netIP} rotates by 180^o underneath the $Co_{.90}Fe_{.10}$. The consequential effect on the canted moment in the $BiFeO_3$ layer (and thus on the $Co_{.90}Fe_{.10}$ magnetic moment) was probed using angle-dependent AMR measurements. It is well known that the AMR in a conventional ferromagnet follows a $R(\theta) = R_0 + (R_{//} - R_0)\cos^2(\theta)$ dependence, where θ is the angle between the magnetization and the current, while R_0 and $R_{//}$ are the resistances when $\theta = 90^o$ and 0^o. [132] High magnetic field (2000 Oe) resistance data taken from the as-grown state indeed show

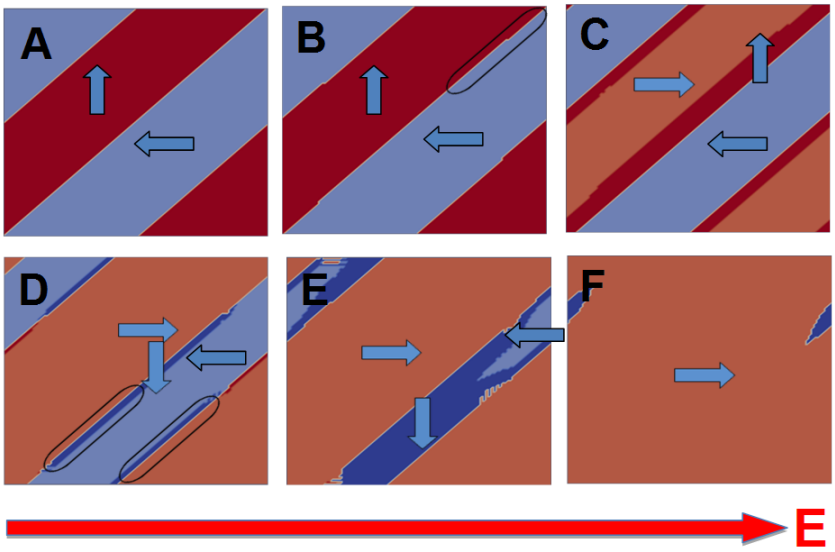

Figure 4.8: The lifetime of 180^o switch of P_{netIP} on the $BiFeO_3$ (001) surface. (a) The in-plane polarization directions in the as-grown state. (b) Initial switching begins at the domain walls when an electric field is applied in-plane and to the right with strength above the coercive field of the 71^o switch and below the 109^o switch. (c) Later, the vertical polarizations (red domains) switch to right oriented polarizations (orange domains). (d) The head-to-head configuration between the orange and light blue domains causes the light blue domains to switch by 71^o to dark blue domains at the domain walls. (e) The dark blue domains continue to grow, creating the favored head-to-tail configuration between orange and dark blue domains. (f) After the lifetime of the dark blue domains has been reached, the dark blue domains switch by 71^o to orange domains, eventually creating a monodomain state. The author aknowledges K. Ashraf and S. Salahuddin for the phase field simulations; similar work is given in reference [130].

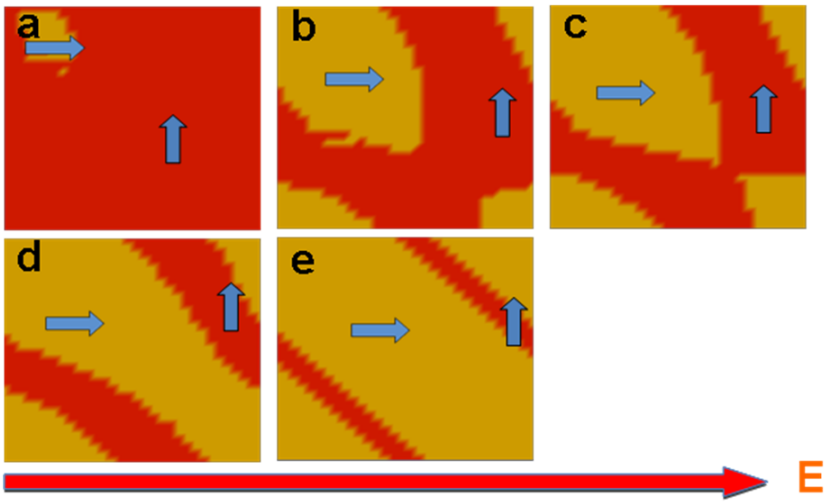

Figure 4.9: (a) Initially an up directed polarization (red domain) is taken as the monodomain and a right directed polarization (yellow domain) is taken as a seed domain. An in-plane electric field is applied towards the right. The strength of the applied field is lower than the coercive field for any switching, both at the domain wall and within the domain and is used to drive the system forward so that relaxation can be achieved within a reasonable simulation time. (b) As expected, domain wall switching from the up domain to the right domain begins quickly due to the system being far from equilibrium. (c, d, e) Eventually a quasi-periodic domain pattern is obtained that consists of up and right oriented domains and the domain walls are oriented along a line going across the body diagonal of the simulation grid. In the specific case of our in-plane switching and subsequent 90^o rotation of net in-plane polarization, the right oriented polarization acts as the majority domain and the up domain acts as the seed. The right oriented polarization originates due to the switching along that direction and the up directed seed domain is already present in the regions adjacent to the electrodes where switching has not occurred. The author aknowledges K. Ashraf and S. Salahuddin for the phase field simulations; similar work is given in reference [130].

a $\cos^2(\theta_a)$ dependence (black curve in Figure 4.10(a)), where θ_a is the angle of the applied magnetic field, indicating that, at this large magnetic field, the Zeeman energy dominates the other anisotropies and thus the $Co_{.90}Fe_{.10}$ magnetization follows the applied magnetic field (i.e. $\theta \sim \theta_a$). In contrast, at a low magnetic field of 20 Oe, the resistance follows a $\cos(\theta_a)$ dependence; in this case, the magnetization simply wiggles about the dominant anisotropy axis, which makes an angle of 45^o with respect to the direction of the current. This $\cos(\theta_a)$ dependence is plotted as the open red circles in Figure 4.10(a) and has been observed in other AFM/FM systems. [129, 123] The deduced orientation of the magnet with respect with the P_{netIP} is in agreement with the interfacial coupling evidenced previously and schematically represented in Figure 4.10(b). The AMR after the $BiFeO_3$ is electrically switched with a field of 130 kV/cm (and under zero magnetic field) is presented as the blue circles in Figure 4.10(a). The AMR retains the $\cos(\theta_a)$ type behavior; however, there is a 180^o phase shift in the AMR curve compared to the as-grown state. This 180^o phase change is the result of a change in the sign of the magnetic torque experienced by the magnetization, due to a magnetization reversal. Furthermore, below ∼100 kV/cm no change in the AMR response was observed. The data in Figure 4.10(a) is a representative of a large sample set (∼20 samples) where such a switching has been observed. Finally, the magnetic field was again turned off and the $BiFeO_3$ was poled with a -130 kV/cm pulse. The -130 kV/cm AMR data is plotted in green in the bottom panel of Figure 4.10(a) and is seen to be in phase with the as-grown curve. This illustrates that the magnetization has again reversed by 180^o, back into the as-grown direction.

4.5.1 Addressing magnetostriction

No change in the low field AMR curve after poling was observed for a heterostructure where a 2 nm $SrTiO_3$ spacer was inserted in between $BiFeO_3$ and $Co_{.90}Fe_{.10}$, indicating that magnetostriction is not the origin of this effect. AMR measurements were performed under a high (2000 Oe) and low (20 Oe) magnetic field on a $Co_{.90}Fe_{.10}$ (2.5 nm)/ $SrTiO_3$ (2 nm)/ $BiFeO_3$ heterostucture and are shown in Figure 4.11. Figure 4.11(a) shows the AMR data from the as-grown state (open red circles). The growth field was applied along the direction of P_{netIP}. The signal plotted in the lower panel (open black circles) was obtained after the application of -2000 Oe magnetic field to reverse the magnetization of the dot previously oriented along the growth field. The 180^o shift of the AMR curve with respect to the as-grown curve is a result of a change in the sign of the torque felt by the reversed magnetization from the 20 Oe applied magnetic field. The schematic in Figure 4.11(b) represents the relative directions of the $Co_{.90}Fe_{.10}$ moment and $BiFeO_3$ net in-plane polarization.

The open red circles in the top panel in Figure 4.11(c) are the data from the as-grown state. After removing the magnetic field and the application of a 130 kV/cm pulse, the AMR signal plotted in the middle panel (open blue circles) was obtained. No phase difference between the 130 kV/cm and the as-grown curves is present,

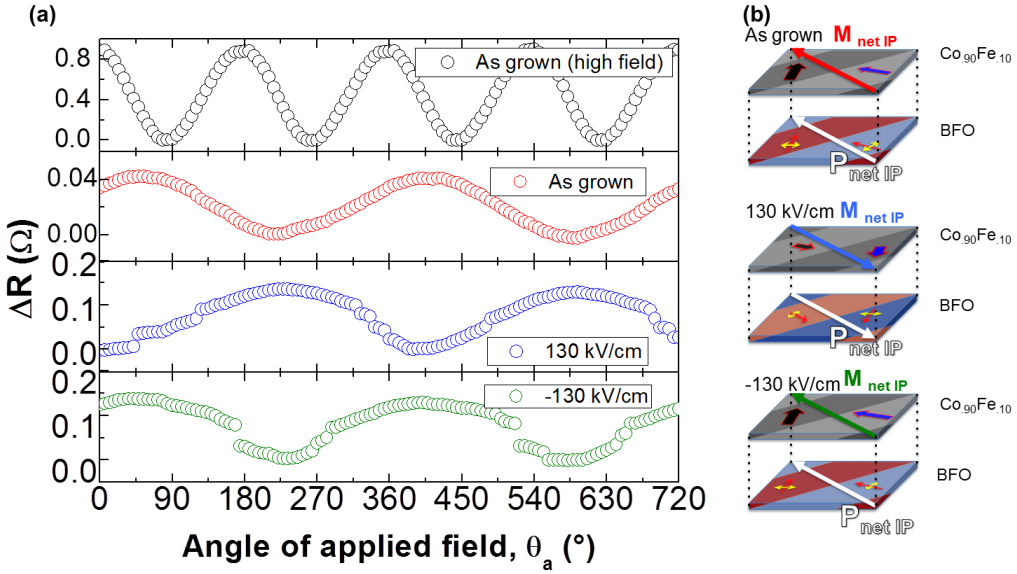

Figure 4.10: (a) Open black circles show the high field (2000 Oe) AMR response (top panel). The low field (20 Oe) AMR response for the as-grown state is plotted with the open red circles (second panel from top). The open blue circles show the low field AMR after pulsing an electric field of 130 kV/cm in zero magnetic field (second panel from bottom). Application of a -130 kV/cm electric field pulse at zero magnetic field results in the recovery of the phase of the as-grown low field AMR response (open green circles - bottom panel). (b) Representation of the one-to-one magnetic interface coupling in the $BiFeO_3$ / $Co_{.90}Fe_{.10}$ heterostructure in the as-grown state, after pulsing an electric field of 130 kV/cm, and -130 kV/cm.

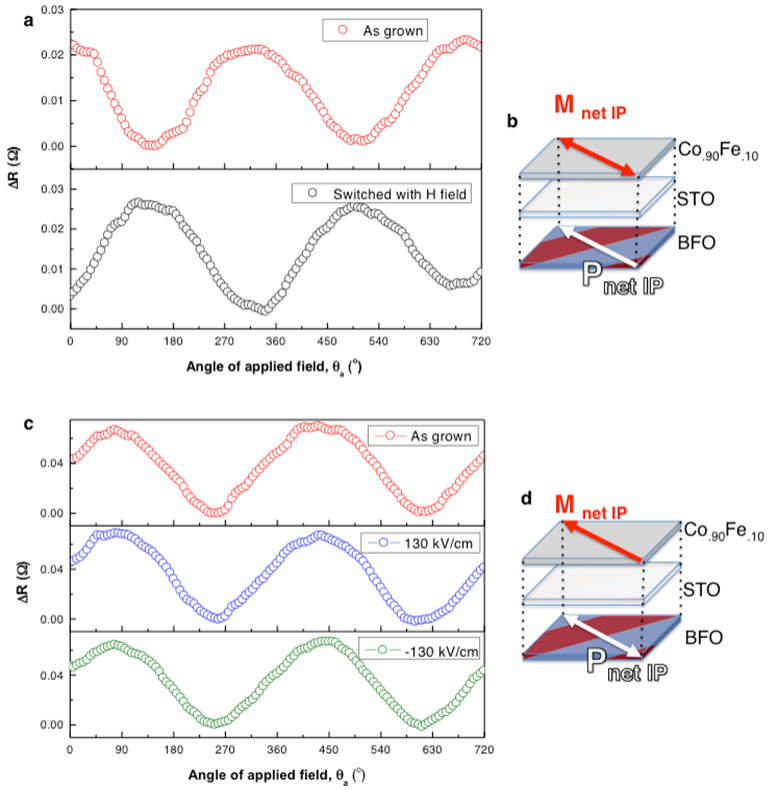

Figure 4.11: All AMR measurements were performed under a 20 Oe magnetic field. (a) AMR measured from a $Co_{.90}Fe_{.10}$ (2.5 nm)/ $SrTiO_3$ (2 nm)/ $BiFeO_3$ heterostucture in the as-grown state (open red circles - top panel) and after switching the magnetization of the $Co_{.90}Fe_{.10}$ dot using a -2000 Oe magnetic field. (b) Schematic of the heterostructure with the $SrTiO3_3$ layer inserted in between the $Co_{.90}Fe_{.10}$ and the $BiFeO_3$ layers giving the relative directions of the moment in the magnet and the net in-plane polarization in $BiFeO_3$. (c) AMR measured in the same architecture in the as-grown state (open red circles - top panel) and as a function of applied voltage (open blue and green circles - middle and bottom panels). No change in the phase of the AMR signal is observed for any of the voltage pulses. (d) Schematic of the structure. Reversing P_{netIP} reorients the magnetic order in the $BiFeO_3$ layer, however, the inserted layer prevents the magnetization reversal.

indicating that the magnetization has not rotated from the as-grown direction. The bottom panel shows the AMR data obtained after applying a -130 kV/cm pulse under zero magnetic field. Again, this curve shows no phase difference compared to the as-grown measurement. Since the magnetization was not rotated during this measurement, we conclude that the observed magnetization reversal shown in Figure 4.10 is not an effect of magnetostriction. The independence of the switching events in the $BiFeO_3$ and the direction of the $Co_{.90}Fe_{.10}$ moment is represented in Figure 4.11(d).

4.6 Concluding remarks and issues

The robust, one-to-one magnetic coupling between a ferromagnetic layer and the multiferroic magnetoelectric $BiFeO_3$ and its use to cause the 180^o reversal of the magnetization in the ferromagnet is a seminal development for the use of multiferroics in future applications. This new method of magnetization reversal is a critical advancement to the field of spintronics since it provides an additional pathway to all electrical based spintronics and, uniquely, it relies solely on the application of an electric field. This ferromagnet-multiferroic system creates a pathway to the realization of room temperature, non-volatile, and low-power consumption spintronics devices.

Nonetheless, there are still several short comings in our demonstration in light of possible applications. Those being:

1. Each domain rotates 90^o and sum to yeild a 180^o reversal. In an ideal case the device would be small enough to reside in a single multiferroic domain, hence a 180^o at the domain scale is required.

2. From the phase field simulations, it is clear that the electric field for switching requires special consideration in terms of amplitude and time of voltage application.

3. Large in-plane voltages are still needed. While reduced from $\sim$200V, 70V is still too large for applications.

4. The in-plane device geometry requires a large surface area making high density devices unlikely.

Chapter 5

Electric field control of ferromagnetism: out-of-plane switching

In the previous chapter it was shown that by using the one-to-one correlation between ferromagnetic and multiferroic domains in a $Co_{.90}Fe_{.10}/BiFeO_3$ heterostructure the magnetoelectric switching and single domain order parameters of $BiFeO_3$ were investigated. Additionally, an in-plane oriented electric field causes the projected polarization and canted moment to rotate 90^o within each domain. To continue the investigation of the magnetoelectric switching of $BiFeO_3$, we now head in the direction of applying an out-of-plane voltage. This geometry has additional technological benefit as as well, namely the voltage will be applied through the thickness of the $BiFeO_3$ film (150nm) reducing the require voltages from 70V to single digit voltages and the removal of in-plane electrodes greatly reduces the size of the device.

5.1 Experimental methods

5.1.1 Details of $BiFeO_3$ / $SrRuO_3$ growth

The (001) oriented films used in this study were fabricated by pulsed laser deposition (PLD) using a KrF laser on single-crystalline (110) $DyScO_3$ substrates. First a thin layer of conducting $SrRuO_3$ (5nm) was deposited and followed by the $BiFeO_3$ thin film (70-120 nm thick). A substrate temperature of 700 ^{o}C was used in an oxygen pressure of 100 mTorr, at a repetition rate of 8 Hz with a laser fluence of 1.1 J/cm^2. After growth, the samples were cooled to room temperature in an O^2 pressure of 750 Torr. The $DyScO_3$ provides a small anisotropic strain to the rhombohedral $BiFeO_3$ resulting in an induced anisotropy in the $BiFeO_3$ domain structure which is composed of two polarization variants. The $SrRuO_3$ layer was deposited as a con-

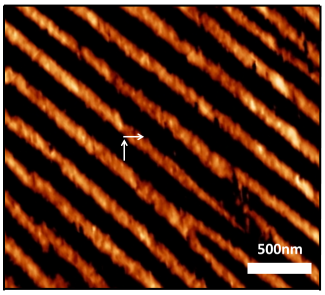

Figure 5.1: PFM image of the $BiFeO_3/SrRuO_3/DyScO_3$ heterostructure revealing the characteristic 71^o stripe-like ferroelectric domains (white and black stripes). The white arrows indicate the in-plane projections of the polarizations associated with each domain variant.

ducting layer to be used as a back electrode for the application of vertical electric fields. Figure 5.1 shows a piezoresponse force microscopy (PFM) image performed on the $BiFeO_3/SrRuO_3/DyScO_3$ heterostructure and the characteristic 71^o stripe-like ferroelectric domains. [107] Each of the ferroelectric variants projects at 90^o from each other onto the (100) surface (white arrows in Figure 5.1). For each of these ferroelectric domains there is an associated canted moment that points along the [11$overline$2] whose projection onto the (100) surface is parallel to the projected polarization. The average domain width in as-grown films are 150-250nm. The (001) projections of the two ferroelectric variants add up to a macroscopic polarization (P_{netIP}) that points perpendicular to the domain walls. [128]

5.1.2 Details of $Co_{.90}Fe_{.10}$ / Pt growth

After the growth of the $BiFeO_3$ films, they were immediately inserted into a vacuum sputtering chamber with a base pressure of $\sim 3x10^{-8}$ Torr. $Co_{.90}Fe_{.10}$ (2.5nm)/ Pt (2.5nm) layers are deposited by DC magnetron sputtering onto the $BiFeO_3$ films at room temperature in a argon background of $8x10^{-4}$ Torr. The $Co_{.90}Fe_{.10}$ layer is deposited under a 200 Oe growth field that is oriented along the P_{netIP} direction of the $BiFeO_3$ film. The device is capped with Pt (2.5 nm) to prevent oxidation of the other layers. As shown in previous chapters, the domain structure of the multiferroic can be induced in an exchange coupled $Co_{.90}Fe_{.10}$ layer by coupling to the weak ferromagnetic moment in each domain of the $BiFeO_3$. [128, 50] and this coupling results in a one-to-one mapping of the induced ferromagnetic domains in $Co_{.90}Fe_{.10}$ to the multiferroic $BiFeO_3$ domains. This coupling can be confirmed easily using magnetic force microscopy (MFM) where the MFM tip is senitive to the out-of-plane component of the magnetization. [50] Figure 5.2(a) shows the MFM image obtained from

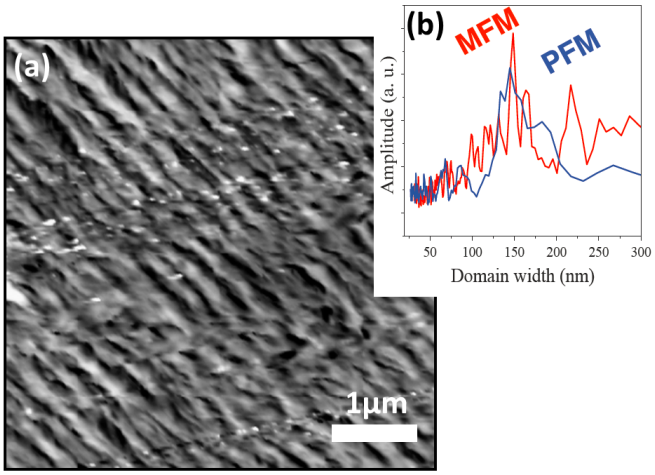

Figure 5.2: (a) MFM image of the $Co_{.90}Fe_{.10}$ domain structure when coupled to $BiFeO_3$. A stripe-like domain structure is clearly revealed. (b) Fourier analysis of the spectrum of the domain widths reveals that the domain widths observed by PFM and MFM are correlated with most domains having a width $\sim$ 150nm.

the surface of the $Co_{.90}Fe_{.10}$ / $BiFeO_3$ heterostruture. Stripe-like domains are cleary observed. The MFM contrast is observed from the fringing magnetization emerging from the magnetic domain walls since the MFM tip is only sensitive to out-of-plane components of magnetization and the moments in the $Co_{.90}Fe_{.10}$ domains lay in the plane of the film. To determine the population of domain widths in the multiferroic and in the $Co_{.90}Fe_{.10}$, Fourier analysis of the MFM and PFM images were perfomed (see Figure 5.2(b)). The spectrum of the two images are closely correlated and share a peak around 140-150nm. This clearly illustrates the domain correlation between the two layers.

5.1.3 Patterning of $Co_{.90}Fe_{.10}$ dots and definition of contacts

The $Co_{.90}Fe_{.10}$ / Pt layers are then patterned into dots with areal dimensions of 2x6 μm^2, 6 μm diameter and 16 μm diameter circles using photolithography and argon ion milling. These bits are defined by etching the surrounding metallic layers down to the underlying $BiFeO_3$ film. Then, electrical contact is made to the dots with Cu/Pt contacts using a photolithographic liftoff process.

5.1.4 Resistance measurements

The devices were measured using a simple two wire geometry using a keithely 220 current source and a keithely 181 nanovoltmeter. Typical device resistances were

between 90 and 200 ohms and displayed linear I(V) curves within our applied current range (1μA - 5μA). The devices are measured in a system where an in-plane magnetic field can be applied to the sample and the sample can be rotated as the resistance is measured. This allows us the flexibilty to measure the device resistance as the device is rotated in a constant magnetic field or to measure the device resistance as the magnetic field is swept, keeping the angle of the sample with respect to the applied magnetic field constant.

5.2 Experimental results and discussion

5.2.1 Switching under the $Co_{.90}Fe_{.10}$

To understand any evolution of the $Co_{.90}Fe_{.10}$ magnetization in response to a vertically applied electric field, $BiFeO_3$'s response to the voltage must first be known. To determine the response to the voltage, a simple device was used (Figure 5.3(a)). The device consists of a 2x6 μm^2 dot of $Co_{.90}Fe_{.10}$ / Pt on top of $BiFeO_3$ with a $SrRuO_3$ back electrode. Using a PFM tip to apply a voltage to the $Co_{.90}Fe_{.10}$ / Pt while keeping the $SrRuO_3$ at ground, an electric field can be applied through the thickness of the $BiFeO_3$. Two devices were used to switch the $BiFeO_3$. The first device was switched once with a negative voltage (-V) while the second was switched twice, first with negative voltage and then followed with a switch with a positive voltage (-V, +V), where V = 9V. To unveil the $BiFeO_3$ underneath the $Co_{.90}Fe_{.10}$ / Pt, a soft Ar ion milling was performed to remove the $Co_{.90}Fe_{.10}$ / Pt. After the removal, the two devices were imaged by PFM.

Figures 5.3(b) and (c) show the in-plane PFM images obtained from the device that was switched (b) once and the device that was switched (c) twice. The striped domain structure is preserved after one switch, however, the color contrast of the stripes has changed from black to white. The direction of P_{netIP} (large white arrows) is reversed in the region of the applied voltage, when compared to the as-grown state surrounding the switched region (Figure 5.3(b)).

The striped domain structure is preserved after 2 switches (Figures 5.3(c)). After two switches, the PFM contrast at the electrically cycled region is the same as the contrast of the as-grown region. This reveals that the P_{netIP} is parallel for the electrically cycled and as-grown regions and additionally reveals that P_{netIP} can be reversibily switched with an out-of-plane single digit voltage.

5.2.2 Domain evolution from out-of-plane voltage

Figures 5.3(b) show that the orientation of the striped domains remained unchanged after a applied voltage. It is another question, however, to ask what the evolution of the ferroelectric polarization when going from the as-grown to the switched

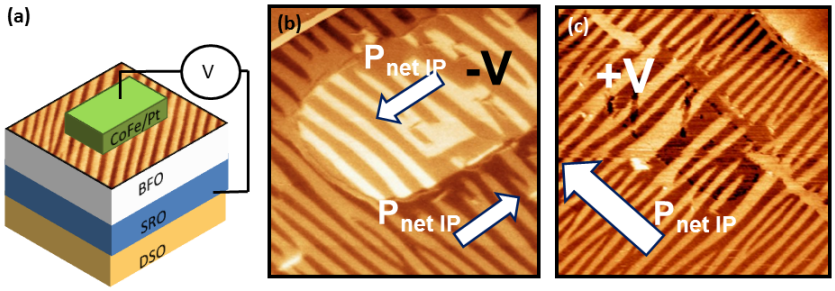

Figure 5.3: (a) A schematic of the device used for studying the switching of the $BiFeO_3$ underneath the $Co_{.90}Fe_{.10}$ dot using out-of-plane voltage. The voltage is applied through the thickness of the $BiFeO_3$ layer using the $SrRuO_3$ and $Co_{.90}Fe_{.10}$ / Pt as bottom and top electrodes. The $Co_{.90}Fe_{.10}$ / Pt was thren removed using Ar ion milling. (b) and (c) show the in-plane PFM images of the $BiFeO_3$ domain structure after (b) one switch with negative voltage and after (c) two switches (one negative, then positive).

state. Figure 5.4 shows a detailed PFM analysis that illustrates the nature of the ferroelectric switching event within each ferroelectric domain. In Figure 5.4 the in-plane and out-of-plane PFM images show a region where the switched and as-grown regions meet. A close inspection of the in-plane PFM images reveal that the ferroelectric domains remain coherent across the boundary of switched and as-grown regions. Both the in-plane and out-of-plane components of the polarization switch by 180^o with respect to its neighboring as-grown domain. In the previously reported planar electric field geometry [54, 128], the reversal consists of two 90^o rotations of the in-plane component of the polarization in adjacent ferroelectric domains. The coherent transition of the domains and domain walls from the as-grown to switched regions also suggests that electrical switching occurs within each domain rather than by the movement of the ferroelastic 71^o domain walls.

The next step is to address if this switching is magnetoelectric. Next, the focus is on the absolute direction of the magnetization vector in each of the $Co_{.90}Fe_{.10}$ domains. This is imaged using scanning electron microscopy with polarization analysis (SEMPA). The X and Y in-plane components of the $Co_{.90}Fe_{.10}$ layer's magnetization can be resolved below the length scale of a single domain ($\sim$150nm). Figure 5.5(a) shows the as-grown configuration of the magnetic domains. A striped domain contrast is observed. The direction of the local moments are given by the color wheel and the moments sum to a net magnetization (M_{net}) direction (given by the white arrow).

The SEMPA image obtained from the device after applying a -7V voltage pulse across the $BiFeO_3$ is shown in Figure 5.5(b). The orientation of the striped magnetic

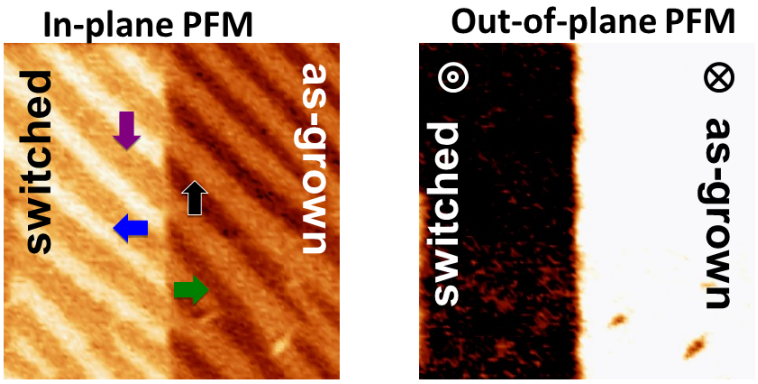

Figure 5.4: In-plane and out-of-plane PFM images of a region that contains both the as-grown and switched regions. The switched region has been switched with the application of a negative voltage. Arrows represent the in-plane component of the ferroelectric polarization in its associated domain.

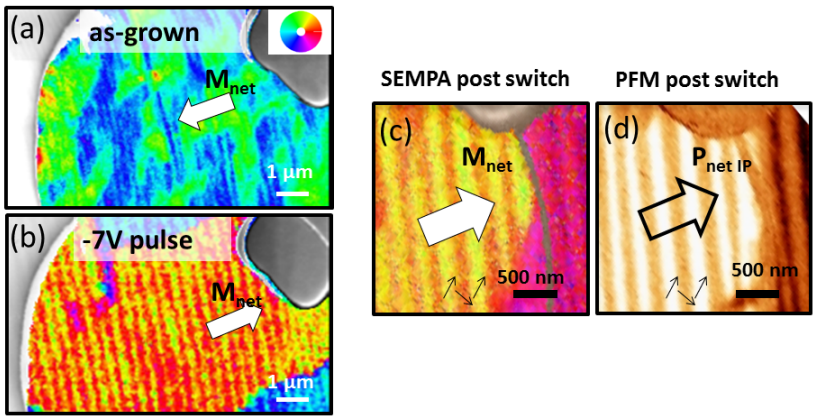

Figure 5.5: (a) SEMPA image of the AMR device structure in the as-grown state. The net magnetization (M_{net}) direction is indicated by the white arrow. The color wheel indicates the orientation of the local magnetic moment. (b) SEMPA image after a -7V voltage pulse. M_{net} has reversed direction and the striped domain pattern is preserved after the pulse. (c) A closer look at the domain structure in (b) to show the local orientation of the magnetic moments in each domain. (d) An in-plane PFM image of the region shown in (c) after the removal of the $Co_{.90}Fe_{.10}$. The images in (c) and (d) reveal that the correlated domain structure is preserved after the electrical switch. Furthermore, the comparison of the images in (c) and (d) reveal that the collinear alignment of the in-plane projection of the polarization and the $Co_{.90}Fe_{.10}$ moment is also preserved after the switch.

domains remains unchanged after electrical switching, however, the color contrast of the domains has changed. An inspection of the color wheel shows that the net magnetization (M_{net}) direction reverses from the as-grown direction. This is a clear demonstration that the macroscopic magnetization can be reverse with a mere -7V in this geometry. To correlate the macroscopic switching with the switching at the domain scale, a combination of SEMPA and PFM imaging is employed.

The ability to induce a local 180^o polarization switching in the $BiFeO_3$ layer (Figure 5.4) and the one-to-one domain structure with $Co_{.90}Fe_{.10}$ (Figure 5.2), makes the heterostructure the ideal system to probe the effect of a 180^o polarization switch on the canted moment. After the application of the -7V voltage pulse, the SEMPA contrast has changed from blue to red while keeping a coherent stripe like domain structure (Figures 5.5(a) and (b)). A detailed analysis of the corresponding SEMPA contrast and $BiFeO_3$ ferroelectric domains (Figures 5.5(c) and (d)) show that the collinear arrangement of the ferromagnetic moments and the ferroelectric ordering is preserved after the application of an electric field. Therefore, at the single domain scale, a 180^o out-of-plane ferroelectric switching event corresponds to an in-plane 180^o reversal of the magnetization direction.

5.2.3 Electrical control of a magnetotransport device

The net magnetization reversal was probed by measuring the anisotropic magnetoresistance (AMR) at a magnetic field of 20 Oe, below the coercive field of the system. This effectively keeps the net magnetization pinned about its remnant direction. The top panel of Figure 5.6 shows the AMR curve while the system is in the as-grown state (open blue circles). The AMR shows a $\cos(\theta_a)$ like dependence similar to that observed in Figure 4.10. After the application of -7V across the thickness of the film, at zero magnetic field, the low field AMR is recorded as the orange curve shown in the middle panel of Figure 5.6. This curve is phase shifted by $\sim 180^o$ with respect to the as-grown AMR curve indicating that the magnetization orientation of the $Co_{.90}Fe_{.10}$ domains evolved in such a way that the net magnetization state has reversed. The reversibility of the switching was investigated with AMR measured after the application of the opposite polarity (7V) pulse. The curve is shown in the bottom panel (open purple circles) and is now in phase with the as-grown curve revealing that the magnetization has reversed back to its original direction. Figure 5.6 also shows in-plane PFM images of two AMR devices that have ben etched to remove the $Co_{.90}Fe_{.10}$ and open the $BiFeO_3$ domains for PFM imaging. One device was etched after the observation of a single magnetization reversal while the other was etched after the observation of two magnetization reversals (a complete electrical cycle). In both cases the evolution of the ferroelectric domain structure, P_{netIP}, and M_{net} follow the observations made in Figures 5.3 and 5.5(b).

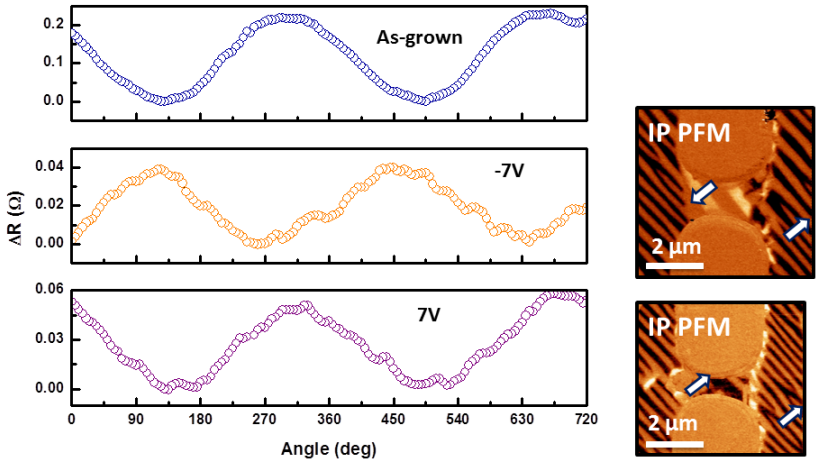

Figure 5.6: In-plane and out-of-plane PFM images of a region that contains both the as-grown and switched regions. The switched region has been switched with the application of a negative voltage. Arrows represent the in-plane component of the ferroelectric polarization in its associated domain.

5.3 Discussion: Mechanism of reversal

A reversal of the antiferromagnetic axis being energetically unlikely [51], this observation reveals that the ferromagnetic moments can be reversed as the canted moment vector rotates by 180^o due to the electrical reversal of the polarization. Projected 90^o in-plane rotations of this vector have been deduced from previous observations involving 71^o ferroelectric switching events [54, 128] and can be attributed to a rotation of the polar axis containing the non-polar distortion. For a 180^o switch, two mechanisms can be at the origin of the polar inversion effect on the canted moment's direction. The anisotropic strain state imposed by the $DyScO_3$ substrate could favor a coupling between rotational and polar distortions, which is a necessity for the electrically induced reversal [51, 52, 133]. An alternative to such a linear magnetoelectric coupling based mechanism involves a sequential rotation of the polar axis. Sequential switching, consisting of successive out-of-plane 71^o and 109^o events have been reported [131] as composing a 180^o ferroelectric switching event. The 71^o and 109^o events have corresponding rotations of the non-polar distortion, thus carrying the uniaxial anisotropy and magnetization with the polarization rotation, leading to a switch of the canted moment and a magnetization reversal.

5.4 Issues, outlook, and concluding remarks

In summary, it has been shown that using the imprint of the multiferroic domain structure into the ferromagnetic architecture of an exchange coupled $Co_{.90}Fe_{.10}$ layer,

yields a domain structure of nanosized stripes that provide a map of the underlying canted moment. The out-of-plane configuration reduces the magnetic switching voltage by an order of magnitude when compared to the planar configuration. The electrically induced reversal of the magnetization of the $Co_{.90}Fe_{.10}$ layer is due to the local magnetization reversal at the domain scale (∼150nm). This observation illustrates, from fundamental and application point of views, the potential for the control of nano-sized magnetic junctions using magnetoelectric multiferroics. Furthermore, the ability to induce the formation of electrically controllable ferromagnetic domains in a $Co_{.90}Fe_{.10}$ layer offers new opportunities for magnetoresistive devices.

Before this observed electrically driven magnetization reversal can impact technology, several issues which were encountered in this study must be addressed.

1. **Mechanism:** As it was discussed in the previous section, the mechanism of the magnetization reversal is not understood fully and is theoretically forbidden for a 180^o ferroelectric switch. The magnetization reversal at the single domain scale has been revealed through SEMPA imaging. The ferroelectric switching process driving such a reversal is not clear from the techniques presented in this chapter. For this reason, two possibilities are proposed. The first being that a coupling between the polar and non-polar distortions exists in this epitaxially constrained thin film. The theoretical arguments presented in [51, 52, 133] stem from a unstrained rhombohedral unit cell and with no consideration of the switching dynamics during the ferroelectric switch. The question is, can the epitaxial constraints alter these assumptions, leading to a pathway of electric field reversal of a magnetization?

2. **Robustness:** Earlier it was shown that the magnetization can be reversed with the polarization reversal. Many cycles of such an observed magnetization reversal are needed to impact technology and lead to an insight of the physical mechanism driving such a reversal. Cycling beyond 10 switches has been a challange in these devices. Such a robustness issue can come from $BiFeO_3$ and back electrode quality (leakage, ferroelectric imprint). Breakdown of the ferroelectric is a common occurance and large internal biases has alos been observed, making ferroelectric switching quite challanging. Ferroelectric/metal interfaces have plagued applications due to the trapping of defects at the ferroelectric/metal interface causing internal electric fields that freeze the polarization. Optimization of the $BiFeO_3$ to reduce defect related issues is required. Additionally, the quality of the $BiFeO_3/Co_{.90}Fe_{.10}$ is to be considered. Ideally, high quality $BiFeO_3$ and $Co_{.90}Fe_{.10}$ layers would be deposited in-situ to keep the interface free from atmospheric conditions and hydrocarbons.

Chapter 6

Demonstration of a energy efficient magnetoelectric memory

6.1 Background and motivation

Aside from understanding the physics that bridges electricity and magnetism in materials, the motivation for the electric field control of magnetism lies in the obstacles to the development of spin based memory and logic devices (i.e. the need for a large current to generate the spin injection or accumulation necessary to reverse a magnetization). This large current is responsible for the significant energy dissipation and material degradation issues that face spin based technologies. While discoveries such as the giant spin Hall effect have demonstrated a way to generate a spin torque that is expected to minimize barrier degradation in magnetic tunnel junctions, a current density that is of the same order as conventional spin transfer torque is still required. [134, 135] To eliminate these issues, the ideal control of magnetic devices would employ an electric field, rather than current, for switching. [136] Attempts to demonstrate the electric field control of magnetic tunnel junctions with perpendicular magnetic anisotropy (PMA) have demonstrated an electric field assisted magnetic switching and a reduced current to induce spin transfer switching through electric field modulation of the PMA. [137, 138] These methods, however, still require an external magnetic field, increase the overall energy consumption of the device.

Multiferroics present themselves as an energy efficient solution to the issues of current based spintronics due to the magnetoelectric interactions that link the ferroelectric and (anti)ferromagnetic orders in these materials. This is one of the driving factors which has brought about the renaissance of multiferroics research. [119, 118, 43, 23] Furthermore, these interactions enable the electric field control of magnetic order. [120, 139, 121, 140, 53] In the previous chapter, we showed that the magnetization of a $Co_{.90}Fe_{.10}$ layer in contact with two variant $BiFeO_3$ can be reversed (on both microscopic and macroscopic scales) with a small voltage pulse. It

is interesting to see if this materials system can be integrated into spintronic devices whereby the low-energy energy control of these devices can be demonstrated. of such a device.

The concept of integrating magnetoelectrics and multiferroics into spintronic devices was first proposed by Ch. Binek and B. Doudin.[61] They proposed two primary schemes of integration. The first is when the magnetoelectric is inserted in between two ferromagnetic layers to form a magnetoelectric magnetic tunnel junction. Magnetic tunnel junctions (MTJs) are a stacked materials sequence in the form of FM/Insulator/FM. These structures display large changes in the electrical resistance across the insulating layer as a magnetic field is cycled and the electrons must tunnel across the insulating layer to the opposite ferromagnetic layer in order to have electrical conduction. The changes in resistance are quantified in terms of a resistance ratio known as the tunneling magnetoresistance ratio (TMR), which can be as large as ten thousand percent. For more on MTJs see ref. [141]. Ch. Binek and B. Doudin propose that the resistance state of a magnetoelectric magnetic tunnel junction can show two different resistance states at zero magnetic field depending on how a voltage would be applied to the tunnel barrier. This construction would permit the electric field control of the device resistance and hence no external magnetic field or large currents are necessary for the writing of the device state.

They also propose that a magnetoelectric multiferroic can be used as an electrically controllable pinning layer, which magnetically pins one of the magnetic layers (also refered to as the pinned layer) in a magnetoresistive (MR) based device, such as an MTJ. The electrical control of the MR device is mediated by the electric field manipulation of the magnetization of the pinned magnetic layer through interface exchange coupling with the multiferroic. This latter case is the approach that I have been pursuing throughout this work. These two proposed devices are shown in Figure 6.1.

The concept of using a magnetoelectric multiferroic as an electrically controllable pinning layer was taken a step further by M. Bibes and A. Barthelemy [142] in light of the results shown by Y-H. Chu *et al.*[54] Here they propose a structure similar to what was proposed in [61]. However, they include a conducting back electrode for the application of a voltage and call it a magnetoelectric memory or possible magnetoelectric random access memory (MERAM). Their sketch, shown in Figure 6.2, shows the hysteretic behavior of the resistance as a function of the voltage applied to the multiferroic layer and shows the device in the two resistance states allowed at zero magnetic field. The appeal of this device, and those proposed in [61], in theory, is that it combines the advantages of ferroelectric RAM (FeRAM), such as quick and low-power writing, and magnetic RAM (MRAM), such as non-volitility and easy read-out of the state, and eliminates either of their individual disadvantages (destructive reading of the state and high-energy writing).

There have been some notable attempts to realize this magnetoelectric memory at room temperature. Their attempts have several barriers that have prevented them

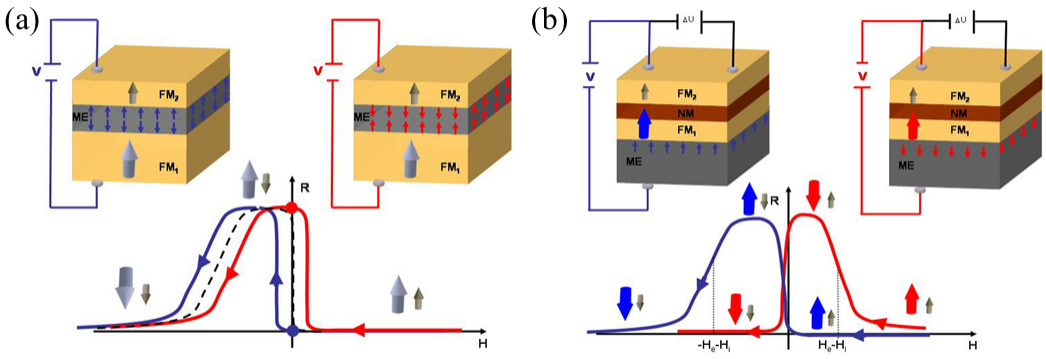

Figure 6.1: The two proposed device schemes for combining magnetoelectrics and spintronic devices. The two concepts use magnetoelectrics as an electrically controllable (a) tunnel barrier and (b) pinning layer. Figure from [61].

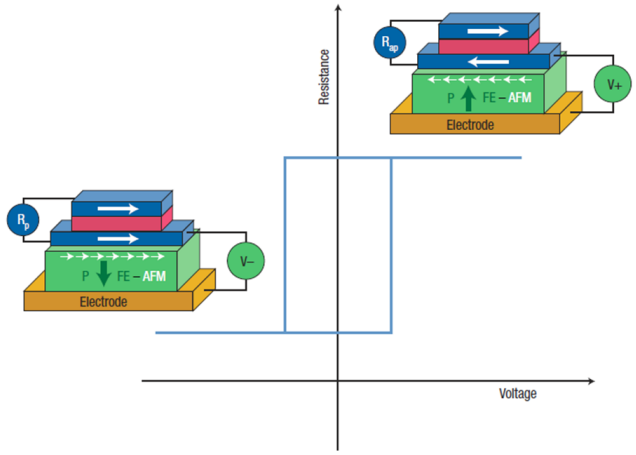

Figure 6.2: Schematic of the proposed magnetoelectric memory and its operation. The voltage applied to the magnetoelectric multiferroic causes the polarization to reverse, reversing the magnetic structure in th multiferroic at the multiferroic/ferromagnet interface. This results in the reversal of the magnetization of the pinned magnetic layer in the spin valve due to the interface exchange coupling. Since the free layer is now the reference layer, and remains fixed, the resistance of the device changes. The resistance versus the applied voltage loop reveals the hysteretic switching of the multiferroic and leads to the two stable resistance states at zero magnetic field. Figure from [142].

from realizing such a device. There have been reports of controlling or modulating a spin valve device using the piezoelectric property of ferroelectrics [143, 144] or the magnetoelectric coupling of $BiFeO_3$. [145, 146] The demonstration of the control in ref. [143] is quite robust. The use of mechanical strain is inhibited with the ability to rotate a magnetization a maximum of 90^o as a consequence of preserving time reversal symmetry. This ultimately reduces the differential resistance between on and off resistance states. While the use of mechanical strain can still be quite useful, the percent changes in resistance can be greatly increased if the magnetizations can be electrically switched between parallel and antiparallel states. This is the intention behind using $BiFeO_3$ based spin valves, but the approach used in [145] has been to electrically control the spin valve through the observed exchange bias between $BiFeO_3$ and a pinned ferromagnetic layer. This methodology suffers from the issue of the exchange bias driven by the magnetic and metastable 109^o domain walls in $BiFeO_3$. [145, 147, 105, 148] Upon application of a voltage, the 109^o domain walls begin to be wiped away and the preferred 71^o domain walls appear. The consequence results in the decrease of the exchange bias to near zero and reduction the MR in a non-reversible fashion.

As presented in the previous chapters, I approach the electrical control of an exchange coupled ferromagnetic layer from the basis of a domain coupling to $BiFeO_3$ rather than a domain wall coupling. This allows the electrical poling to stable states. In this chapter, I will discuss the work that shows the electric field control of a multiferroic-spin valve device by simply applying small voltages (4-9V) to reverse the magnetization of the pinned layer. This ultimately demonstrates the concept of a magnetoelectric memory. Lastly, I compare the energy consumption of our writing process to that of well established memories. This demonstration is already an order of magnitude more energy efficient than optimized spin transfer torque while still providing simple pathways to reduce this energy consumption even further.

6.2 Experimental methods

6.2.1 Details of $BiFeO_3$ / $SrRuO_3$ growth

The (001) oriented epitaxial $BiFeO_3$ (200-300 nm thick)/$SrRuO_3$ (8nm) thin films used for this study were fabricated by pulsed laser deposition (PLD) using a KrF laser on single-crystalline (110) $DyScO_3$ substrates. For PLD, a substrate temperature range of 690-710 ^{o}C was used in an oxygen pressure of 100 mTorr, at a repetition rate of 8 Hz with a laser fluence of 1.1 J/cm^2. After growth, the samples were cooled to room temperature in an O_2 pressure of 750 Torr. The $DyScO_3$ provides a small anisotropic strain to the rhombohedral $BiFeO_3$ resulting in an induced anisotropy in the $BiFeO_3$ domain structure which is composed of two polarization variants. [107, 110] The $SrRuO_3$ layer was deposited as a conducting layer to be

used as a back electrode for the application of vertical electric fields. The surface topography and the ferroelectric domain structure were imaged using atomic force (AFM) and piezoresponse force (PFM) microscopies. The film surface displayed a terraced/stepped like surface topology with an RMS roughness of .2nm ((a)). The in-plane components of the polarizations in each of the two multiferroic domain variants are shown in ((b)). The polarizations in each domain have the same out-of-plane component (not shown), pointing down into $SrRuO_3$ layer, while the in-plane components are 90^o separated, forming a quasi-periodic structure.

6.2.2 Details of $Co_{.90}Fe_{.10}$ / Cu / $Co_{.90}Fe_{.10}$ / Pt multilayer growth

The domain anisotropy in the multiferroic can be induced in an exchange coupled $Co_{.90}Fe_{.10}$ layer through coupling to the weak ferromagnetic moment in each domain of the $BiFeO_3$. [128, 50] This coupling results in a one-to-one mapping of the induced ferromagnetic domains in $Co_{.90}Fe_{.10}$ and the domains of the multiferroic $BiFeO_3$, leading to a macroscopic easy axis that is parallel to P_{netIP}. [128, 50] After the $BiFeO_3$ films were grown, they were immediately inserted into a vacuum sputtering chamber with a base pressure of $3x10^{-8}$ Torr. Spin valve devices in the sequence of $Co_{.90}Fe_{.10}$ (2.3nm)/ Cu (4-7nm)/ $Co_{.90}Fe_{.10}$ (2.5nm)/ Pt (2.5nm) are deposited by DC magnetron sputtering onto the $BiFeO_3$ films at room temperature in a argon background of $8x10^{-4}$ Torr. The $Co_{.90}Fe_{.10}$ layers are deposited under a 200 Oe growth field that is oriented along the direction of P_{netIP}. The growth field is used to induce a magnetic easy axis in the free layer that is parallel to the magnetic easy axis of the pinned layer in contact with $BiFeO_3$. The device is capped with Pt (2.5 nm) to prevent oxidation of the other layers.

6.2.3 Definition of the device

The metallic multilayers are then patterned into a bit the areal size of 2x6 μm^2 using photolithography and argon ion milling. The bits are defined by etching the surrounding metallic layers down to the underlying $BiFeO_3$ film. Then, electrical contact is made to the bit with Cu/Pt contacts for current in-plane measurements (CIP) using a photolithographic liftoff process. The schematic presented in Figure 6.3 illustrates the completed multiferroic-spin valve device architecture, showing that the voltage is applied through the thickness of the multiferroic layer and the resistance measurement of the spin valve device is in-plane.

6.2.4 Resistance measurements

Resistance measurements were configured in a simple two wire geometry using a keithely 220 current source and a keithely 181 nanovoltmeter. Typical device re-

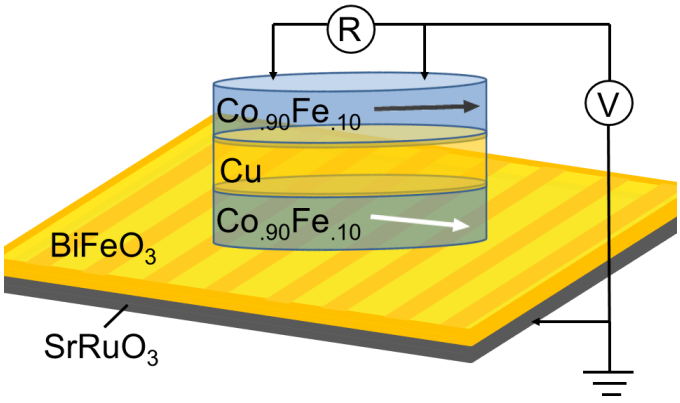

Figure 6.3: Schematic of the multiferroic - spin valve device. The voltage is applied through the film thickness of the $BiFeO_3$ film. The two wire resistance measurement of the spin valve device is oriented such that the current is applied into the plane of the spin valve interfaces (CIP).

sistances were between 10 and 60 ohms and displayed linear I(V) curves within our applied current range (1μA - 20μA). This measurement system allows for the flexibilty to measure the device resistance as the device is rotated in a constant magnetic field or to measure the device resistance as the magnetic field is swept keeping the angle of the sample with respect to the applied magnetic field constant.

6.3 Experimental results and discussion

6.3.1 Device characterization: magnetotransport

The devices were found to have a maximum giant magnetoresistance ratio (GMR) between 1 % and 3 %. Typical magnetoresistance (MR) data for these devices is shown in Figure 6.4. The purple open circles show the data going from positive to negative magnetic field while the red open circles are the data going from negative to positive magnetic field. Going from positive to negative, the free layer (2.5nm $Co_{.90}Fe_{.10}$) switches first, creating a rise in the resistance until the resistance reaches a saturation value. Upon decreasing the magnetic field further, the magnetic layer in contact with $BiFeO_3$ switches due to its enhanced magnetic anisotropy from the exchange coupling, resulting in a decrease in the device resistance.

To confirm the induced uniaxial anisotropies, angular dependent MR curves were taken. In Figure 6.5, the MR curves taken as the applied magnetic field is angled away from the direction of the growth field (net in-plane polarization) direction are

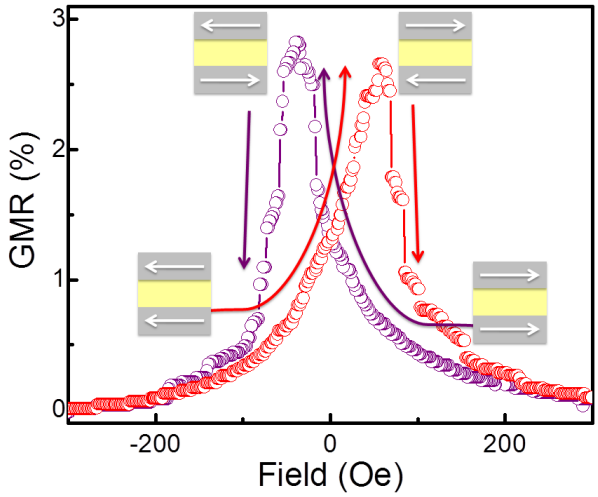

Figure 6.4: Example of a typical magnetoresistance hysteresis curve found in these devices when the magnetic field is oriented along the easy axis of the magnetic layers. Schematics in the graph indicate the orientations of the magnetizations in the top and bottom magnetic layers as the field is cycled. Note that the bottom layer is in contact with the $BiFeO_3$ surface.

shown. Along the growth field direction (0^o) there are two sharp switches indicative of the easy axis for both layers. The resistance saturates very clearly indicating that the true antiparallel state has been reached.

90^o from the growth direction gives a MR curve that well represents a hard axis for both layers. The change in resistance is quite smooth with the peak resistance at $H = 0$ (in one direction) and the $H = 0$ axis serving as an axis of symmetry confirming that this axis is the hard direction for both magnetic layers.

Rotating 180^o from the growth direction yields a MR curve that is very sharp and that quite closely resembles the curve taken at 0^o. The symmetry in the magnetic hysteresis with a 180^o rotation indicates that the two layers have uniaxial anisotropy and confirms our expectation of the device's magnetic anisotropy considering the direction of the growth field and the anisotropy direction imposed by the $BiFeO_3$.

Due to the size of the magnets and the induced domain structure in the pinned layer from the $BiFeO_3$, the relevant resistance states of our multidomain device deviate from conventional parallel and antiparallel resistance states and so a description of the MR curve with respect to the domain structure of the two layers is deserved (see Figure 6.6). Following the purple curve, at high positive field (numbered 1) both saturated magnetizations are parallel and thus the device resistance is low. As the field is decreased to $H = 0$, the resistance begins to increase due to the formation of domains in the layer exchange coupled to $BiFeO_3$ (numbered 2). Domain formation in the free layer at zero field is expected to be small due to the high remnant magnetization of

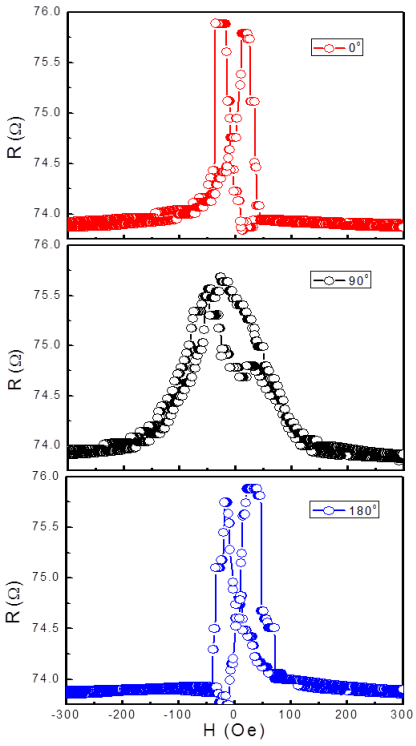

Figure 6.5: Magnetoresistance curves of an as-grown device illustrating the uniaxial magnetic anisotropy of both magnetic layers. 0^o indicates the direction of the applied magnetic field during the growth of the magnetic layers (and net in-plane polarization direction in the as-grown state) which coincides with the magnetic easy axes of the magnetic layers.

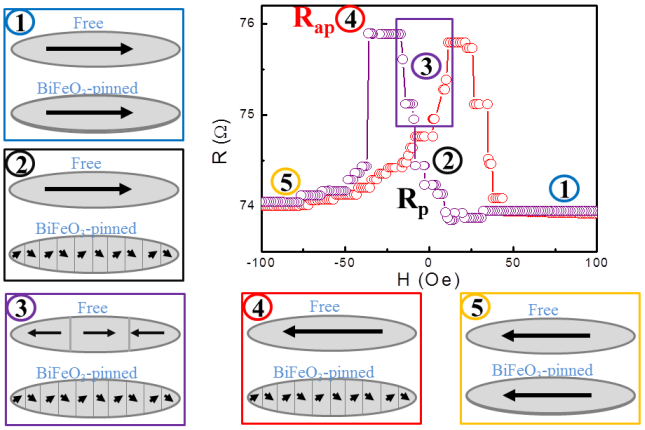

Figure 6.6: A description of the magnetoresistance hysteresis curve found in these devices with respect to the domain structure of the two magnetic layers. The numbers in the graph refer to the schematics which illustrate the domain structure and magnetization directions of the top and bottom magnetic layers as the field is swept from positive to negative values. Note that the bottom layer is in contact with the $BiFeO_3$ surface and has the quasi-periodic striped magnetic domain pattern. Also note that R_p and R_{ap} are defined by states 2 and 4.

our unpinned $Co_{.90}Fe_{.10}$, as seen in Figure 1.11. This state, the R(H = 0) state, is what we refer to as the R_p state, where the essentially saturated free layer is parallel to the net magnetization of the pinned layer but to neither of the 2 magnetization variants in the pinned layer.

As the magnetic field is decreased further, the free layer switches first due to its low anisotropy. As the free layer switches around 12 Oe (there is a sharp increase in resistance), domains form in the free layer, increasing the overall resistance. This region is labeled 3 in the figure and is enclosed by the purple box. The resistance increases until a saturation resistance value is reached due to the magnetization saturation of the free layer. We refer to this resistance state as R_{ap}. While the free layer is saturated, the layer pinned to $BiFeO_3$ is still in a quasi-periodic domain pattern with the net magnetization pointing in the positive field direction. As the magnetic field is decreased further, the magnetic layer in contact with $BiFeO_3$ switches at significantly higher field (typical coercivity in the range of 40-90 Oe) due to its enhanced magnetic anisotropy from the exchange coupling. At higher negative magnetic field, both magnetizations are truly parallel once again and the lowest device resistance is reached. A similar sequence follows when increasing the magnetic field from this state back to high positive field.

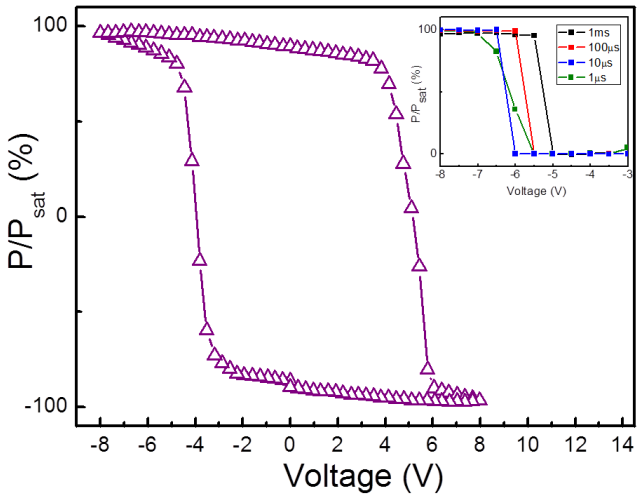

Figure 6.7: Typical ferroelectric hysteresis loop from a $BiFeO_3$-spin valve device structure. Inset: Electric pulse width dependence of the ferroelectric switching.

6.3.2 Device characterization: ferroelectricity

Now that the magnetic device is fully characterized, we are set to determine the electrical switching properties of the multiferroic $BiFeO_3$ in our device. In Figure 6.7, a typical ferroelectric hysteresis loop from these devices is presented. The ferroelectric switching was typically found to have coercivities between 4-9 V depending on film thickness and the duration of the voltage pulse (see inset). The loops show ferroelectric saturation with negligible leakage current. Now that we have seen that both individual ferroic components (magnetic and ferroelectric) operate independently, we are now set to demonstrate their coupling.

6.3.3 Electric field control of spin valve resistance state

In the previous chapter, I have shown that the net magnetization of a $Co_{.90}Fe_{.10}$ layer coupled to $BiFeO_3$ can be reversed with the application of a small out-of-plane voltage. Here I have added additional layers ($Cu/Co_{.90}Fe_{.10}/Pt$) on top of the exchange coupled $Co_{.90}Fe_{.10}$ layer to form a spin-valve structure where the electrical control the exchange coupled $Co_{.90}Fe_{.10}$ layer with out-of-plane voltages to the $BiFeO_3$ is expected. Advantages to this approach reside in the fact that the magnetization state of the bottom layer can be read out without the application of a magnetic field (required for AMR) and the writing voltage is greatly reduced (from 70V to 7V). To begin our study of the electrical control of the resistance state of a spin valve device, the state of the device is prepared by running a MR measurement along the easy axis of the device, which simultaneously tells us the resistance values of the R_p and R_{ap} resistance states (see right plot of Figure 6.8). After finishing the scan at high,

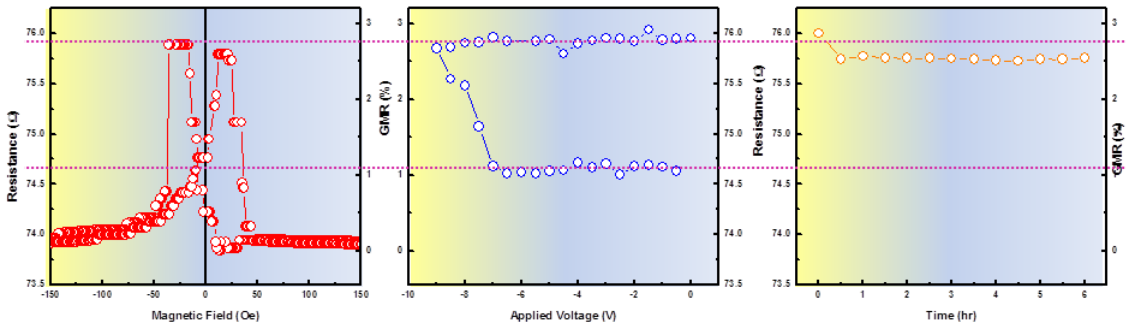

Figure 6.8: Magnetoresistance curve in the as-grown state when the applied field is oriented along the easy axis of the device (left) and a plot of the device resistance as a function of the amplitude of a 1μs voltage pulses (middle). (right) The device resistance as a function of time after electrically poling it into the R_{ap} resistance state. The dashed purple lines are guides to the eye.

positive magnetic field, the magnetic field is set to zero. The resistance of the device is then measured after a 1μs voltage pulse is applied to the $BiFeO_3$ (middle - Figure 6.8). A schematic of the R(V) measurement used to obtain the data in Figure 6.8 is shown in Figure 6.9. The voltage pulses start from zero amplitude and decrease to -9V. From V = 0 to V = -7V the resistance of the device is roughly constant at the value of R_p (use purple dashed line as a guide to the eye). The resistance of the device begins to increase as the voltage amplitude is decreased further. By -9V the resistance has reached the R_{ap} resistance value, revealing that one of the two magnetizations has reversed. The R_{ap} resistance state after switching is stable upon pulsing with negative voltages back to V = 0.

For memory applications, a non-volatile memory bit is highly desired so that the data can be accessed after long periods of time. That is to say, since $BiFeO_3$ is a magnetoelectric multiferroic with stable, electrically switchable states [53], and if the $Co_{.90}Fe_{.10}$ is coupled to the canted moment in each domain, then we expect any electrical control of the coupled ferromagnet to be non-volatile. To illustrate the non-volatility of the switch, the stability of the R_{ap} resistance state after switching was measured over long periods (right panel). The device is stable in this state under H = 0 Oe for a measurement period of 6hrs. In other devices the stability has been measured for more than 12 hrs. This clearly illustrates the non-volatile nature of the electrical switching of our device.

Now that the spin valve resistance state can be switched with an electric field, it must be verified that it is indeed the layer that is in contact with the $BiFeO_3$ that

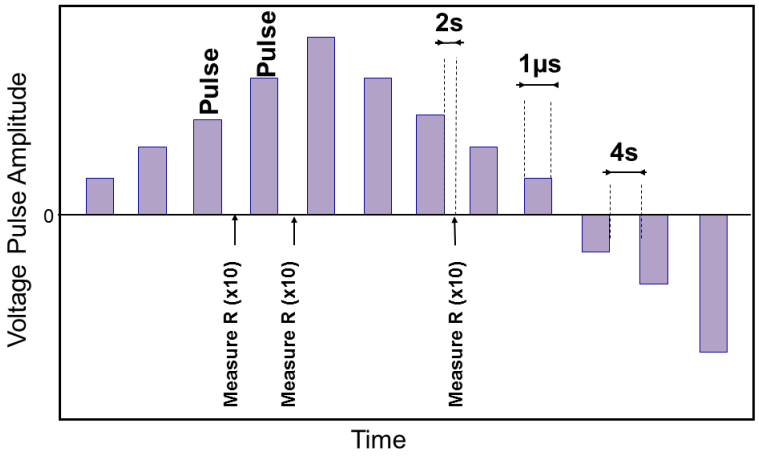

Figure 6.9: Schematic of the measurement-pulse sequence used to obtain the data in Figure 6.8.

is undergoing the electric field induced reversal. To investigate this, a sample with similar characteristics to the sample shown in Figure 6.8 was prepared. In Figure 6.10, the state of this sample in the as-grown state is swept from H = 0 to H = 200 Oe and back to H = 0 while measuring the resistance of the device (open black triangles in the figure). After the measurement of the as-grown state, the sample is pulsed with -7V at H = 0. The data after the voltage pulse is shown in the open orange triangles. The initial resistance at H = 0 has increased from the as-grown value to a R_{ap} value. As the field is increased, there is a switching to the low resistance state near 80 Oe, the coercive field of the bottom $Co_{.90}Fe_{.10}$ layer in contact with $BiFeO_3$. This clearly reveals that the layer in contact with the $BiFeO_3$ layer is the magnetization that is electrically reversed.

Now that we have shown that the bottom layer is the layer that is electrically controlled, presented in Figure 6.11 is a completed resistance versus voltage loop (open red circles) along with the ferroelectric loop (open violet triangles) to correlate the multiferroic switching events to the switching events in the spin valve resistance. The measurement scheme of this magnetoelectric device is the same as that present in Figure 6.9. The loop begins at V = 0 and decreases to -7V where the voltage then starts to increase to complete the hysteresis cycle. There is a clear correlation between the ferroelectric switching of the multiferroic and the switching between the R_p and R_{ap} resistance states. The slight voltage asymmetry in the ferroelectric loop (1V shift) is closely mimicked by the device resistance. The switching fields for the ferroelectric and resistance states are clearly correlated (V_c = -4V and 5V while for

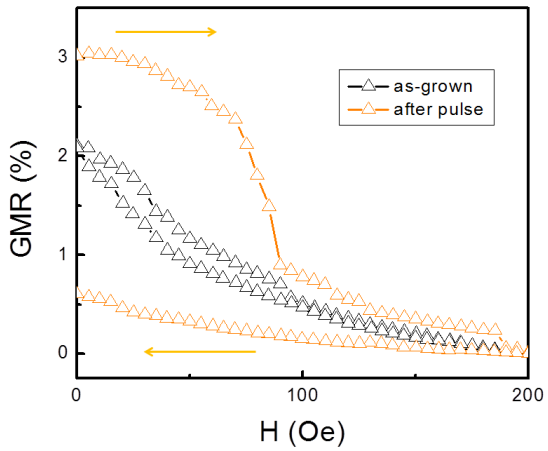

Figure 6.10: Magnetoresistance curves taken (from a sample similar to the one shown in Figure 6.8) along the easy axis of the as-grown (open black triangles) and electrically switched (open orange triangles) states by sweeping the magnetic field from 0 Oe to 200 Oe and back to 0 Oe (orange arrows associate resistances with the field sweep). The sharp switching around 80 Oe in the switched curve indicates that the layer in contact with $BiFeO_3$ is the one that reorients due to the applied voltage.

the device R_c = -3.5V and 4.5V). The loop closes with a small gap between the initial and final resistance states, which may be due to a lack of saturation on the positive side of the loop and thus the lowest resistance state may have not been reached. This loop is a clear demonstration of an operational magnetoelectric multiferroic memory bit at room temperature.

Figure 6.12(a) shows the measured ferroelectric loop from another device and is plotted with the resistance of the spin valve as the voltage is pulsed. Again, a clear correlation of the switching voltages is illustrated. Additionally, the magnetoresistance of the device is plotted to the right to correlate the resistance states of the R(V) loops to the magnetic state of the device. The device is switched between R_p and R_{ap} states. Figure 6.12(b) shows the cycling of the device and the measurement sequence used with the application of +,- 8V.

6.4 Discussion: Energy consumption

Since the motive of combining multiferroics and spintronics research has been to find low energy solutions for spintronics applications, the energy consumption of this primitive device is quantified. Furthermore, I compare the energy loss to that of the spin transfer torque (STT) method of reversal because of its advantages over other methods of data storage, such as high speed, high density, high endurance, low

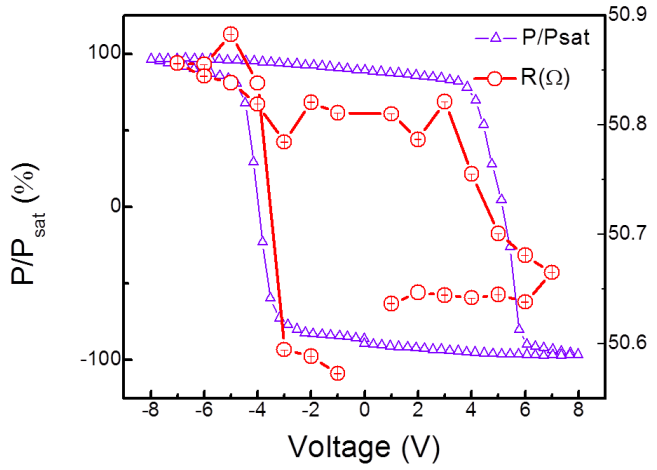

Figure 6.11: Complete hysteresis of the device resistance obtained at room temperature as the amplitude of a 1μs voltage pulse is cycled while under zero magnetic field.

energy dissipation and non-volatility. At this time, the state of the art STT device requires 49μA of current through a 40nm diameter device (9.7x10^5 A/cm^2) which lead to an energy dissipation per unit area of 3mJ/cm^2. [149] If we consider the average switching voltage of our devices to be 4.5V, the energy lost in our device is (4.5V)100μC/cm^2 = .450mJ/cm^2, roughly an order of magnitude lower than an optimized spin torque device. Futhermore, our primitive memory has the traditional advantages of magnetic memory, such as non-volatility and low reading energy.

It is noted that our energy consumption can be decreased easily through fine control of $BiFeO_3$ film quality leading to thinner $BiFeO_3$ thicknesses and reduced switching voltages. [150] Furthermore, doping to reduce the ferroelectric coercivity and polarization of $BiFeO_3$ will further reduce the switching voltage and energy consumption. [151] While our device is still in its primitive stages, the fact that the writing is done by the multiferroic and is then essientially governed by a ferroelectric switch, the switching speed can be as fast as 100ps but has yet to be determined in these devices. If the switch could be done at these time scales, ultra-low power devices could be demonstrated.

6.5 Concluding remarks and outlook

$BiFeO_3$ has long been proposed to influence traditional spintronic devices due to its high temperature magnetoelectric-multiferroic properties. Barriers hindering this impact have been driven by the desire to control the magnetization through the control of exchange bias, which is caused by metastable 109^o domain walls. [145, 152, 153]

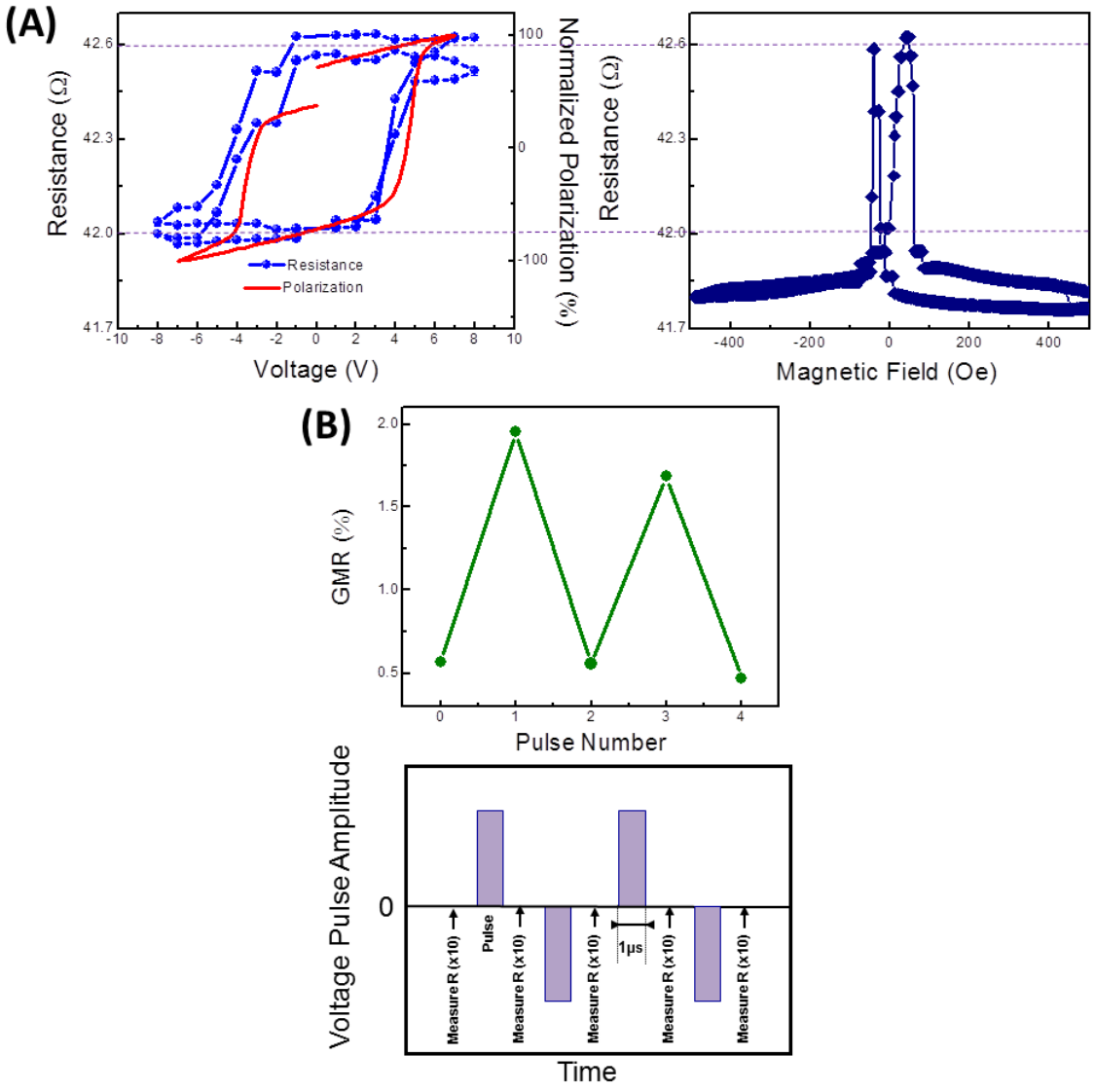

Figure 6.12: (a) Complete hysteresis of the device resistance obtained at room temperature as the amplitude of a 1μs voltage pulse is cycled while under zero magnetic field. The red line represents the ferroelectric loop of the device. To correlate the resistance states in the R(V) loop to the magnetic configuration of the device, the magnetoresistance of the device is also plotted. (b) Multiple switching cycles are shown in the green plot. Below is the schematic of the cycling measurement using +,- 8V.

Here I have demonstrated the ability to reversibly control the resistance state of a GMR structure solely with a small voltage pulse. By exploiting the magnetic coupling between a ferromagnetic layer and the magnetoelectric multiferroic $BiFeO_3$, which is driven by an intrinsic mechanism (coupling to the $BiFeO_3$'s canted moment in each domain), a magnetization of a ferromagnet is controllably reversed in this traditional spintronic device with soley an applied electric field. Only voltage pulses of relatively small amplitudes (4-9V) are required to control the resistance state when the voltage is applied across the thickness of the $BiFeO_3$ film. This non-volatile electrical switching between R_p and R_{ap} resistance states, using only small currents for reading and voltage for writing, demonstrates a low energy dissipation memory. These latter points make this magnetoelectric memory architecture more advantageous, in the energy dissipation basis, for industrial applications than piezo- and current driven approaches.

At this time, the state of the art STT device requires 49μA of current through a 40nm diameter device ($9.7x10^5$ A/cm^2), which leads to an energy dissipation per unit area of 3mJ/cm^2. [149] Considering the average switching voltage of our devices to be 4.5V, the energy lost in our device is $(4.5V)100\mu C/cm^2 = .450mJ/cm^2$, roughly an order of magnitude lower than an optimized spin torque device. Our device the first clear demonstration where $BiFeO_3$ has been intergrated into a spintronic device without the loss of magnetic capability. Futhermore, it has been demonstrated that our primitive memory has the traditional advantages of magnetic memory such as non-volatility and low reading energy.

Transitioning fundamental discoveries to real products is a monumental challenge due to the growing number of processing and financial obstacles. While there is still a long road to travel before such a magnetoelectric device will impact magnetic technology, this work already illustrates its potential from the following viewpoint. As we discussed, our approach is already more energy effiecient than current based approaches, however, for the further advancement of this approach several issues remain which must be tackled.

1. **Switching below 1V:** It's clear that the future steps must be to show that the magnetization can be reversed below 1V via an out-of-plane electric field. This can theoretically be achieved through the control of the $BiFeO_3$ film quality and thickness. Additionally, the chemical doping of 10-15 percent La reduces the ferroelectric polarization and the switching voltage of $BiFeO_3$ films. Bringing these together can lead to the lower switching voltages and lower energy consumption magnetic switching.

2. **Robustness-$BiFeO_3$ quality and interface cleanliness:** Earlier it was shown that the magnetization can be reversed with the polarization reversal. Many cycles of such an observed magnetization reversal are needed to impact technology and lead to an insight of the physical mechanism driving such a

reversal. Issues of the robustness in these devices can come from $BiFeO_3$ and back electrode quality (leakage, ferroelectric imprint). Ferroelectric/metal interfaces have plagued industrial applications due to the trapping of defects at the Ferroelectric/metal interface causing internal electric fields that freeze the polarization. Optimization of the $BiFeO_3$ to reduce defect related issues. Additionally, the quality of the $BiFeO_3/Co_{.90}Fe_{.10}$ is to be considered. Ideally, high quality $BiFeO_3$ and $Co_{.90}Fe_{.10}$ layers would be deposited in-situ to keep the interface free from atmospheric conditions and hydrocarbons.

Chapter 7

Conclusion and future directions

Our ever increasing consumption of energy (and other resources) has led to situations of unmet demand and raised awareness of conservation practices to protect our global resources. At the same time, there is an ever increasing need for information, leading to the push for faster technology with a larger information storage capacity. Spintronics has emerged as a flourishing field of theoretical and experimental research that is, at its core level, focused on meeting these technological and energy demands by integrating additional functionalities into electronic devices through the electron's other degree of freedom: the spin. While this field has made a significant impact on technology over the past 20 years, the largest has been in the sectors of memory and sensing (both RAM, hard disk, and read heads). Currently these technologies have been bottle necked by issues of scalability and energy dissipation due to the current needed to generate external magnetic fields. Advances, such as the discovery of the spin transfer torque, have improved device scalability but still suffer because the device operation requires large currents. This leads to a large energy waste and a host of material degradation issues. The ideal approach to this dual-fold problem is to use electric fields rather than electrical currents. Such a control of magnetism has, therefore, aroused significant interest in recent years and has led to the revival of multiferroics research. Thus, in this dissertation it was my effort to explore room temperature magnetoelectric multiferroic oxides and heterostructures as a means to overcome the issues faced by modern spintronic technologies. Furthermore, this dissertation presents the demonstration of the electrically induced bistable magnetization switching at room temperature − a necessary requirement for magnetic data storage − and the demonstration of a magnetoelectric memory.

There are two crucial aspects to researching the electric field control of magnetism using heterostructures with multiferroics. Those are the investigation of the heterointerface and multiferroic itself (magnetoelectric switching events, direction of multiferroic parameters, strain effects, etc). Here, the interface exchange coupling mechanism via the manifestations in the magnetic domain structure and magnetic anisotropy of a $Co_{.90}Fe_{.10}$ in contact with an epitaxially strain engineered multiferroic

$BiFeO_3$ layer. I have highlighted the importance of the epitaxial constraints on the domain structure of the multiferroic layer due to its transferability to an exchange coupled ferromagnetic layer. The observation of the one-to-one domain correlation between the multiferroic and the ferromagnet has allowed for the interface exchange coupling mechanism, the direction of the magnetic order parameters, and the magnetoelectric switching events of the multiferroic $BiFeO_3$ to be determined. Using a combination of XMCD, XMLD, and PFM, the one-to-one domain correlation was used to show that $Co_{.90}Fe_{.10}$ moment couples to the weak ferromagnetic moment of $BiFeO_3$ whereby then the $Co_{.90}Fe_{.10}$ essentally acts as a spin amplifier of the multiferroic's weak ferromagnetic moment.

The design and fabrication of a simple magnetoelectric device that uses this effective amplification to reveal the magnetoelectric switching events in $BiFeO_3$ due to applied in-plane and out-of-plane electric fields was illustrated. Furthermore, the technological appeal of these investigations is highlighted by the fact that no applied magnetic field is needed to control the ferromagnet. The feromagnetic magnetization can be reversibly cycled and, in the case of the out-of-plane switching, only requires a small voltage. Finally, I ended with the demonstration of a true low-energy magnetoelectric device where both the read and write processes were done electrically and without an applied magnetic field. In essence, the progress in the field of $BiFeO_3$ from the view point of the electrical control of magnetism has been reviewed. It is my hope that this thesis has captured all of the excitement, fascinating ideas, and nuances that have been used recently in this pursuit and have highlighted its viability to impact technology.

Transitioning fundamental discoveries to real products is a monumental challenge due to the growing number of processing and financial obstacles. As a testament to the achievement of becoming an industry technology, spin torque still faces functional issues that are hindering a strong adoption of the technology despite its ten year tenure. While there is still a long road to travel before multiferroics will impact magnetic technologies, the work presented in this thesis has illustrated their potential impact from two viewpoints. 1) The ability to reverse a magnetization with an applied electric field has been questioned from symmetry considerations. Here it was shown that multiferroics have the capability of reversing a magnetization with an applied electric field at both macroscopic and microscopic scales. 2) A magnetization can be reversed in a single or multilayer device with an applied single digit voltage. The energy dissipation is assumed to come from the ferroelectric hysteresis and, therefore, in this magnetoelectric device structure the energy loss is roughly $.45 mJ/cm^2$, roughly an order of magnitude lower than spin torque.

With these studies setting the stage, there are several interesting research endeavors and issues that can be pursued from both scientific and applications perspectives. Such endeavors are presented here for the direction of future efforts.

1. **Tuning the spin-orbit interaction in $BiFeO_3$:** As I have discussed throughout this dissertation, the pathways to the electrical control of magnetism involve some

manifestation of the spin-orbit interaction. In $BiFeO_3$, the Dzyaloshinskii-Moriya interation is the spin-orbit interaction that links the macroscopic charge order to the macroscopic spin order. There have been attempts to influence the magnetic order and the degree of spin canting in $BiFeO_3$ through chemical doping (i.e. Mn incorporation). [154] There have been no attempts to strengthen the spin-orbit interation and the magnetoelectric coupling in this room temperature magnetoelectric multiferroic. It seems that doping the B site with heavy elements which have partially filled d or f shells could strengthen the spin-orbit interaction while still providing spins for enhanced magnetic interactions. Possible elements could be Gd, Ir, Eu and Sm.

2. **Dynamics:** The speed of the electrical switching of the magnetization is a critical experiment for the understanding of the physical mechanisms of the reversal and the determination the technological viability of the electrical control. Of course, the speed of the writing is critical, most especially in RAM applications where the information is called quickly. In the case of spin transfer torque, the switching of the magnetization can be done in the range of 1-.1ns. The switching of ferroelectrics due to an applied electric field can also be in this range. As it was described in the simulations of the in-plane ferroelectric switching of $BiFeO_3$ for the in-plane magnetoelectric device structure, the switch has a 'relaxation' like component. The time scale of relaxive switching can be much longer, even up to seconds in cases. Clearly then, the speed of the switch will reveal the rate limiting step in the observed reversal and indicate the the magnetoelectric switching mechanism in $BiFeO_3$ by which the magnetization is reversed. That is to say, is the reversal due to the sharp switch from the applied electric field or some kind of slow relaxation switching?

3. **Device size and the single domain switching:** Areal space in modern memory is precious realestate and memory bits on the order of microns are far too large. To have an impact on technology, the devices will need to be decreased into the 100-10nm range. Shrinking the device down to this size does a couple things. The magnets at this scale are monodomain and hence there is no convolution from multidomain state in the magnetoeresistance. Also the magnetic bits can then fit into a single $BiFeO_3$ domain. These two facts allow for experiments that investigate the magnetic coupling between the ferromagnet and the multiferroic within an individual multiferroic domain and the switching processes that happen at the single domain scale.

4. **Futher reduction of the energy and voltage requirements:** While the control of a magnetization with a mere 4-7 volts was shown, this value is still considered to be large in the microelectronics industry. More importantly, there are pathways to reduce this switching voltage further, while opening up some interesting multiferroic materials questions. Previous reports on the substitution of 10 percent La can reduce the remnant polarization and coercive field of the $BiFeO_3$. [151] The questions are whether the magnetoelectric properties and the coupling with the ferromagnet are similar enough to the undoped case such that the observed magnetization reversal is still possible.

5. **Long term reliability:** While reversibilty was shown throughout this work, issues of long term device reliability (switching greater than 10^9 cycles) still remain. Issues of imprint, $BiFeO_3$ and $BiFeO_3/Co_{.90}Fe_{.10}$ quality are areas that can be the focus for improved device performance. Such a research endeavor should focus on the growth of $BiFeO_3$ and $Co_{.90}Fe_{.10}$ in situ for the highest quality interface.

Listed above are just a few of the unexplored questions regarding the magnetoelectric nature of multiferroic complex oxides and many others exist. As these posed questions are answered, new questions will undoubtedly arise. The pursuit to the answers of such questions is a worthy quest. I believe that answering such questions is relevant to both a fundamental understanding of magnetoelectric multiferroics as well as to the applications of low-energy spintronics.

Bibliography

[1] JW FORRESTER. DIGITAL INFORMATION STORAGE IN 3 DIMENSIONS USING MAGNETIC CORES. *JOURNAL OF APPLIED PHYSICS*, 22(1):44–48, 1951.

[2] Joachim Stohr and Hans Christoph Siegmann. Magnetism : From Fundamentals to Nanoscale Dynamics. *Springer*, ():826, 2006.

[3] D. C. Ralph and M. D. Stiles. Spin transfer torques. *JOURNAL OF MAGNETISM AND MAGNETIC MATERIALS*, 320(7):1190–1216, APR 2008.

[4] JC Slonczewski. Current-driven excitation of magnetic multilayers. *JOURNAL OF MAGNETISM AND MAGNETIC MATERIALS*, 159(1-2):L1–L7, JUN 1996.

[5] T. Kawahara, K. Ito, R. Takemura, and H. Ohno. Spin-transfer torque RAM technology: Review and prospect. *MICROELECTRONICS RELIABILITY*, 52(4):613–627, APR 2012.

[6] JG BEDNORZ and KA MULLER. POSSIBLE HIGH-TC SUPERCONDUCTIVITY IN THE BA-LA-CU-O SYSTEM. *ZEITSCHRIFT FUR PHYSIK B-CONDENSED MATTER*, 64(2):189–193, 1986.

[7] M Imada, A Fujimori, and Y Tokura. Metal-insulator transitions. *REVIEWS OF MODERN PHYSICS*, 70(4, Part 1):1039–1263, OCT 1998.

[8] S JIN, TH TIEFEL, M MCCORMACK, RA FASTNACHT, R RAMESH, and LH CHEN. THOUSANDFOLD CHANGE IN RESISTIVITY IN MAGNETORESISTIVE LA-CA-MN-O FILMS. *SCIENCE*, 264(5157):413–415, APR 15 1994.

[9] A.P. Ramirez. Colossal magnetoresistance. *JOURNAL OF PHYSICS-CONDENSED MATTER*, 9(39):8171–8199, SEP 29 1997.

[10] Pu Yu. Emergent Phenomena at Complex Oxide Interfaces. *Thesis, University of California, Berkeley*, ():1–3, Spring 2011.

[11] A Ohtomo and HY Hwang. A high-mobility electron gas at the LaAlO3/SrTiO3 heterointerface. *NATURE*, 427(6973):423–426, JAN 29 2004.

[12] K. F. Wang, J. M. Liu, and Z. F. Ren. Multiferroicity: the coupling between magnetic and polarization orders. *ADVANCES IN PHYSICS*, 58(4):321–448, 2009.

[13] R. Ramesh and Nicola A. Spaldin. Multiferroics: progress and prospects in thin films. *NATURE MATERIALS*, 6(1):21–29, JAN 2007.

[14] Sang-Wook Cheong and Maxim Mostovoy. Multiferroics: a magnetic twist for ferroelectricity. *NATURE MATERIALS*, 6(1):13–20, JAN 2007.

[15] Hans Schmid. Some symmetry aspects of ferroics and single phase multiferroics. *JOURNAL OF PHYSICS-CONDENSED MATTER*, 20(43), OCT 29 2008.

[16] N Hur, S Park, PA Sharma, JS Ahn, S Guha, and SW Cheong. Electric polarization reversal and memory in a multiferroic material induced by magnetic fields. *NATURE*, 429(6990):392–395, MAY 27 2004.

[17] P. Curie. *J. Physique*, 3:393, 1894.

[18] D. N. Astov. *Sov. Phys.-JETP*, 11:708, 1960.

[19] D. N. Astov. *Sov. Phys.-JETP*, 13:729, 1961.

[20] GT RADO and VJ FOLEN. OBSERVATION OF MAGNETICALLY INDUCED MAGNETOELECTRIC EFFECT AND EVIDENCE FOR ANTIFERROMAGNETIC DOMAINS. *PHYSICAL REVIEW LETTERS*, 7(8):310–&, 1961.

[21] VJ FOLEN, GT RADO, and EW STALDER. ANISOTROPY OF MAGNETOELECTRIC EFFECT IN CR2O3. *PHYSICAL REVIEW LETTERS*, 6(11):607–&, 1961.

[22] GT RADO. MECHANISM OF MAGNETOELECTRIC EFFECT IN AN ANTIFERROMAGNET. *PHYSICAL REVIEW LETTERS*, 6(11):609–&, 1961.

[23] M Fiebig. Revival of the magnetoelectric effect. *Journal of Physics D-Applied Physics*, 38(8):R123–R152, APR 21 2005.

[24] Nicola A. Spaldin and R. Ramesh. Electric-Field Control of Magnetism in Complex Oxide Thin Films. *MRS BULLETIN*, 33(11):1047–1050, NOV 2008.

[25] JY Zhai, ZP Xing, SX Dong, JF Li, and D Viehland. Detection of pico-Tesla magnetic fields using magneto-electric sensors at room temperature. *APPLIED PHYSICS LETTERS*, 88(6), FEB 6 2006.

[26] SX Dong, JF Li, and D Viehland. Vortex magnetic field sensor based on ring-type magnetoelectric laminate. *APPLIED PHYSICS LETTERS*, 85(12):2307–2309, SEP 20 2004.

[27] SX Dong, JF Li, and D Viehland. Circumferentially magnetized and circumferentially polarized magnetostrictive/piezoelectric laminated rings. *JOURNAL OF APPLIED PHYSICS*, 96(6):3382–3387, SEP 15 2004.

[28] SX Dong, JG Bai, JY Zhai, JF Li, GQ Lu, D Viehland, SJ Zhang, and TR Shrout. Circumferential-mode, quasi-ring-type, manetoelectric laminate composite - a highly sensitive electric current and/or vortex magnetic field sensor. *APPLIED PHYSICS LETTERS*, 86(18), MAY 2 2005.

[29] SX Dong, JF Li, D Viehland, J Cheng, and LE Cross. A strong magnetoelectric voltage gain effect in magnetostrictive-piezoelectric composite. *APPLIED PHYSICS LETTERS*, 85(16):3534–3536, OCT 18 2004.

[30] SX Dong, JF Li, and D Viehland. Voltage gain effect in a ring-type magnetoelectric laminate. *APPLIED PHYSICS LETTERS*, 84(21):4188–4190, MAY 24 2004.

[31] Shuxiang Dong, Junyi Zhai, J. F. Li, D. Viehland, and M. I. Bichurin. Magnetoelectric gyration effect in Tb1-xDyxFe2-y/Pb(Zr,Ti)O-3 laminated composites at the electromechanical resonance. *APPLIED PHYSICS LETTERS*, 89(24), DEC 11 2006.

[32] Junyi Zhai, Jiefang Li, Shuxiang Dong, D. Viehland, and M. I. Bichurin. A quasi(unidirectional) Tellegen gyrator. *JOURNAL OF APPLIED PHYSICS*, 100(12), DEC 15 2006.

[33] Z. Huang. Theoretical modeling on the magnetization by electric field through product property. *JOURNAL OF APPLIED PHYSICS*, 100(11), DEC 1 2006.

[34] MI Bichurin, IA Kornev, VM Petrov, AS Tatarenko, YV Kiliba, and G Srinivasan. Theory of magnetoelectric effects at microwave frequencies in a piezoelectric/magnetostrictive multilayer composite. *PHYSICAL REVIEW B*, 64(9), SEP 1 2001.

[35] RR BIRSS and SHRUBSAL.RG. PROPAGATION OF ELECTROMAGNETIC WAVES IN MAGNETOELECTRIC CRYSTALS. *PHILOSOPHICAL MAGAZINE*, 15(136):687–&, 1967.

[36] Ce-Wen Nan, M. I. Bichurin, Shuxiang Dong, D. Viehland, and G. Srinivasan. Multiferroic magnetoelectric composites: Historical perspective, status, and future directions. *Journal of Applied Physics*, 103(3), FEB 1 2008.

[37] J Wang, JB Neaton, H Zheng, V Nagarajan, SB Ogale, B Liu, D Viehland, V Vaithyanathan, DG Schlom, UV Waghmare, NA Spaldin, KM Rabe, M Wuttig, and R Ramesh. Epitaxial BiFeO3 multiferroic thin film heterostructures. *SCIENCE*, 299(5613):1719–1722, MAR 14 2003.

[38] H Zheng, J Wang, SE Lofland, Z Ma, L Mohaddes-Ardabili, T Zhao, L Salamanca-Riba, SR Shinde, SB Ogale, F Bai, D Viehland, Y Jia, DG Schlom, M Wuttig, A Roytburd, and R Ramesh. Multiferroic BaTiO3-CoFe2O4 nanostructures. *SCIENCE*, 303(5658):661–663, JAN 30 2004.

[39] V. M. Petrov, G. Srinivasan, M. I. Bichurin, and A. Gupta. Theory of magnetoelectric effects in ferrite piezoelectric nanocomposites. *PHYSICAL REVIEW B*, 75(22), JUN 2007.

[40] Manuel Bibes and Agnes Barthelemy. Oxide spintronics. *IEEE TRANSACTIONS ON ELECTRON DEVICES*, 54(5):1003–1023, MAY 2007.

[41] H. Bea, M. Gajek, M. Bibes, and A. Barthelemy. Spintronics with multiferroics. *JOURNAL OF PHYSICS-CONDENSED MATTER*, 20(43), OCT 29 2008.

[42] E ASCHER, H RIEDER, H SCHMID, and H STOSSEL. SOME PROPERTIES OF FERROMAGNETOELECTRIC NICKEL-IODINE BORACITE NI3B7O13I. *JOURNAL OF APPLIED PHYSICS*, 37(3):1404–&, 1966.

[43] D. I. Khomskii. Multiferroics: Different ways to combine magnetism and ferroelectricity. *Journal of Magnetism and Magnetic Materials*, 306(1):1–8, NOV 1 2006.

[44] L. W. Martin and R. Ramesh. Overview No. 151 Multiferroic and magnetoelectric heterostructures. *ACTA MATERIALIA*, 60(6-7):2449–2470, APR 2012.

[45] D. Lebeugle, A. Mougin, M. Viret, D. Colson, J. Allibe, H. Bea, E. Jacquet, C. Deranlot, M. Bibes, and A. Barthelemy. Exchange coupling with the multiferroic compound BiFeO3 in antiferromagnetic multidomain films and single-domain crystals. *PHYSICAL REVIEW B*, 81(13), APR 1 2010.

[46] NA Hill. Why are there so few magnetic ferroelectrics? *JOURNAL OF PHYSICAL CHEMISTRY B*, 104(29):6694–6709, JUL 27 2000.

[47] I DZYALOSHINSKY. A THERMODYNAMIC THEORY OF WEAK FERROMAGNETISM OF ANTIFERROMAGNETICS. *JOURNAL OF PHYSICS AND CHEMISTRY OF SOLIDS*, 4(4):241–255, 1958.

[48] IE DZYALOSHINSKII. THEORY OF HELICOIDAL STRUCTURES IN ANTIFERROMAGNETS .1. NONMETALS. *SOVIET PHYSICS JETP-USSR*, 19(4):960–971, 1964.

[49] T MORIYA. ANISOTROPIC SUPEREXCHANGE INTERACTION AND WEAK FERROMAGNETISM. *PHYSICAL REVIEW*, 120(1):91–98, 1960.

[50] M. Trassin, J. T. Heron, J.D. Clarkson, R. Bowden, D.T. Pierce, J. Unguris, and R. Ramesh. Switching of Dzyaloshinskii - Moriya Vector with an Electric Field. *Science*, ():, In submission 2012.

[51] C Ederer and NA Spaldin. Weak ferromagnetism and magnetoelectric coupling in bismuth ferrite. *PHYSICAL REVIEW B*, 71(6), FEB 2005.

[52] Craig J. Fennie. Ferroelectrically induced weak ferromagnetism by design. *PHYSICAL REVIEW LETTERS*, 100(16), APR 25 2008.

[53] T. Zhao, A. Scholl, F. Zavaliche, K. Lee, M. Barry, A. Doran, M. P. Cruz, Y. H. Chu, C. Ederer, N. A. Spaldin, R. R. Das, D. M. Kim, S. H. Baek, C. B. Eom, and R. Ramesh. Electrical control of antiferromagnetic domains in multiferroic BiFeO3 films at room temperature. *Nature Materials*, 5(10):823–829, OCT 2006.

[54] Ying-Hao Chu, Lane W. Martin, Mikel B. Holcomb, Martin Gajek, Shu-Jen Han, Qing He, Nina Balke, Chan-Ho Yang, Donkoun Lee, Wei Hu, Qian Zhan, Pei-Ling Yang, Arantxa Fraile-Rodriguez, Andreas Scholl, Shan X. Wang, and R. Ramesh. Electric-field control of local ferromagnetism using a magnetoelectric multiferroic. *Nature Materials*, 7(6):478–482, JUN 2008.

[55] B DIENY, VS SPERIOSU, SSP PARKIN, BA GURNEY, DR WILHOIT, and D MAURI. GIANT MAGNETORESISTANCE IN SOFT FERROMAGNETIC MULTILAYERS. *PHYSICAL REVIEW B*, 43(1, Part b):1297–1300, JAN 1 1991.

[56] SSP Parkin, C Kaiser, A Panchula, PM Rice, B Hughes, M Samant, and SH Yang. Giant tunnelling magnetoresistance at room temperature with MgO (100) tunnel barriers. *NATURE MATERIALS*, 3(12):862–867, DEC 2004.

[57] Stuart S. P. Parkin, Masamitsu Hayashi, and Luc Thomas. Magnetic domain-wall racetrack memory. *SCIENCE*, 320(5873):190–194, APR 11 2008.

[58] SSP PARKIN. ORIGIN OF ENHANCED MAGNETORESISTANCE OF MAGNETIC MULTILAYERS - SPIN-DEPENDENT SCATTERING FROM MAGNETIC INTERFACE STATES. *PHYSICAL REVIEW LETTERS*, 71(10):1641–1644, SEP 6 1993.

[59] T VALET and A FERT. THEORY OF THE PERPENDICULAR MAGNETORESISTANCE IN MAGNETIC MULTILAYERS. *PHYSICAL REVIEW B*, 48(10):7099–7113, SEP 1 1993.

[60] PM LEVY, SF ZHANG, and A FERT. ELECTRICAL-CONDUCTIVITY OF MAGNETIC MULTILAYERED STRUCTURES. *PHYSICAL REVIEW LETTERS*, 65(13):1643–1646, SEP 24 1990.

[61] C Binek and B Doudin. Magnetoelectronics with magnetoelectrics. *Journal of Physics-Condensed Matter*, 17:L39–L44, 2005.

[62] Martin Gajek, Manuel Bibes, Stephane Fusil, Karim Bouzehouane, Josep Fontcuberta, Agnes Barthelemy, and Albert Fert. Tunnel junctions with multiferroic barriers. *NATURE MATERIALS*, 6(4):296–302, APR 2007.

[63] V. Garcia, S. Fusil, K. Bouzehouane, S. Enouz-Vedrenne, N. D. Mathur, A. Barthelemy, and M. Bibes. Giant tunnel electroresistance for non-destructive readout of ferroelectric states. *NATURE*, 460(7251):81–84, JUL 2 2009.

[64] V. Garcia, M. Bibes, L. Bocher, S. Valencia, F. Kronast, A. Crassous, X. Moya, S. Enouz-Vedrenne, A. Gloter, D. Imhoff, C. Deranlot, N. D. Mathur, S. Fusil, K. Bouzehouane, and A. Barthelemy. Ferroelectric Control of Spin Polarization. *SCIENCE*, 327(5969):1106–1110, FEB 26 2010.

[65] Andre Chanthbouala, Vincent Garcia, Ryan O. Cherifi, Karim Bouzehouane, Stephane Fusil, Xavier Moya, Stephane Xavier, Hiroyuki Yamada, Cyrile Deranlot, Neil D. Mathur, Manuel Bibes, Agnes Barthelemy, and Julie Grollier. A ferroelectric memristor. *NATURE MATERIALS*, 11(10):860–864, OCT 2012.

[66] Andre Chanthbouala, Arnaud Crassous, Vincent Garcia, Karim Bouzehouane, Stephane Fusil, Xavier Moya, Julie Allibe, Bruno Dlubak, Julie Grollier, Stephane Xavier, Cyrile Deranlot, Amir Moshar, Roger Proksch, Neil D. Mathur, Manuel Bibes, and Agnes Barthelemy. Solid-state memories based on ferroelectric tunnel junctions. *NATURE NANOTECHNOLOGY*, 7(2):101–104, FEB 2012.

[67] EC STONER and EP WOHLFARTH. INTERPRETATION OF HIGH COERCIVITY IN FERROMAGNETIC MATERIALS. *NATURE*, 160(4071):650–651, 1947.

[68] EC STONER and EP WOHLFARTH. A MECHANISM OF MAGNETIC HYSTERESIS IN HETEROGENEOUS ALLOYS. *PHILOSOPHICAL TRANSACTIONS OF THE ROYAL SOCIETY OF LONDON SERIES A-MATHEMATICAL AND PHYSICAL SCIENCES*, 240(826):599–642, 1948.

[69] WH MEIKLEJOHN and CP BEAN. NEW MAGNETIC ANISOTROPY. *PHYSICAL REVIEW*, 102(5):1413–1414, 1956.

[70] JCS Kools. Exchange-biased spin-valves for magnetic storage. *IEEE TRANSACTIONS ON MAGNETICS*, 32(4, Part 2):3165–3184, JUL 1996.

[71] SSP Parkin, KP Roche, MG Samant, PM Rice, RB Beyers, RE Scheuerlein, EJ O'Sullivan, SL Brown, J Bucchigano, DW Abraham, Y Lu, M Rooks, PL Trouilloud, RA Wanner, and WJ Gallagher. Exchange-biased magnetic tunnel junctions and application to nonvolatile magnetic random access memory (invited). *JOURNAL OF APPLIED PHYSICS*, 85(8, Part 2b):5828–5833, APR 15 1999.

[72] J Nogues and IK Schuller. Exchange bias. *JOURNAL OF MAGNETISM AND MAGNETIC MATERIALS*, 192(2):203–232, FEB 1999.

[73] T Gredig, IN Krivorotov, P Eames, and ED Dahlberg. Unidirectional coercivity enhancement in exchange-biased Co/CoO. *APPLIED PHYSICS LETTERS*, 81(7):1270–1272, AUG 12 2002.

[74] C Prados, E Pina, A Hernando, and A Montone. Reversal of exchange bias in nanocrystalline antiferromagnetic-ferromagnetic bilayers. *JOURNAL OF PHYSICS-CONDENSED MATTER*, 14(43):10063–10074, NOV 4 2002.

[75] J Nogues, D Lederman, TJ Moran, and IK Schuller. Positive exchange bias in FeF2-Fe bilayers. *PHYSICAL REVIEW LETTERS*, 76(24):4624–4627, JUN 10 1996.

[76] J Nogues, D Lederman, TJ Moran, IK Schuller, and KV Rao. Large exchange bias and its connection to interface structure in FeF2-Fe bilayers. *APPLIED PHYSICS LETTERS*, 68(22):3186–3188, MAY 27 1996.

[77] F Radu, M Etzkorn, R Siebrecht, T Schmitte, K Westerholt, and H Zabel. Interfacial domain formation during magnetization reversal in exchange-biased CoO/Co bilayers. *PHYSICAL REVIEW B*, 67(13), APR 1 2003.

[78] M Gruyters and D Riegel. Strong exchange bias by a single layer of independent antiferromagnetic grains: The CoO/Co model system. *PHYSICAL REVIEW B*, 63(5), FEB 1 2001.

[79] Florin Radu and Hartmut Zabel. Exchange bias effect of ferro-/antiferromagnetic heterostructures. *Springer Tracts in Modern Physics*, 227:97–184, 2008.

[80] WH MEIKLEJOHN. EXCHANGE ANISOTROPY - A REVIEW. *JOURNAL OF APPLIED PHYSICS*, 33(3):1328–&, 1962.

[81] WH MEIKLEJOHN and CP BEAN. NEW MAGNETIC ANISOTROPY. *PHYSICAL REVIEW*, 105(3):904–913, 1957.

[82] H Fujiwara, C Hou, M Sun, HS Cho, and K Nishioka. Effect of exchange coupling of polycrystalline antiferromagnetic layers on the magnetization behavior of soft magnetic layers. *IEEE TRANSACTIONS ON MAGNETICS*, 35(5, Part 1):3082–3087, SEP 1999. 1999 International Magnetics Conference (INTERMAG 99), KYONGJU, SOUTH KOREA, MAY 18-21, 1999.

[83] D MAURI, HC SIEGMANN, PS BAGUS, and E KAY. SIMPLE-MODEL FOR THIN FERROMAGNETIC-FILMS EXCHANGE COUPLED TO AN ANTIFERROMAGNETIC SUBSTRATE. *JOURNAL OF APPLIED PHYSICS*, 62(7):3047–3049, OCT 1 1987.

[84] AP MALOZEMOFF. RANDOM-FIELD MODEL OF EXCHANGE-ANISOTROPY AT ROUGH FERROMAGNETIC-ANTIFERROMAGNETIC INTERFACES. *PHYSICAL REVIEW B*, 35(7):3679–3682, MAR 1 1987.

[85] AP MALOZEMOFF. MECHANISMS OF EXCHANGE-ANISOTROPY. *JOURNAL OF APPLIED PHYSICS*, 63(8, Part 3):3874–3879, APR 15 1988.

[86] AP MALOZEMOFF. HEISENBERG-TO-ISING CROSSOVER IN A RANDOM-FIELD MODEL WITH UNIAXIAL ANISOTROPY. *PHYSICAL REVIEW B*, 37(13):7673–7679, MAY 1 1988.

[87] NC Koon. Calculations of exchange bias in thin films with ferromagnetic/antiferromagnetic interfaces. *PHYSICAL REVIEW LETTERS*, 78(25):4865–4868, JUN 23 1997.

[88] TC Schulthess and WH Butler. Consequences of spin-flop coupling in exchange biased films. *PHYSICAL REVIEW LETTERS*, 81(20):4516–4519, NOV 16 1998.

[89] RC O'Handley. Modern Magnetic Materials:Principles and Applications. *Wiley, New York*, ():521, 1999.

[90] H.J. Brikenbeil and R.W. Cahn. Induced magnetic anisotropy created by magnetic or stress annealing of iron-aluminium alloys. *Journal of Applied Physics*, 32:362S–363S, 1961.

[91] B Hofmann and H Kronmuller. Stress-induced magnetic anisotropy in nanocrystalline FeCuNbSiB alloy. *JOURNAL OF MAGNETISM AND MAGNETIC MATERIALS*, 152(1-2):91–98, JAN 1996.

[92] RC HALL. MAGNETIC ANISOTROPY AND MAGNETOSTRICTION OF ORDERED AND DISORDERED COBALT-IRON ALLOYS. *JOURNAL OF APPLIED PHYSICS*, 31(5):S157–S158, 1960.

[93] RC OHANDLEY. MAGNETOSTRICTION OF TRANSITION-METAL-METALLOID GLASSES - TEMPERATURE-DEPENDENCE. *PHYSICAL REVIEW B*, 18(2):930–938, 1978.

[94] Tuomas H. E. Lahtinen, Kevin J. A. Franke, and Sebastiaan van Dijken. Electric-field control of magnetic domain wall motion and local magnetization reversal. *SCIENTIFIC REPORTS*, 2, FEB 10 2012.

[95] YF POPOV, AK ZVEZDIN, GP VOROBEV, AM KADOMTSEVA, VA MURASHEV, and DN RAKOV. LINEAR MAGNETOELECTRIC EFFECT AND PHASE-TRANSITIONS IN BISMUTH FERRITE, BIFEO3. *JETP LETTERS*, 57(1):69–73, JAN 10 1993.

[96] C MICHEL, JM MOREAU, ACHENBAC.GD, R GERSON, and WJ JAMES. ATOMIC STRUCTURE OF BIFEO3. *SOLID STATE COMMUNICATIONS*, 7(9):701–&, 1969.

[97] F KUBEL and H SCHMID. STRUCTURE OF A FERROELECTRIC AND FERROELASTIC MONODOMAIN CRYSTAL OF THE PEROVSKITE BIFEO3. *ACTA CRYSTALLOGRAPHICA SECTION B-STRUCTURAL SCIENCE*, 46(Part 6):698–702, DEC 1 1990.

[98] JR TEAGUE, R GERSON, and WJ JAMES. DIELECTRIC HYSTERESIS IN SINGLE CRYSTAL BIFEO3. *SOLID STATE COMMUNICATIONS*, 8(13):1073–&, 1970.

[99] GA SMOLENSKII, VM YUDIN, ES SHER, and YE STOLYPIN. ANTIFERROMAGNETIC PROPERTIES OF SOME PEROVSKITES. *SOVIET PHYSICS JETP-USSR*, 16(3):622–624, 1963.

[100] I SOSNOWSKA, T PETERLINNEUMAIER, and E STEICHELE. SPIRAL MAGNETIC-ORDERING IN BISMUTH FERRITE. *JOURNAL OF PHYSICS C-SOLID STATE PHYSICS*, 15(23):4835–4846, 1982.

[101] P FISCHER, M POLOMSKA, I SOSNOWSKA, and M SZYMANSKI. TEMPERATURE-DEPENDENCE OF THE CRYSTAL AND MAGNETIC-STRUCTURES OF BIFEO3. *JOURNAL OF PHYSICS C-SOLID STATE PHYSICS*, 13(10):1931–1940, 1980.

[102] D. Lebeugle, A. Mougin, M. Viret, D. Colson, and L. Ranno. Electric Field Switching of the Magnetic Anisotropy of a Ferromagnetic Layer Exchange Coupled to the Multiferroic Compound BiFeO3. *PHYSICAL REVIEW LETTERS*, 103(25), DEC 18 2009.

[103] D. Lebeugle, D. Colson, A. Forget, M. Viret, P. Bonville, J. F. Marucco, and S. Fusil. Room-temperature coexistence of large electric polarization and magnetic order in BiFeO3 single crystals. *PHYSICAL REVIEW B*, 76(2), JUL 2007.

[104] FM Bai, JL Wang, M Wuttig, JF Li, NG Wang, AP Pyatakov, AK Zvezdin, LE Cross, and D Viehland. Destruction of spin cycloid in (111)(c)-oriented BiFeO3 thin films by epitiaxial constraint: Enhanced polarization and release of latent magnetization. *APPLIED PHYSICS LETTERS*, 86(3), JAN 17 2005.

[105] Lane W. Martin, Ying-Hao Chu, Mikel B. Holcomb, Mark Huijben, Pu Yu, Shu-Jen Han, Donkoun Lee, Shan X. Wang, and R. Ramesh. Nanoscale control of exchange bias with BiFeO3 thin films. *Nano Letters*, 8(7):2050–2055, JUL 2008.

[106] F Zavaliche, H Zheng, L Mohaddes-Ardabili, SY Yang, Q Zhan, P Shafer, E Reilly, R Chopdekar, Y Jia, P Wright, DG Schlom, Y Suzuki, and R Ramesh. Electric field-induced magnetization switching in epitaxial columnar nanostructures. *NANO LETTERS*, 5(9):1793–1796, SEP 2005.

[107] Ying-Hao Chu, Qing He, Chan-Ho Yang, Pu Yu, Lane W. Martin, Padraic Shafer, and R. Ramesh. Nanoscale Control of Domain Architectures in BiFeO3 Thin Films. *Nano Letters*, 9(4):1726–1730, APR 2009.

[108] MR SCHEINFEIN, J UNGURIS, MH KELLEY, DT PIERCE, and RJ CELOTTA. SCANNING ELECTRON-MICROSCOPY WITH POLARIZATION ANALYSIS (SEMPA). *REVIEW OF SCIENTIFIC INSTRUMENTS*, 61(10, Part 1):2501–2526, OCT 1990.

[109] HP Oepen, G Steierl, and J Kirschner. Scanning electron microscope with polarization analysis: Micromagnetic structures in ultrathin films. *JOURNAL OF VACUUM SCIENCE & TECHNOLOGY B*, 20(6):2535–2538, NOV-DEC 2002. 3rd Low Energy Electron Microscopy/Photoemission Electron Microscopy Workshop, ALBUQUERQUE, NM, MAY 14-17, 2002.

[110] SK Streiffer, CB Parker, AE Romanov, MJ Lefevre, L Zhao, JS Speck, W Pompe, CM Foster, and GR Bai. Domain patterns in epitaxial rhombohedral ferroelectric films. I. Geometry and experiments. *Journal of Applied Physics*, 83(5):2742–2753, MAR 1 1998.

[111] EB Myers, DC Ralph, JA Katine, RN Louie, and RA Buhrman. Current-induced switching of domains in magnetic multilayer devices. *Science*, 285(5429):867–870, AUG 6 1999.

[112] D. Chiba, M. Sawicki, Y. Nishitani, Y. Nakatani, F. Matsukura, and H. Ohno. Magnetization vector manipulation by electric fields. *Nature*, 455(7212):515–518, SEP 25 2008.

[113] H Ohno, D Chiba, F Matsukura, T Omiya, E Abe, T Dietl, Y Ohno, and K Ohtani. Electric-field control of ferromagnetism. *Nature*, 408(6815):944–946, DEC 21 2000.

[114] Sarbeswar Sahoo, Srinivas Polisetty, Chun-Gang Duan, Sitaram S. Jaswal, Evgeny Y. Tsymbal, and Christian Binek. Ferroelectric control of magnetism in BaTiO3/Fe heterostructures via interface strain coupling. *Physical Review B*, 76(9), SEP 2007.

[115] S. Gepraegs, A. Brandlmaier, M. Opel, R. Gross, and S. T. B. Goennenwein. Electric field controlled manipulation of the magnetization in Ni/BaTiO3 hybrid structures. *APPLIED PHYSICS LETTERS*, 96(14), APR 5 2010.

[116] Alexandr Chernyshov, Mason Overby, Xinyu Liu, Jacek K. Furdyna, Yuli Lyanda-Geller, and Leonid P. Rokhinson. Evidence for reversible control of magnetization in a ferromagnetic material by means of spin-orbit magnetic field. *Nature Physics*, 5(9):656–659, SEP 2009.

[117] Tao Yang, Takashi Kimura, and Yoshichika Otani. Giant spin-accumulation signal and pure spin-current-induced reversible magnetization switching. *NATURE PHYSICS*, 4(11):851–854, NOV 2008.

[118] W. Eerenstein, N. D. Mathur, and J. F. Scott. Multiferroic and magnetoelectric materials. *Nature*, 442(7104):759–765, AUG 17 2006.

[119] NA Spaldin and M Fiebig. The renaissance of magnetoelectric multiferroics. *Science*, 309(5733):391–392, JUL 15 2005.

[120] T Lottermoser, T Lonkai, U Amann, D Hohlwein, J Ihringer, and M Fiebig. Magnetic phase control by an electric field. *Nature*, 430(6999):541–544, JUL 29 2004.

[121] D. Lebeugle, D. Colson, A. Forget, M. Viret, A. M. Bataille, and A. Gukasov. Electric-field-induced spin flop in BiFeO(3) single crystals at room temperature. *Physical Review Letters*, 100(22), JUN 6 2008.

[122] Seoungsu Lee, W. Ratcliff, II, S-W. Cheong, and V. Kiryukhin. Electric field control of the magnetic state in BiFeO3 single crystals. *APPLIED PHYSICS LETTERS*, 92(19), MAY 12 2008.

[123] V. Laukhin, V. Skumryev, X. Marti, D. Hrabovsky, F. Sanchez, M. V. Garcia-Cuenca, C. Ferrater, M. Varela, U. Lueders, J. F. Bobo, and J. Fontcuberta. Electric-field control of exchange bias in multiferroic epitaxial heterostructures. *PHYSICAL REVIEW LETTERS*, 97(22), DEC 1 2006.

[124] V. Skumryev, V. Laukhin, I. Fina, X. Marti, F. Sanchez, M. Gospodinov, and J. Fontcuberta. Magnetization Reversal by Electric-Field Decoupling of Magnetic and Ferroelectric Domain Walls in Multiferroic-Based Heterostructures. *PHYSICAL REVIEW LETTERS*, 106(5), FEB 3 2011.

[125] P Borisov, A Hochstrat, X Chen, W Kleemann, and C Binek. Magnetoelectric switching of exchange bias. *PHYSICAL REVIEW LETTERS*, 94(11), MAR 25 2005.

[126] Xi He, Yi Wang, Ning Wu, Anthony N. Caruso, Elio Vescovo, Kirill D. Belashchenko, Peter A. Dowben, and Christian Binek. Robust isothermal electric control of exchange bias at room temperature. *NATURE MATERIALS*, 9(7):579–585, JUL 2010.

[127] S. M. Wu, Shane A. Cybart, P. Yu, M. D. Rossell, J. X. Zhang, R. Ramesh, and R. C. Dynes. Reversible electric control of exchange bias in a multiferroic field-effect device. *Nature Materials*, 9(9):756–761, SEP 2010.

[128] J. T. Heron, M. Trassin, K. Ashraf, M. Gajek, Q. He, S. Y. Yang, D. E. Nikonov, Y-H. Chu, S. Salahuddin, and R. Ramesh. Electric-Field-Induced Magnetization Reversal in a Ferromagnet-Multiferroic Heterostructure. *Physical Review Letters*, 107(21), NOV 14 2011.

[129] BH Miller and ED Dahlberg. Use of the anisotropic magnetoresistance to measure exchange anisotropy in Co/CoO bilayers. *APPLIED PHYSICS LETTERS*, 69(25):3932–3934, DEC 16 1996.

[130] K Ashraf and S Salahuddin. Phase field model of domain dynamics in micron scale, ultrathin ferroelectric films: Application for multiferroic bismuth ferrite. *Journal of Applied Physics*, 112(074102):1–11, Oct 2012.

[131] S. H. Baek, H. W. Jang, C. M. Folkman, Y. L. Li, B. Winchester, J. X. Zhang, Q. He, Y. H. Chu, C. T. Nelson, M. S. Rzchowski, X. Q. Pan, R. Ramesh, L. Q. Chen, and C. B. Eom. Ferroelastic switching for nanoscale non-volatile magnetoelectric devices. *NATURE MATERIALS*, 9(4):309–314, APR 2010.

[132] TR MCGUIRE and RI POTTER. ANISOTROPIC MAGNETORESISTANCE IN FERROMAGNETIC 3D ALLOYS. *IEEE TRANSACTIONS ON MAGNETICS*, 11(4):1018–1038, 1975.

[133] Claude Ederer and Craig J. Fennie. Electric-field switchable magnetization via the Dzyaloshinskii-Moriya interaction: FeTiO3 versus BiFeO3. *JOURNAL OF PHYSICS-CONDENSED MATTER*, 20(43), OCT 29 2008.

[134] Luqiao Liu, Chi-Feng Pai, Y. Li, H. W. Tseng, D. C. Ralph, and R. A. Buhrman. Spin-Torque Switching with the Giant Spin Hall Effect of Tantalum. *Science*, 336(6081):555–558, MAY 4 2012.

[135] Chi-Feng Pai, Luqiao Liu, Y. Li, H. W. Tseng, D. C. Ralph, and R. A. Buhrman. Spin Transfer Torque Devices utilizing the Giant Spin Hall Effect of Tungsten. *ArXiv*, 1208.1711, AUG 8 2012.

[136] Evgeny Y. Tsymbal. Spintronics: Electric toggling of magnets. *Nature Materials*, 11(1):12–13, JAN 2012.

[137] Wei-Gang Wang, Mingen Li, Stephen Hageman, and C. L. Chien. Electric-field-assisted switching in magnetic tunnel junctions. *Nature Materials*, 11(1):64–68, JAN 2012.

[138] Yoichi Shiota, Takayuki Nozaki, Frederic Bonell, Shinichi Murakami, Teruya Shinjo, and Yoshishige Suzuki. Induction of coherent magnetization switching in a few atomic layers of FeCo using voltage pulses. *Nature Materials*, 11(1):39–43, JAN 2012.

[139] Y. Yamasaki, H. Sagayama, T. Goto, M. Matsuura, K. Hirota, T. Arima, and Y. Tokura. Electric control of spin helicity in a magnetic ferroelectric. *Physical Review Letters*, 98(14), APR 6 2007.

[140] Y. Bodenthin, U. Staub, M. Garcia-Fernandez, M. Janoschek, J. Schlappa, E. I. Golovenchits, V. A. Sanina, and S. G. Lushnikov. Manipulating the magnetic structure with electric fields in multiferroic ErMn(2)O(5). *Physical Review Leeters*, 100(2), JAN 18 2008.

[141] EY Tsymbal, ON Mryasov, and PR LeClair. Spin-dependent tunnelling in magnetic tunnel junctions. *Journal of Physics-Condensed Matter*, 15(4):R109–R142, FEB 5 2003.

[142] Manuel Bibes and Agnes Barthelemy. Multiferroics: Towards a magnetoelectric memory. *Nature Materials*, 7(6):425–426, JUN 2008.

[143] Ming Liu, Shandong Li, Ogheneyunume Obi, Jing Lou, Scott Rand, and Nian X. Sun. Electric field modulation of magnetoresistance in multiferroic heterostructures for ultralow power electronics. *Applied Physics Letters*, 98(22), MAY 30 2011.

[144] D. T. Huong Giang, V. N. Thuc, and N. H. Duc. Electric field-induced magnetoresistance in spin-valve/piezoelectric multiferroic laminates for low-power spintronics. *Journal of Magnetism and Magnetic Materials*, 324(13):2019–2023, JUL 2012.

[145] Julie Allibe, Stephane Fusil, Karim Bouzehouane, Christophe Daumont, Daniel Sando, Eric Jacquet, Cyrille Deranlot, Manuel Bibes, and Agnes Barthelemy. Room Temperature Electrical Manipulation of Giant Magnetoresistance in Spin Valves Exchange-Biased with $BiFeO_3$. *Nano Letters*, 12(3):1141–1145, MAR 2012.

[146] X. Zhang, Y. H. Wang, D. L. Zhang, G. Q. Zhang, H. L. Yang, J. Miao, X. G. Xu, and Y. Jiang. Electric-Field-Induced Change of the Magnetoresistance in the Multiferroic Spin-Valve Based on BiFeO3 Film. *IEEE Transactions on Magnetics*, 47(10):3139–3142, OCT 2011. Conference on International Magnetics (INTERMAG), Taipei, TAIWAN, APR 25-29, 2011.

[147] Q. He, C-H. Yeh, J-C. Yang, G. Singh-Bhalla, C-W. Liang, P-W. Chiu, G. Catalan, L. W. Martin, Y-H. Chu, J. F. Scott, and R. Ramesh. Magnetotransport at Domain Walls in $BiFeO_3$. *Physical Review Letters*, 108(6), FEB 9 2012.

[148] H. Bea, M. Bibes, F. Ott, B. Dupe, X. H. Zhu, S. Petit, S. Fusil, C. Deranlot, K. Bouzehouane, and A. Barthelemy. Mechanisms of exchange bias with multiferroic BiFeO(3) epitaxial thin films. *Physical Review Letters*, 100(1), JAN 11 2008.

[149] S. Ikeda, K. Miura, H. Yamamoto, K. Mizunuma, H. D. Gan, M. Endo, S. Kanai, J. Hayakawa, F. Matsukura, and H. Ohno. A perpendicular-anisotropy CoFeB-MgO magnetic tunnel junction. *Nature Materials*, 9(9):721–724, SEP 2010.

[150] Y. H. Chu, T. Zhao, M. P. Cruz, Q. Zhan, P. L. Yang, L. W. Martin, M. Huijben, C. H. Yang, F. Zavaliche, H. Zheng, and R. Ramesh. Ferroelectric size effects in multiferroic BiFeO3 thin films. *Applied Physics Letters*, 90(25), JUN 18 2007.

[151] Y. H. Chu, Q. Zhan, C. H. Yang, M. P. Cruz, L. W. Martin, T. Zhao, P. Yu, R. Ramesh, P. T. Joseph, I. N. Lin, W. Tian, and D. G. Schlom. Low voltage performance of epitaxial BiFeO(3) films on Si substrates through lanthanum substitution. *Applied Physics Letters*, 92(10), MAR 10 2008.

[152] Axel Lubk, S. Gemming, and N. A. Spaldin. First-principles study of ferroelectric domain walls in multiferroic bismuth ferrite. *Physical Review B*, 80(10), SEP 2009.

[153] M. P. Cruz, Y. H. Chu, J. X. Zhang, P. L. Yang, F. Zavaliche, Q. He, P. Shafer, L. Q. Chen, and R. Ramesh. Strain control of domain-wall stability in epitaxial BiFeO3 (110) films. *Physical Review Letters*, 99(21), NOV 23 2007.

[154] S. K. Mishra, M. Trassin, J. D. Clarkson, J. T. Heron, J. X. Zhang, S. J. Suresha, P. B. Rossen, Y. H. Chu, E. Arenholz, and R. Ramesh. Orbital distortion mediated reduced anisotropy in spin-engineered multiferroic thin films. *Submitted to Physical Review Letters*, 2012.

[155] H-H.S. Lee. So little bandwidth, so many memories. *Workshop on architecting memory technologies*, http://web.engr.oregonstate.edu/ sllu/lee.pdf():, Sept 16, 2012 2010.

[156] P. Yu, J. S. Lee, S. Okamoto, M. D. Rossell, M. Huijben, C. H. Yang, Q. He, J. X. Zhang, S. Y. Yang, M. J. Lee, Q. M. Ramasse, R. Erni, Y. H. Chu, D. A. Arena, C. C. Kao, L. W. Martin, and R. Ramesh. Interface Ferromagnetism and Orbital Reconstruction in BiFeO3-La0.7Sr0.3MnO3 Heterostructures. *Physical Review Letters*, 105(2), JUL 6 2010.

[157] P. Nemec, E. Rozkotova, N. Tesarova, F. Trojanek, E. De Ranieri, K. Olejnik, J. Zemen, V. Novak, M. Cukr, P. Maly, and T. Jungwirth. Experimental observation of the optical spin transfer torque. *Nature Physics*, 8(5):411–415, MAY 2012.

[158] Wei-Gang Wang, Mingen Li, Stephen Hageman, and C. L. Chien. Electric-field-assisted switching in magnetic tunnel junctions. *Nature Materials*, 11(1):64–68, JAN 2012.

[159] Yoichi Shiota, Takayuki Nozaki, Frederic Bonell, Shinichi Murakami, Teruya Shinjo, and Yoshishige Suzuki. Induction of coherent magnetization switching in a few atomic layers of FeCo using voltage pulses. *Nature Materials*, 11(1):39–43, JAN 2012.

[160] YK Kato, RC Myers, AC Gossard, and DD Awschalom. Observation of the spin Hall effect in semiconductors. *Science*, 306(5703):1910–1913, DEC 10 2004.

[161] T. Kimura, Y. Otani, T. Sato, S. Takahashi, and S. Maekawa. Room-temperature reversible spin Hall effect. *Physical Review Letters*, 98(15), APR 13 2007.

[162] F. Zavaliche, S. Y. Yang, T. Zhao, Y. H. Chu, M. P. Cruz, C. B. Eom, and R. Ramesh. Multiferroic BiFeO3 films: domain structure and polarization dynamics. *PHASE TRANSITIONS*, 79(12):991–1017, DEC 2006.

[163] LM Eng, HJ Guntherodt, GA Schneider, U Kopke, and JM Saldana. Nanoscale reconstruction of surface crystallography from three-dimensional polarization distribution in ferroelectric barium-titanate ceramics. *APPLIED PHYSICS LETTERS*, 74(2):233–235, JAN 11 1999.

[164] Nina Balke, Igor Bdikin, Sergei V. Kalinin, and Andrei L. Kholkin. Electromechanical Imaging and Spectroscopy of Ferroelectric and Piezoelectric Materials: State of the Art and Prospects for the Future. *JOURNAL OF THE AMERICAN CERAMIC SOCIETY*, 92(8):1629–1647, AUG 2009.

[165] A Verdaguer, GM Sacha, H Bluhm, and M Salmeron. Molecular structure of water at interfaces: Wetting at the nanometer scale. *CHEMICAL REVIEWS*, 106(4):1478–1510, APR 2006.

[166] G. M. Sacha, A. Verdaguer, and M. Salmeron. Induced water condensation and bridge formation by electric fields in atomic force microscopy. *JOURNAL OF PHYSICAL CHEMISTRY B*, 110(30):14870–14873, AUG 3 2006.

Appendix A

Other methods of electric field control of magnetism

In this thesis I have focused on using the intrinsic magnetoelectric coupling in proper single phase multiferroics, via the Dzyaloshinskii-Moriya interaction, as the bridge between electronic and spin orders to enable the electric field control of magnetism. The focus of this thesis is on single phase multiferroic composites where a combination of the intrinsic magnetoelectric coupling and interface magnetic exchange coupling are used to establish the electric field control of large magnetization. It is important to spend some time reflecting on other pathways that have shown an electrical control of magnetism. Note: I will broaden our discussion here to include some current driven techniques that are quite robust or show a low-energy control of a magnetic phenomenon regardless if they are multiferrous or non-multiferrous materials. Additionally, I encourage the reader to reflect on the possibility of other mechanisms that can bridge the link between an electric field and magnetism in the solid state.

A.1 Composite multiferroics

Composite multiferroics are material composites that combine ferroelectric/ferroelastic materials with ferromangetic materials. An examble could be a Fe film on $BaTiO_3$. Typically the route to the electric field control of ferromagnetism is through lattice coupling where the ferroelectric distorts the lattice and through lattice coupling, the lattice of the ferromanget as well. The magnetization and magnetic anisotropy of the magnet will rotate in response to the lattice distortion through the inverse magnetostriction effect. Composite multiferroics have received so much attention due to the deficiencies of single phase multiferroics - namely low T_cs and, generally, low magnetic moments. With the capabilities of room temperature functionality, ease of growth, and large magnetoelectric coupling coefficients, researchers of composite

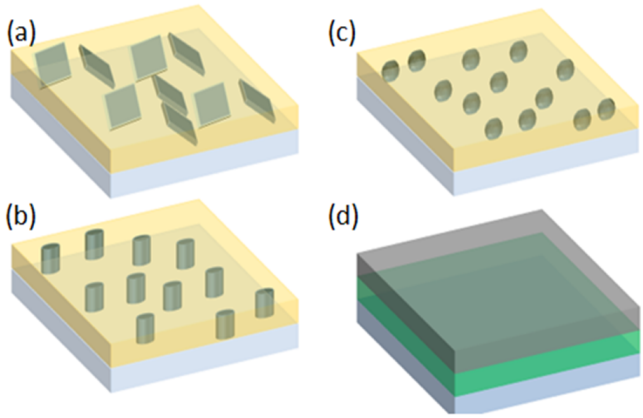

Figure A.1: Schematics of nanostructured composites. The nanostructures (grey) reside in a thin film matrix (orange) that is deposited on a substrate (blue). (a) nanosheets, (b) nanopillars, (c) nanoprecipitates and (d) laminar thin films.

multiferroics have been able to demonstrate magnetoelectric functionalities in a wide variety of device applications (at least in bulk). [36] Composite multiferroics can be created in a variety of structural variants using controlled growth conditions. Similar to composite systems that can be created in bulk, self-assembly can create thin film nanoscale composites in the form of nanopillar, nanosheet and nanoparticulate composites. Due to immiscibility, the two components of the composite will separate forming the nanoscale composite system. This is common in perovskite - spinel composite systems, where the spinel phase separates into one of the nanostructures embedded in the perovskite matrix. An additional benefit of the composite system is the high surface to volume ration of the nanostructures that are formed in these systems. This high surface area means a greater lattice coupling to the matrix state and in these nano-phase separated thin film systems the adverse effect of lattice clamping from the substrate is greatly reduced, providing a significant magnetoelectric coupling. Figure A.1 gives simple examples of such composite structures.

Furthermore, a controlled growth process can produce laminar thin film heterostructures. Laminar thin film heterostructures come with a huge advantage of the easy deposition of materials and a broad materials selection to build a composite multiferroic. This has largely been the reason why this approach has been favored over phase separated composites. However, this composite geometry suffers from the fact that the substrate clamps the piezoelectric thin film, inhibiting the lattice expansion and strain produce from an applied voltage. This limitation can reduce the magnetoelectric coefficient by a factor of five.

Despite the structural variation, the pathway to the electrical control of magnetism

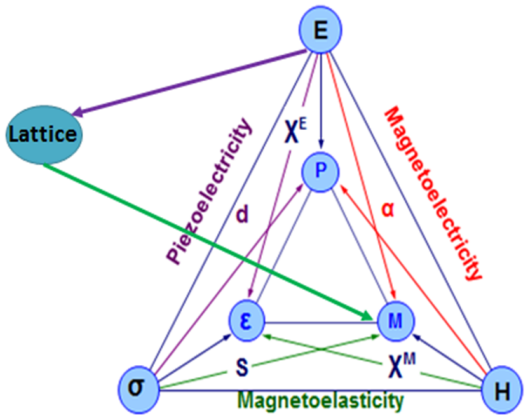

Figure A.2: Schematic of the route to electric field control of magnetism for multiferroic composites. The coupling is mediated through the sharing of the lattice by which strain can be transferred from the piezoelectric matrix to the magnetostrictive ferromagnet.

is the same in each case. Figure 5 illustrates this common pathway on our map of the electrical control of magnetism. In this case the common point of both subsystems is the lattice. Since both layers share the same lattice, they are then coupled through this means. The ferroelectric or piezoelectric will have its lattice distorted with an applied electric field; therefore the lattice of the ferromagnetic subsystem will also have its lattice distorted. When the ferromagnet displays the magnetostrictive effect (or more properly, the inverse magnetostrictive effect) the lattice distortion in the ferromagnet induces a change in its magnetic anisotropy. A rotation of the magnetic anisotropy is accompanied by a rotation of the magnetization between 0 and 90 degrees. In order to reverse a magnetization, a small magnetic field must be applied to break the time reversal invariance.

While the benefits of this approach are quite valuable, it is not an approach that allows for a binary switch of the magnetization by 180. As we discussed previously, this is due to the lack of symmetry breaking by the coupling mechanisms. Lastly we will discuss an approach will combine the benefits of single phase and composite multiferroics, which enables the 180 reversal of a magnetization with an applied electric field.

A.2 Orbital coupling

One other degree of freedom is the orbital degree of freedom. The study of this freedom as a pathway to the electrical control of magnetism is relatively scarce due to

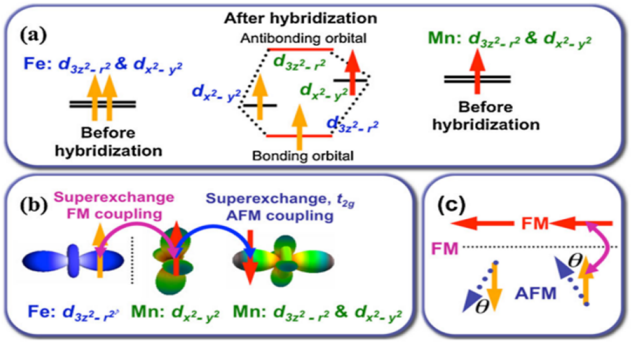

Figure A.3: (a) Schematic of the interface electronic orbital reconstruction, with hybridization, (b) Proposed interface spin configuration and coupling mechanism with dx^2-y^2 orbital ordering in the interfacial LSMO. (c) Schematic of the origin of the interface magnetism. Taken from reference [156]

the lack of room temperature capability. Nonetheless, it is a pathway which has shown that the electric field control of magnetic properties in a single phase multiferroic composite system composed of two perovskite oxides can be established. In the study of the $La_{.7}Sr_{.3}MnO_3$ (LSMO) / $BiFeO_3$ heterostructure at low temperature, an interface ferromagnetic ordering in the $BiFeO_3$ was discovered and attributed to an orbital reconstruction induced by the orbital ordering in the manganite (see Figure A.3). [156] This leads to a significant exchange bias interaction across the interface. Figure A.3(a) shows the proposed band alignment at the interface, keeping the Fermi energy continuous across the interface.

Then using the Goodenough-Kanamori-Anderson rules, the superexchange interactions between the Fe^{3+} and Mn^{3+} (4+) are ferromagnetic while the superexchange interaction between the interface Mn and the bulk Mn in the LSMO layer is antiferromagnetic (Figure A.3(b)). Figure A.3(c) summaries the results in terms of the $BiFeO_3$ magnetic structure at the interface of the heterostructure. The competition between the bulk antiferromagnetic order and the induced ferromagnetic order due to the orbital ordering leads to a significant canting of the $BiFeO_3$ magnetic structure. Then using this interface coupling through the Mn and Fe d-orbitals, the intrinsic magnetoelectric coupling of the $BiFeO_3$ was electrically manipulated to determine if the interface magnetic/orbital coupling could be changed. Indeed, researchers have shown that the exchange bias amplitude can be modulated reversibly with reversible cycling of the ferroelectric polarization of $BiFeO_3$. [127] As shown in Figure A.4 the exchange bias is modulate with the sequential voltage pulse, however this can be

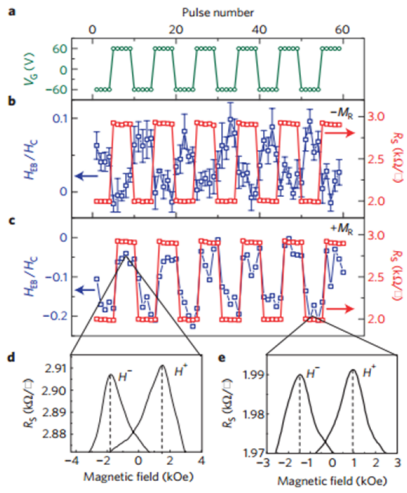

Figure A.4: (a) Shows the gate-voltage-pulse sequence used for the measurements. (b,c) Measurements of normalized exchange bias and peak resistance for the gate-pulse sequence. The exchange bias modulates with ferroelectric polarization; the data shown for (b) were obtained with a negative remanent magnetization in the LSMO channel whereas the data shown for (c) were obtained in positive remanent magnetization. (d,e) Examples of individual MR curves from the two resistance states. Taken from reference [127].

in-phase or out of phase with the change in the sheet resistance depending on the orientation of the magnetization of the LSMO layer.

Clearly this is a pathway that needs further scientific exploration. If such a coupling could be observed at room temperature, a great deal of excitement could be generated in this area. In the ideal case, the electrical control of magnetism and orbital order could be extended outside of heterostructures to single layer films such as the manganites which display large magnetoresistance due to a magnetic phase transition.

A.3 Carrier mediation magnetism

In magnetic semiconductors such as GaMnAs, the magnetism is mediated through a hybridized exchange interaction, such as a p-d interaction, between the charge carriers and the d electrons of the Mn. In the case of GaMnAs the carriers are holes and in the dilute limit it has been found that the Curie temperature scales as $p^{1/3}$, where p is the concentration of the holes. In these systems, the magnetism can be controlled simply by accumulating or depleting electrons in the semiconductor using a conventional MOSFET like structure like the one shown in Figure A.5. [113]

Researchers have shown that the ferromagnetic phase can be quenched completely

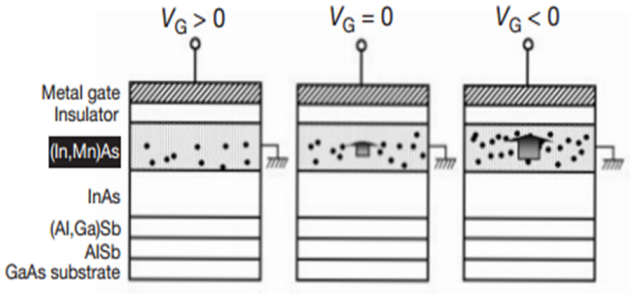

Figure A.5: A schematic of the metal-oxide-semiconductor structure used to accumulate or deplete holes from a magnetic semiconductor (InMnAs) using a gate voltage. The black dots are representations of holes in the magnetic semiconductor while the black arrow represents the magnitude of the magnetization. Taken from reference [113]

and that the magnetization, through control of the magnetic anisotropy, can be electrically controlled by modulating the carrier concentration with the applied voltage. The electrical control of magnetism has been shown in IV and III-V based magnetic semiconductors such as InMnAs, GaMnAs, GeMn. In the case of GaMnAs (Figure A.6), it was shown that the perpendicular anisotropy field can be modulated with an electric field and showed that the effect is dependent on the carrier density which they were able to saturate to a minimum value. [112]

Carrier mediated ferromagnetism has proven to be a quite robust technique for manipulation of magnetism with electric fields, but it is not without its short comings. Primarily, the curie temperatures of magnetic semiconductors are capped at 180K, significantly below room temperature. Additionally, the modulation of anisotropy cannot reverse a magnetization without the aid of an external magnetic bias; a similar issue arises in composite multiferroics. Additional benefits to the carrier mediated approach exist due to the ability to transfer angular momentum to the magnetization through light and the spin polarized current. This, of course, has led to the observation of magnetization switching and precession via optical and current driven spin torques. [157, 116]

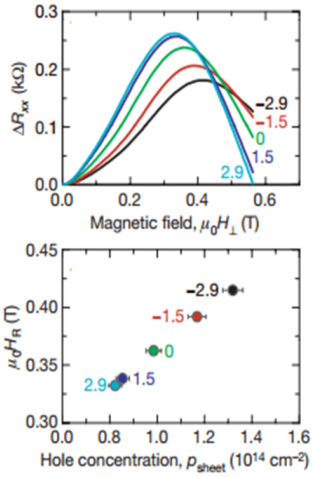

Figure A.6: (Top) The magnetic field at which ΔR_{xx} (the difference between R_{xx} (H) and R_{xx} (H = 0)) peaks is a measure of the perpendicular uniaxial anisotropy field. Magnetic field dependence of ΔR_{xx}, for different values of electric field in MV cm^{-1} at 5 K. The anisotropy field becomes lower when a positive electric field is applied and becomes higher when negative E is applied. (Bottom) Perpendicular anisotropy field as a function of the sheet hole concentration and applied voltage. Taken from reference [112].

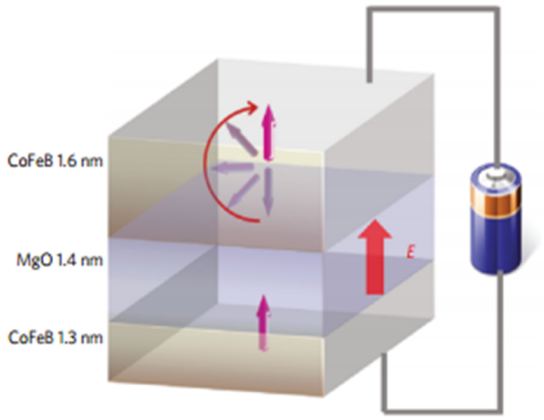

Figure A.7: Schematic of a magnetic tunnel junction with a thin magnetic layers showing perpendicular magnetic anisotropy. The electric field is applied through the thickness of the films. Taken from reference [158].

A.4 Surface Magnetocrystalline Anisotropy (SMCA)

In this section, the idea behind the electrical control of magnetism is very similar to the approach used in carrier mediated ferromagnetism. In very thin magnetic metals, the surface magnetocrystalline magnetic anisotropy (SMCA) dominates over the bulk anisotropy and favors an out-of-plane magnetization or what is referred to as a perpendicular magnetic anisotropy. The bulk anisotropy and the magnetostatic energy favor an in-plane magnetization direction. The strength of the surface anisotropy is very sensitive to the carrier density at the surface. The strength of the SMCA is dependent on the occupation of surface states which can be depleted with a voltage since an electric field can penetrate a metal for a few Angstroms. Thus the anisotropy and hence the magnetization can be toggled between in-plane and out-of-plane by depleting carriers from the surface with an applied voltage. There have been several examples of this kind of switching reported recently using magnetic tunnel junctions such as that shown in Figure A.7. [158] Furthermore, by cleverly tuning the width of the voltage pulse applied, the remnant magnetization of the thin magnetic layer can be reversed. [159] However, in order to obtain deterministic switching of the magnetization, a small magnetic bias must be applied and thus this approach is not truly a electric field control of ferromagnetism.

Figure A.8 shows the work of Shiota *et al.*, from reference [159]. In Figure A.8(a) is a schematic of the voltage pulses that are used in the magnetic simulations of (b) and the pulses used in (d) and (e). In Figure A.8(b) they use micromagnetic simulations to determine how far the magnetization will rotate under the duration of

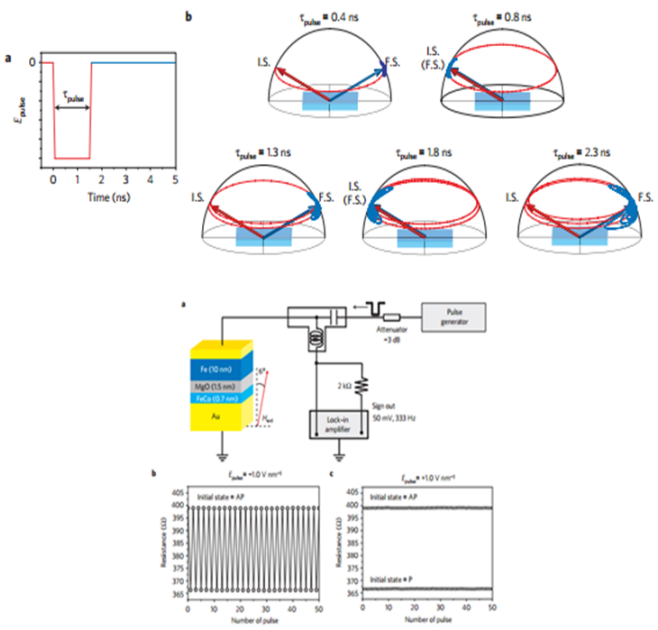

Figure A.8: (a) Schematic of voltage pulse profile used. (b) Simulations of magnetization precession as a function of pulse width. (c) Experimental configuration for pulsed measurements. (d) Toggling of the magnetic state of the magnetic tunnel junction with positive voltage. (e) Stability of states under applied negative voltage. Taken from reference [159].

the applied bias, I.S. stands for initial state and F.S. stands for final state. The voltage pulse creates a small out-of-plane anisotropy, bringing the magnetization out of plane slightly. The magnetization precesses about the out-of-plane direction causing the magnetization to change direction in-plane. Depending on the width of the pulse the in-plane component can be reversed or rotated 360 degrees or more. Using a .58ns negative voltage pulse, the authors were able to show that the resistance state of the magnetic tunnel junction could be toggled using this magnetization precession (Figure A.8(d)). Using a positive voltage does not toggle the state due to the inability to increase the strength of the SCMA.

A.5 Current Driven Techniques - Spin torque and Giant spin Hall effect

While we understand that a discussion of current driven techniques is a small deviation from our main objective, we include a short discussion of some techniques here since it fits with the global theme of low energy control of magnetization and due

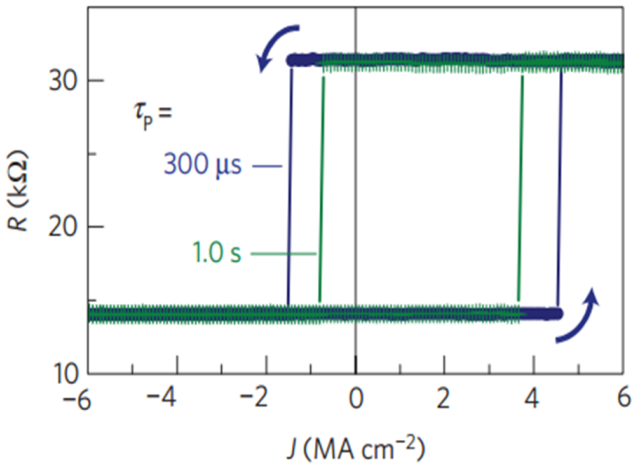

Figure A.9: Demonstration of the current driven switching as a function of current pulse width. Taken from reference [149].

to its impact on sience and memmory technology since its discovery in 1999. [111] As we discussed early in this chapter, the most energy effiecient spin torque device to date has shown a energy dissipation of 3mJ/cm^2 in a device size of 49nm. [149] Figure A.9 shows some results presented in [149]. As it can be seen the energy consumption is low but the power consumption is still rather high.

We have seen that spin torque uses a ferromagnet to spin polarize a large current density which is then directed at another ferromagnetic layer and is able to reverse the magnetization of this non-polarizing magnetic layer. However there are other ways to create a spin current. The spin Hall effect was first observed using optical methods in GaAs in 2004. [160] Shortly after, this effect was observed in metals. Recently, intrinsic and extrinsic spin-orbit effects have generated a large field of excitement. This is largely due to the observations of the spin Hall and inverse spin Hall effect in metals with a significant spin-orbit interaction such as Pt and Ta. [161, 134] Interestingly, the spin Hall effect observed in Ta was observed to be giant. In fact researchers have shown that by injecting a small current into a strip of Ta with a magnetic tunnel junction ion to of it (Figure A.10) that the magnetization of the bottom magnetic layer and hence the resistance state of the tunnel junction can be reversed. [134] while at the current state the energy dissipation is of the same order as spin torque switching, by tuning the geometry of the Ta and hence the resistance of the device, it is believed that the energy consumption can be reduce by at least one order of magnitude.

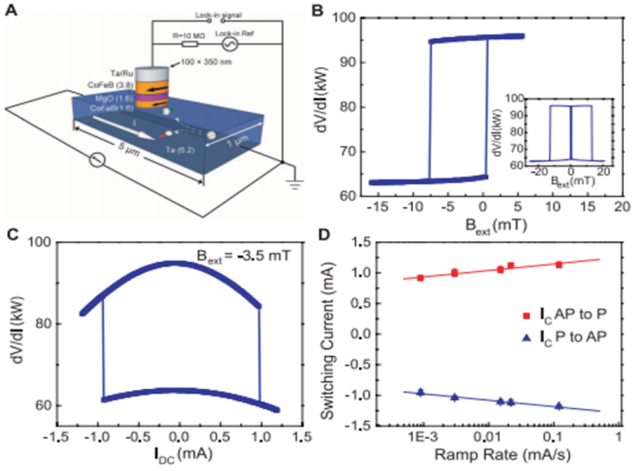

Figure A.10: Giant spin Hall effect switching of an in-plane magnetic tunnel junction device. Taken from [134].

Appendix B

Piezoresponse force microscopy: PFM

Details of the PFM technique are given due to the significance of the PFM measurements in the works presented herein. The details of the measurements have been reported previously by Zavaliche *et al.,*. [162] A DI-Veeco multimode AFM equipped with a Nanoscope IV controller was used to simultaneously image the surface topography, out-of-plane piezoresponse, and in-plane piezoresponse of $BiFeO_3$ films and the $Co_{.90}Fe_{.10}$ / $BiFeO_3$ devices. Images were taken at ambient condtions using a 6.3kHz AC bias.

B.1 Basics

Piezoresponce force microscopy (PFM) begins with a metal coated tip that is in contact with the film under test. PFM measures the mechanical response when an electrical voltage is applied to the sample surface with a conductive tip of an AFM. In response to the electrical stimulus, the sample then locally expands or contracts as shown in Figure B.1. When the tip is in contact with the surface, the local piezoelectric response is detected as the first harmonic component of the tip deflection. The phase of the electromechanical response of the surface yields information on the polarization direction below the tip. An AC voltage is applied between the tip and the back of the film as a laser is reflected from the back of the tip to a 4-quadrant photodetector. If the polarization has a out-of-plane component, an applied electric field can either cause a out-of-plane expansion or contraction of the lattice depending on the orientation of the applied electric field with respect to the polarization direction. Figures B.1(a) and B.1(b) illustrate this effect. Now, since an AC voltage is applied, the out-of-plane lattice parameter will expand and contract but the two polarization directions can be distinguished because the two will respond oppositely to the applied voltage. The photodiode will detect a signal that

is in phase with the applied ac voltage while for the other polarization variant, the detected signal will be out of phase with the applied voltage. This difference in phase is plotted as a color contrast in the out-of-plane PFM image.

If there are in-plane components, an out-of-plane electric field causes the regions to shear differently, resulting in the PFM tilting either to the left or the right depending on the polarization direction (see Figures B.1(c) and B.1(d)). The difference again results in the photodiode detecting a phase change with respect to the applied voltage and the phase contrast is plotted in the in-plane PFM image. Note that no contrast is obtainable along the long axis of the PFM tip. In order to determine the third component of the polarization vector, the same region of the sample previously measured must be measured again after rotating the sample by 90^o (since the tip cannot be rotated in this system). [163] Finally, piezoelectric response can be probed a DC bias on the tip has been applied. This can provide information on ferroelectric switching as well as more complex electrochemical and electrocapillary processes. [165, 166] For a comprehensive introduction to PFM, see the article by Balke *et al.,*. [164]

When considering a PFM image of $BiFeO_3$, there are only eight possible directions in which the polarization can point due to the rhombohedral symmetry of $BiFeO_3$ with the rhombohedral distortion along the pseudocubic <111> directions. So when considering in-plane and out-of-plane PFM images of the two variant (001) $BiFeO_3$ on $DyScO_3$ as in Figure B.2, the fact that the polarization must point along a pseudocubic <111> direction quickly determines the direction of the polarization in each domain. The out-of-plane PFM contrast shown in Figure B.2(b) is primarily white contrast indicating that the out-of-plane polarization of the film is largely pointing down into the substrate. There are some regions where the polarization points out of the film surface, but these domains are of small volume fraction and are like present due to defects in the film. The in-plane PFM image is shown in Figure B.2(c). Here it is clearly seen that there are two contrasts that form long striped like ribbons. One contrast is white while the darker contrast is the grey scale of this image and thus indicates a no contrast region. The white domains have a in-plane polarization direction that points down in the image and is indicated by the white arrow in the image. The long axis of the tip is along the x-axis of the image (left-right), thus a polarization along this direction cannot be determined from this image alone and appears as a no contrast in this image. The direction of te polarization in this domain is easily determined by rotating the sample by 90^o and imaging the same region, to reveal that the polarization in the no contrast domain points to the left in Figure B.2(c) and is represented by the black arrow in the figure.

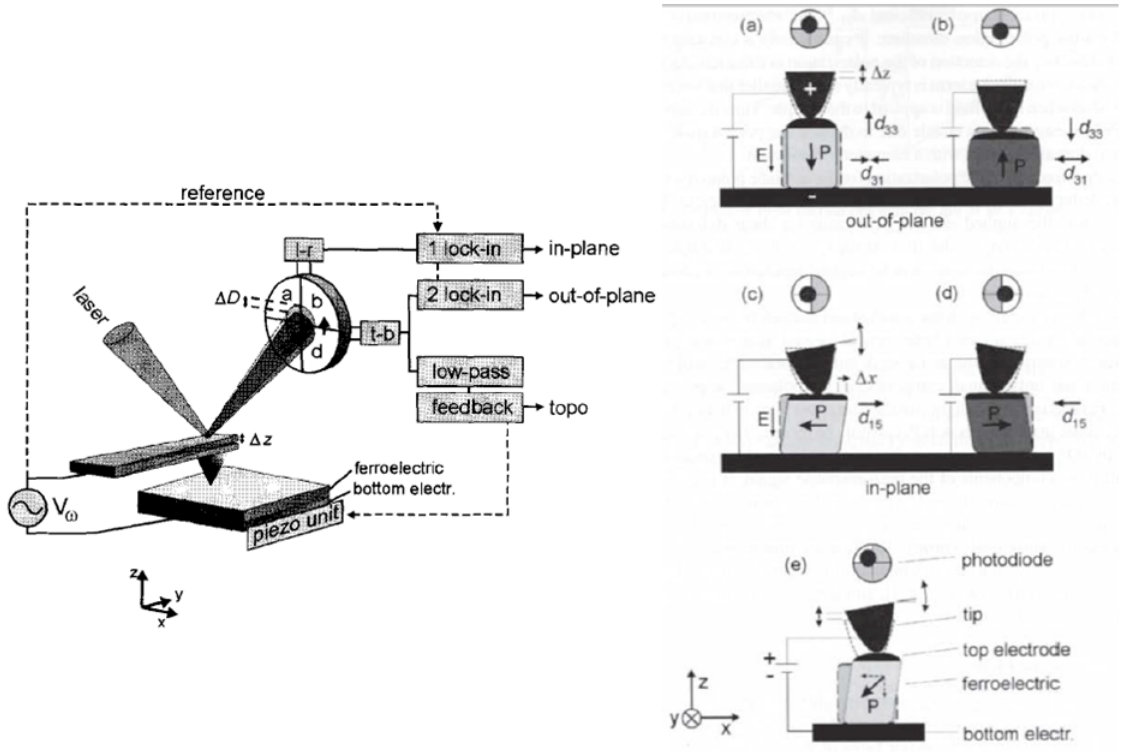

Figure B.1: (left) Schematic of the PFM measurement with tip, sample, 4-quadrant photodiode detector, laser, AC voltage and lock-in amplifiers. (Right) (a,b) Piezo-distortions from a ferroelectric sample with out-of-plane polarization variants due to a out-of-plane oriented electric field (d_{33}) with corresponding motion of the PFM tip. (c,d) Piezo-distortions from a ferroelectric sample with in-plane polarization variants due to a out-of-plane oriented electric field (d_{31}). (e) Tip motion and detection from a polarization with both in-plane and out-of-plane components. Image taken from [164].

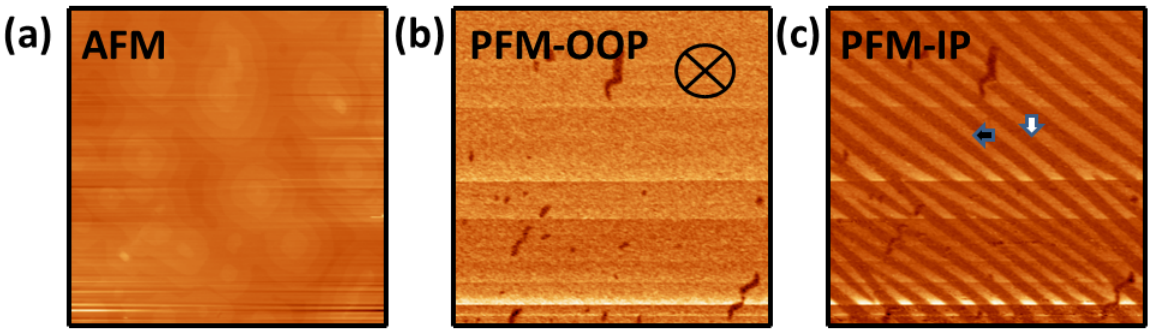

Figure B.2: (a) AFM image of the surface topology (b) out-of-plane (OOP) PFM image. White contrast corresponds to polarization directed into the page and black contrast out of the page, (c) in-plane (IP) PFM image. The white stripes indicate a in-plane polarization that points down and the no contrast (darker domains) have a in-plane polarization component that points to the left.

Appendix C

From 180^o to 360^o periodic AMR

In Figure 4.3 I showed the device characterization verifying the AMR response at high field (500 Oe, black open triangles) and low field (20 Oe, blue open squares). At 500 Oe the Zeeman energy dominates the energy landscape and thus $\theta \cong \theta_a$ (angle of the applied field w.r.t. the applied current direction). Thus if $\theta \cong \theta_a$ then the high field AMR curve should follow a $\cos^2\theta_a$ dependence, which is observed by the 180^o periodicity of the curve and the large amplitude of the resistance oscillations (see Figure 4.3(a)).

However, what is interesting is what happens at low magnetic field. At low field the Zeeman energy is significantly smaller than the anisotropy energy and the result is that the magnetization simply wiggles about its anisotropy axis without switching. At small applied magnetic field the approximation can be made that θ_u - θ is small and therefore the uniaxial anisotropy term can be rewritten as:

$$\frac{MH_u}{2}sin^2(\theta_u - \theta) \approx \frac{MH_u}{2}(\theta_u - \theta)^2 \tag{C.1}$$

$$= MH_u(-1 + 1 + \frac{(\theta_u - \theta)^2}{2}) \tag{C.2}$$

$$\approx MH_u(cos(\theta_u - \theta) - 1) \tag{C.3}$$

When the magnetization only wiggles slightly from the uniaxial anisotropy direction, the effective energy landscape has a $\cos(\theta_u$ - $\theta)$ dependence. A unidirectional anisotropy is modeled with a $\cos(\theta_{ex.bias}$ - $\theta)$ term. Hence, at applied magnetic fields that are significantly lower than the anisotropy field, the uniaxial anisotropy effectively acts like a unidirectional anisotropy in that the uniaxial energy barrier is to large for switching and the magnetization wiggles about its equillibrium direction. [79] This fact is what causes the change in the AMR phase at low field. [129, 123] The 360^o periodicity can be derived easily now that its understood that the anisotropy is effectively unidirectional at small field. With that, we can write the total magnetic field felt by the magnetization to be:

$$\vec{H_{total}} = \vec{H_{applied}} + \vec{H_{anisotropy}} \tag{C.4}$$

The magnetization will point along this effective field direction. Thus we can determine the angle of the magnetization with respect to the applied current, θ, with the following:

$$\vec{M} \bullet \vec{H_{total}} = M H_{total} cos(\theta) \tag{C.5}$$

$$cos^2(\theta) = \frac{(H_{applied} cos(\theta_a) + H_{anisotropy} cos(\theta_u))^2}{(H^2_{applied} + H^2_{anisotropy} + 2 H_{applied} H_{anisotropy} cos(\theta_a - \theta_u))} \tag{C.6}$$

$$= \frac{(h cos(\theta_a) + cos(\theta_u))^2}{(h^2 + 1 + 2h cos(\theta_a - \theta_u))} \tag{C.7}$$

Now since the applied field is much smaller than the anisotropy field, h is much smaller than one. Terms in h^2 are negligible and 1+2hcos(θ_a-θ_u) is approximately equal to 1 since h is small and cos $\leq$ 1. This leaves us with

$$cos^2(\theta) = 2h cos(\theta_a) cos(\theta_u) + cos^2(\theta_u) \tag{C.8}$$

which has a 360^o periodicity in θ_a and θ_u is fixed by the $BiFeO_3$.